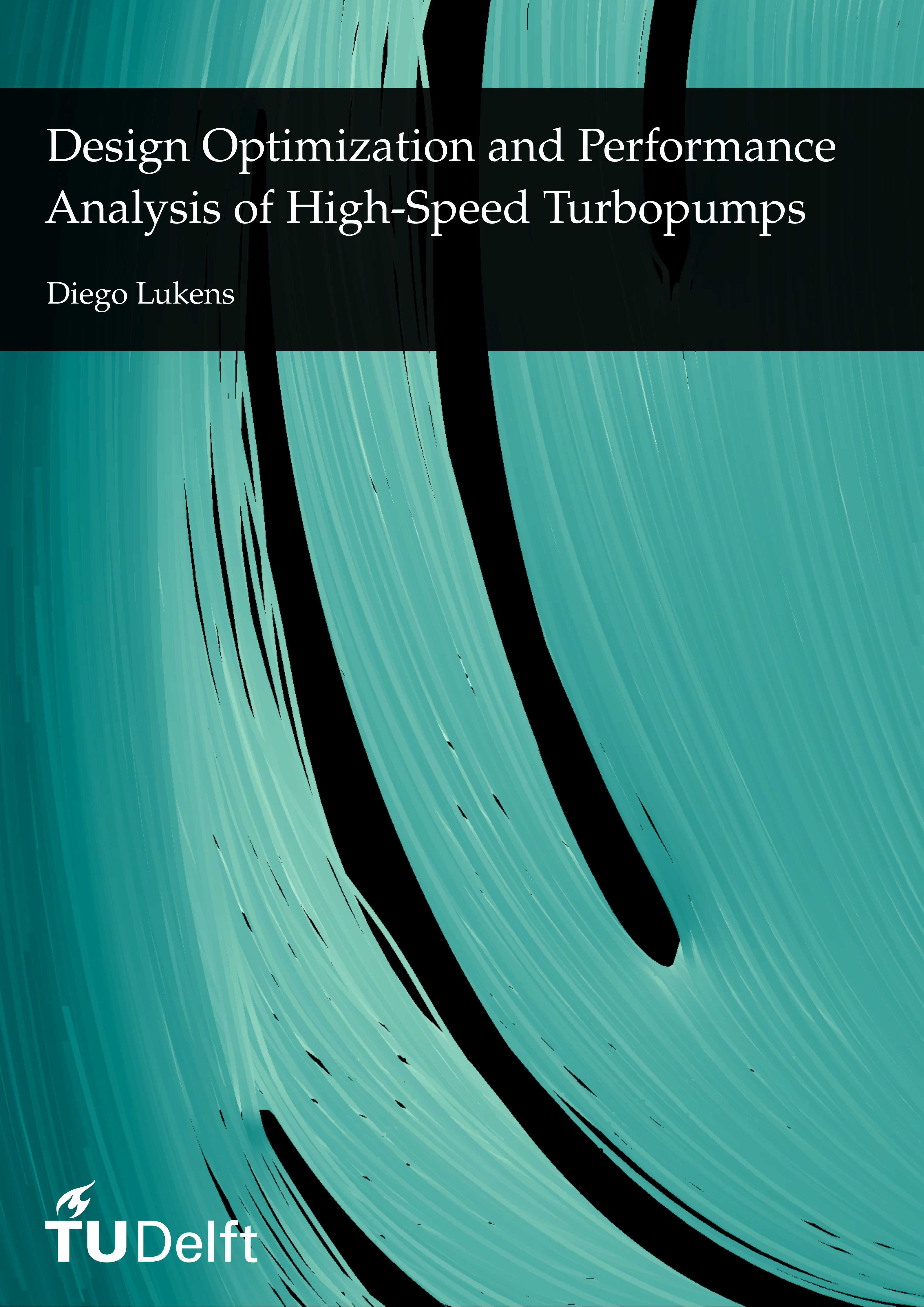

Design Optimization and Performance Analysis of High-Speed Turbopumps

Diego Lukens

Design Optimization and Performance Analysis of High-Speed Turbopumps

MSc Thesis

by

Diego Lukens

To obtain the degree of Master of Science
at the Delft University of Technology.
Defended publicly on Thursday August 29, 2024 at 4:00 PM.

Student number:	4648196	
Project duration:	September 8, 2023 – July 27, 2024	
Thesis committee:	Dr. M. Pini	(Supervisor)
	Dr. I. Langella	(Chair)
	Dr. N.A.K. Doan	(External Examiner)
Location:	Faculty of Aerospace Engineering, Delft University of Technology	

TU Delft

Acknowledgments

I want to thank everyone who has been a part of my journey through Delft. It has been a time of enormous personal growth filled with learning, hard work, and memorable moments. I feel extremely lucky and privileged to have had this unforgettable experience.

I thank my parents and family for their unconditional love and support, which have encouraged my education and made it possible. I thank my amazing friends and housemates for getting me out of my comfort zone, supporting me, and bringing optimism and joy to my life. Last but not least I thank Dr. Matteo Pini for trusting and allowing me to work on this exciting project under his supervision and guidance.

I wouldn't have made it this far without all the wonderful people around me.

Thank you!

Diego Lukens
Delft, August 2024

Abstract

The focus of this thesis is the preliminary design optimization and performance analysis of non-cavitating centrifugal turbopumps using a 1D lumped-parameter method. Centrifugal pumps are critical components in many engineering applications due to their high efficiency in converting mechanical energy into fluid pressure. This study presents the development and validation of a computationally efficient model to design and predict the flow properties along different stations of a centrifugal pump. The methodology minimizes the reliance on expensive CFD simulations, making use of multiple design parameters to control the impeller, diffuser, volute, and exit cone configurations to ensure a robust and efficient performance.

A common challenge in turbopump design is the prediction and mitigation of cavitation, which occurs when the fluid static pressure falls below its vapor pressure. This leads to the formation and subsequent collapse of vapor bubbles, which can cause severe damage to pump components. Given the complex physics involved, this work makes use of reduced-order models to predict, and avoid cavitating regimes through design adjustments.

This thesis provides a comprehensive framework for optimizing the design of centrifugal turbopumps by integrating validated loss models and a reduced-order modeling approach. The proposed design methodology is applied to develop a centrifugal pump for the TU Delft ORCHID facility, demonstrating its feasibility and effectiveness. This research contributes a practical modeling tool for centrifugal turbopump optimization and performance analysis.

Contents

List of Figures

List of Tables

Nomenclature

Acronyms

AR	Aspect Ratio
BEP	Best Efficiency Point
CAD	Computer-Aided Design
CFD	Computational Fluid Dynamics
DF	Diffusion Factor
EoS	Equation of State
LE	Leading Edge
NICFD	Non-Ideal Compressible Fluid Dynamics
NPSH_A	Net Positive Suction Head Available
NPSH_R	Net Positive Suction Head Required
ORC	Organic Rankine Cycle
ORCHID	Organic Rankine Cycle Hybrid Integrated Device
RANS	Reynolds-Averaged Navier Stokes
ROM	Reduced-Order Model
RPM	Revolutions per Minute
TE	Trailing Edge

Greek Letters

α	Absolute Flow Angle
β	Relative Flow Angle
δ_r	Swirl Number
ϵ_t	Tip Clearance
η	Efficiency
$\lambda_{w,c}$	Blade Cavitation Coefficient
ν	Kinematic Viscosity
ω	Rotational Speed
ϕ	Flow Coefficient
ψ	Work Coefficient
ρ	Density
σ	Slip Factor
σ_b	Cavitation Number
τ	Blade Blockage Factor
τ_{al}	Allowable Shear Stress

Roman Letters

$\dot{m}$	Mass Flow Rate
$\dot{Q}$	Heat Flow Rate
$\dot{W}$	Work Rate
A	Area
b	Width
C_f	Friction Coefficient
C_p	Pressure Recovery Coefficient
C_v	Specific Heat Capacity at Constant Volume
d	Diameter
e	Surface Roughness
F_{ax}	Axial Force
g	Acceleration of gravity 9.81

H	Head
h	Specific Enthalpy
I	Rothalpy
i	Blade incidence
k_n	Impeller Shape Factor
n	Revolutions per Minute
N_{bl}	Number of Main Blades
N_{split}	Number of Splitter Blades
n_q	Specific Speed
n_{ss}	Specific Suction Speed
P	Pressure
P_{el}	Electric Power
P_v	Vapor Pressure
Q	Volumetric Flow Rate
r	Radius
Re	Reynolds Number
T	Temperature, Torque
U	Circumferential Velocity
u	Internal Energy
V	Absolute Velocity
W	Relative Velocity
w	Specific Work
Z	Height
L	Length
P	Power
t	Blade Thickness

Subscripts

B	Blade
h	Hub
i	Inception
m	Meridional
s	Shroud
t	Total quantity, tangential
0	Impeller Inlet
1	Impeller Outlet / Diffuser Inlet
2	Diffuser Outlet / Volute Inlet
3	Volute Outlet / Exit Cone Inlet
4	Exit Cone Outlet
des	Design
diff	Diffuser
eul	Euler
ext	External
hyd	Hydraulic
int	Internal
is	Isentropic
max	Maximum
min	Minimum
ref	Reference
tt	Total-to-Total

Superscripts

$\overline{\alpha}$	Mean Value
$'$	Station *Inside* the Impeller Passage

1

Introduction

This thesis explores the preliminary design and optimization of centrifugal pumps, which are highly valued in many engineering fields. The goal is to develop and validate a program capable of quickly designing and predicting flow properties along various stations in a pump. Based on the latest available literature, this can be achieved in a computationally efficient manner with a 1D lumped-parameter model. The idea is to minimize the CFD simulations required to design an efficient and robust machine. The presented model can analyze and optimize the performance of a pump with an impeller, diffuser, volute, and exit cone.

To do this, cavitation must be considered, as it is a major limiting factor in the design and operation of high-speed pumps. This phenomenon often occurs around the pump inlet, when the working fluid static pressure falls below its vapor pressure $P < P_v$. This causes the liquid to change phase into a gas. Then, as the pressure within the pump rises, the fluid pressure increases past the vapor pressure P_v again, causing the gas bubbles to collapse rapidly. This collapse is an extremely high-energy event that causes damage to any surface in its vicinity. Thus, predicting and mitigating cavitation is often a major effort in pump design.

The challenge is that cavitation is an extremely localized and three-dimensional effect that cannot be accurately captured without expensive multi-phase CFD simulations or experimental campaigns. The approach here is to conservatively predict the inception of cavitation and avoid it through design choices.

1.1 Turbomachinery

Turbomachines are energy conversion devices that continuously convert mechanical energy into thermal or pressure energy between a fluid and a rotating machinery component or 'rotor'. The thermal or pressure energy in the fluid can be in kinetic or static enthalpy form and can be converted in either direction through a diffuser or nozzle, called 'stator' [59].

The term "turbo" originates from Latin, referring to something that spins or whirls. A rotor or impeller alters the stagnation enthalpy of the fluid passing through it by performing either positive or negative mechanical work. These enthalpy changes are closely related to the net pressure changes within the fluid [25].

As shown in Figure 1.1, the various types of turbomachines can be categorized into several groups based on different criteria. First, based on the direction of energy transfer, turbomachines can either be work-absorbing, such as fans, compressors, and pumps, which elevate fluid pressure or head, or work-producing, such as wind, hydraulic, steam, and gas turbines, which expand a fluid to a lower pressure or head. Second, turbomachines can handle compressible fluids (gases) or incompressible fluids (liquids) based on the fluid type. Lastly, based on the direction of flow through the rotor, turbomachines can be classified as axial, where the flow path is mainly parallel to the axis of rotation; radial, where the flow path is mainly in a plane perpendicular to the axis of rotation; or mixed, where the flow at the rotor outlet has significant radial and axial velocity components.

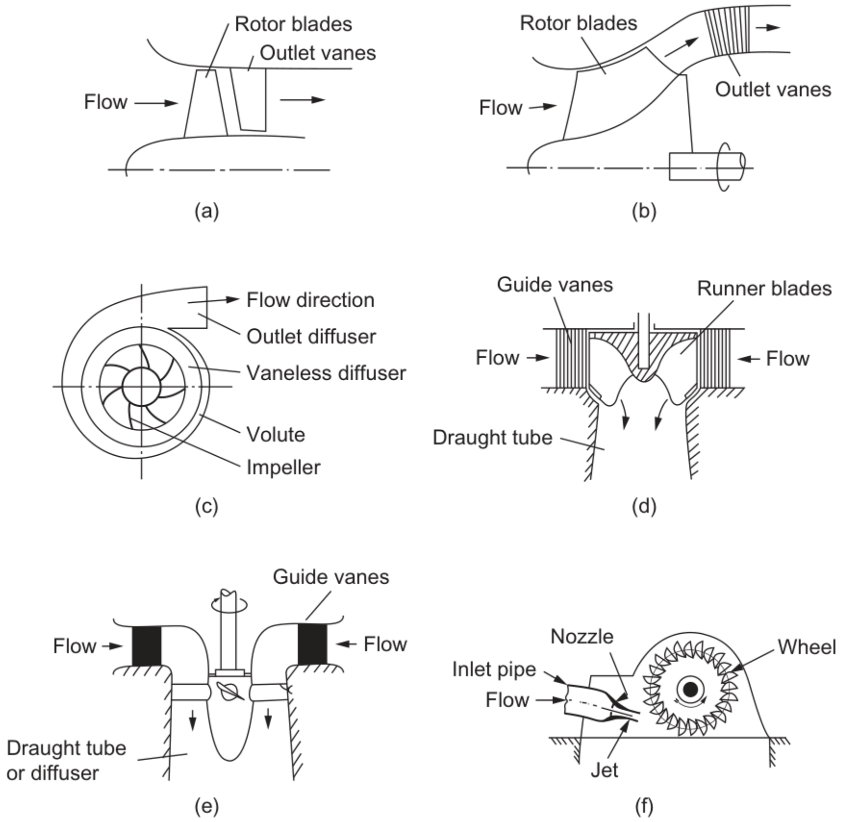

Figure 1.1: Examples of turbomachines: (a) Single stage axial flow compressor or pump, (b) mixed flow pump, (c) centrifugal compressor or pump, (d) Francis turbine (mixed flow), (e) Kaplan turbine, and (f) Pelton wheel. [25]

1.2 Literature Study

This section reviews the history, current turbomachinery landscape, and recent developments. While a general overview of turbomachines is given, the review of design and analysis methods is limited to the scope of this work: centrifugal turbopumps.

1.2.1 Applications

Turbomachines are everywhere. They are essential components in power generation, transportation, refrigeration, construction, chemical processing, computer cooling, hydraulics, and medical devices, among many other applications.

In central power plants, steam turbines convert thermal energy into mechanical energy to power electric generators. Pumps handle liquid water, such as boiler-feed pumps and condensate pumps. Turbomachines are also key in energy-producing systems like hydropower, wind power, and geothermal installations.

Gas turbine engines, including multistage axial-flow turbines and compressors, are essential in aircraft and industrial power plants. Centrifugal types are used in smaller engines for ground operations, marine vessels, aircraft, and automotive turbochargers. Pumps, fans, blowers, and compressors pressurize and transport liquids or gases in fluid-handling systems across industries. These systems are crucial in HVAC systems, water supply, treatment, irrigation, oil production, refining, gas transport, chemical processes, and other industries.

Modern turbofan and turbojet engines are great examples of turbomachinery innovations in the aerospace industry. They use (mostly) axial compressors and turbines to power themselves and propel the aircraft forward. Open propellers are also a form of turbomachine, as they increase the momentum of the air passing through them. Spacecraft use some of the most advanced turbomachinery designs to feed propellant and oxidizer into their engines, given their need for high power density.

Finally, organic Rankine cycle (ORC) power systems are a rising application for low specific-speed turbomachines for converting renewable and waste thermal energy. ORC technology is very flexible and is often the only applicable technology for converting external thermal energy sources. As the name suggests, ORC power systems use complex organic compound fluids in a Rankine thermodynamic cycle to recover waste heat from low-temperature sources. The role of turbomachinery in ORC systems is growing, and advancements in the integrated cycle's efficiency recovering waste heat can enable new energy management technologies [28], [45], [5] and have a huge effect in the fight against climate change [16].

1.2.2 Historical Developments

Turbomachinery has a rich history dating back to ancient Greece. Over time, water wheels and early turbines like *Leonardo da Vinci's smoke jack* began harnessing air and water flow for mechanical work. The Industrial Revolution saw the rise of steam turbines, with *Carl Gustaf de Laval* and *Charles Parsons* pioneering impulse and reaction turbines, respectively. Gas turbines, introduced by *John Barber* in 1791, evolved significantly by 1903 when *Ægidius Elling* built the first gas turbine producing positive net power.

The development of modern turbomachines began in the 18th century, with major pump development initiated in 1705 by *Denis Papin*, who detailed centrifugal blowers and pumps. Crude versions remained prevalent in the US until the early 19th century. In 1839, *W. D. Andrews* introduced a volute, and in 1875 *Osborne Reynolds* patented a vaned diffuser in England. By 1884, *Charles Parsons* patented an axial-flow compressor, followed by a three-stage centrifugal compressor for ship ventilation in 1887. By 1899, he achieved an 81-stage axial-flow compressor with 70% efficiency but encountered issues, reverting to centrifugal machines in 1908. Concurrently, *August Rateau* in France contributed to compressor development, focusing on gas turbine engines.

The modern-day development of turbomachinery has skyrocketed from Parsons' early design, from producing 0.746 kW, to modern nuclear steam turbines producing upwards of 1500 MW. In 2021, steam turbines in various types of power plants accounted for roughly 45% of the electrical power generated in the United States. With engineers constantly striving for increased efficiency, current industrial steam turbines operate with over 60% efficiency and an inlet temperature of 1600° C [59].

1.2.3 Recent Developments

Advancements in the miniaturization and efficiency of high-speed electric motors (up to 1 million rpm) [81] are allowing for new technological innovations making use of small-scale, high-speed turbomachinery (analogous to low specific-speed n_q). For example, [64] investigates the design and optimization of small-scale radial compressors for domestic heat pump applications, which could reach up to 250 krpm, showing that the residential sector accounts for around a third of global energy consumption. The miniaturization of efficient turbomachines combined with the development of ORC systems unlocks waste heat recovery for the transportation sector, as shown by [9] applied to heavy long-haul diesel truck engines, given that 40-50% of energy in fuel-driven power generation is usually dissipated as heat [66]. Following this trend, a study on the combined-cycle turboshaft engine with an ORC bottoming unit on an aircraft with a turbo-electric propulsion system shows the potential for around 4% fuel savings [45].

In addition, oil-free bearings are a key enabling technology of efficient high-speed turbomachinery, as they eliminate the need for lubricants, reduce maintenance, and increase mechanical efficiency [32]. However, they exhibit a highly non-linear behavior and often require digital twins to monitor performance and provide sufficient operational reliability [57].

The implementation of electrically-driven heat pumps with high-speed centrifugal pumps are preferred over standard volumetric machines due to the potential for higher efficiencies, reduced volume and weight, absence of lubricant oil, thanks to foil bearings [36]. The optimal design of mini centrifugal pumps requires high efficiency, a wide operating range, and high power density. Additionally, the design must adhere to strict constraints concerning minimum impeller dimensions for manufacturability, maximum allowable rotational speed, and maximum tolerable axial thrust to accommodate gas bearings. More compact stages reduce material and machining costs, lower weight and inertia, and a smaller frontal area, resulting in lower axial thrust. Selecting optimal pump design parameters is further complicated by the choice of the working fluid, which depends on the heat pump's design requirements [28].

As low specific-speed turbomachines are becoming more attractive due to their compactness, studies are being carried out to predict and characterize their relatively unexplored performance, given that they are more prone to unstable head capacity characteristics [33]. While reduced-order models can predict the performance of geometrically similar pumps as a function of specific speed n_q, the performance is affected by additional effects such as higher relative roughness and tip clearance. To this extent, [77] investigates the adverse influence of tip clearance in the preliminary design of small-scale ORC turbopumps and presents novel neural network slip and head loss coefficient models. The same authors have also explored the influence of splitter blades and meridional profiles on the performance of small-scale turbopumps for ORC applications, showing that splitter blades can increase the head and slip factors by 10-24% depending on the blade outlet angle [76]. Furthermore, the effect of size and working fluid on the efficiency, operating range, and axial thrust is examined for high-speed, oil-free centrifugal compressors with validated reduced-order models, showing that complex molecule working fluids provide lower efficiencies and that the clearance gap ratio is more influential than surface finish [28].

Many studies have compiled recommendations of validated loss model sets for centrifugal compressors published in open literature [56] [44]. While centrifugal pump loss models have not received the same scientific attention (in part due to compressor loss mechanism similarity), several studies have investigated the efficiency and loss mechanisms of pumps with varying specific speeds. In [50], the authors propose theoretical models for the detailed modeling of losses inside a hydraulic pump that can operate as a turbine and validate their accuracy with CFD simulations. In another study [11], the authors systematically summarized loss calculation formulas for the internal flow field of a mixed flow impeller to predict its performance curve.

Multiple 1D design methodologies have been published, including the design procedure for inducers with arbitrary shapes, usually mounted upstream of a pump impeller with low NPSH [53]. Methodologies for the analytical design of pump impellers have been developed from turbomachinery first principles [55], and methodologies to optimize compressor and vaned diffuser geometries (applicable to pumps) have also emerged in recent years [49]. New optimization models include the influence of design robustness due to manufacturing uncertainties [51] [42], since small impellers are more sensitive to geometrical imperfections. Furthermore, data-driven approaches are emerging to generate entire families of turbomachinery designs [54] [30] as a new way of exploring optimum designs.

Lastly, it is well known that cavitation is a challenge in the design of high-performance turbopumps [33]. The fundamental physics of cavitation is mature and well-understood, with several decades of research in the field and various test-validated models in the open literature. The *Rayleigh-Plesset* equation, hydrodynamics of pump cavitation, numerical cavitation simulation, performance analyses, bubble dynamics, and other topics are well documented in the literature [13] [20]. Many characterization and validation campaigns have been conducted against CFD [14] [73]. New methods to reduce the high computational expense of multiphase simulations [72], and experimental cavitation diagnostics, such as rotating cavitation [48], have been introduced in recent years.

1.3 Research Objectives

The turbomachinery research field has been active and vibrant in the past few decades and only shows signs of growth. It is a broad field that brings together the best of every engineering discipline. High-performance centrifugal turbopumps have been gaining attention due to new applications in the aerospace and transportation sectors, with rocket engines and ORC heat recovery systems being prime examples. Therefore, it is of interest to aid in the design and analysis of such machines.

Research objectives

- To develop a preliminary design and optimization framework for non-cavitating turbopumps.
- To develop a centrifugal pump design to replace the TU Delft ORCHID main pump.

Research questions

- To what degree can a reduced-order turbopump design model assess performance compared to CFD?
- What is the size and the efficiency of the ORCHID centrifugal pump?

2

Theoretical Background

This chapter outlines several component definitions and design procedures. It also reviews the relevant thermodynamics and provides the working principles of each component in a centrifugal pump.

2.1 Fundamental Equations

We begin by asserting that centrifugal pumps are machines that add **mechanical energy** to a working fluid. Furthermore, the full thermodynamic state of a fluid is defined for a given state variable input pair such as (P, T), (P, h), and (T, s). By knowing how these state variables evolve through each component, the thermodynamic state can be resolved (with the necessary assumptions). Let's begin by recalling the definition of total enthalpy:

$$h_t = h + \frac{V^2}{2} = u + \frac{P}{\rho} + \frac{V^2}{2} = C_v \cdot T + \frac{P}{\rho} + \frac{V^2}{2} \tag{2.1}$$

We can now introduce the definition of the total power dE/dt through a control volume:

$$\frac{dE}{dt} = \dot{m}_{\text{in}} \cdot \left(h_{\text{in}} + \frac{1}{2}V_{\text{in}}^2\right) - \dot{m}_{\text{out}} \cdot \left(h_{\text{out}} + \frac{1}{2}V_{\text{out}}^2\right) + \dot{Q}_{\text{in}} + \dot{W}_{\text{in}} \tag{2.2}$$

In this work, the flow is considered adiabatic ($\dot{Q}_{\text{in}} = 0$), steady-state ($dE/dt = 0$), and incompressible ($\dot{m}_{\text{out}} = \dot{m}_{\text{in}} = \dot{m}$). By making use of the specific work $w_{\text{in}} = \dot{W}_{\text{in}}/\dot{m}$, we obtain the specific work input:

$$w_{\text{in}} = \Delta h_t = \left(h_{\text{out}} + \frac{1}{2}V_{\text{out}}^2\right) - \left(h_{\text{in}} + \frac{1}{2}V_{\text{in}}^2\right) \tag{2.3}$$

With the total enthalpy $h_t = h + 1/2 \cdot \rho \cdot V^2$. This expression relates the thermodynamic state of the flow *before* and *after* the component to the work provided to the flow. This is a useful expression to assess the performance of a machine, as seen with the *Euler* equation:

$$\Delta h = h_2 - h_1 = \omega \cdot (r_2 \cdot V_{2t} - r_1 \cdot V_{1t}) = \frac{1}{2}\left(U_2^2 - U_1^2\right) + \frac{1}{2}\left(W_1^2 - W_2^2\right) \tag{2.4}$$

We also introduce the conservation of energy relating the velocity (kinetic energy), pressure, and height (potential energy) of a subsonic incompressible fluid:

$$P_t = P + \frac{1}{2}\rho V^2 + \rho g z \tag{2.5}$$

The assumption of incompressibility is granted when designing for pump applications. Most fluids in a liquid state do not exhibit an appreciable change of density of practical effect, even under extremely high pressures. **Note** that in this work, the gravitational potential $\rho g z$ is ignored due to its negligible contribution.

Lastly, a common convention used for pump selection and design is to express the produced pressure rise in the form of *Head*.

$$H = \frac{\Delta P_t}{\rho \cdot g} = \frac{\Delta P}{\rho \cdot g} + \frac{V^2}{2 \cdot g} \tag{2.6}$$

This is measured in meters and normalizes the pressure rise with density so that pump performance can be communicated independently of the working fluid. Practically, it is useful as it allows for a intuitive understanding through the height of a column of liquid.

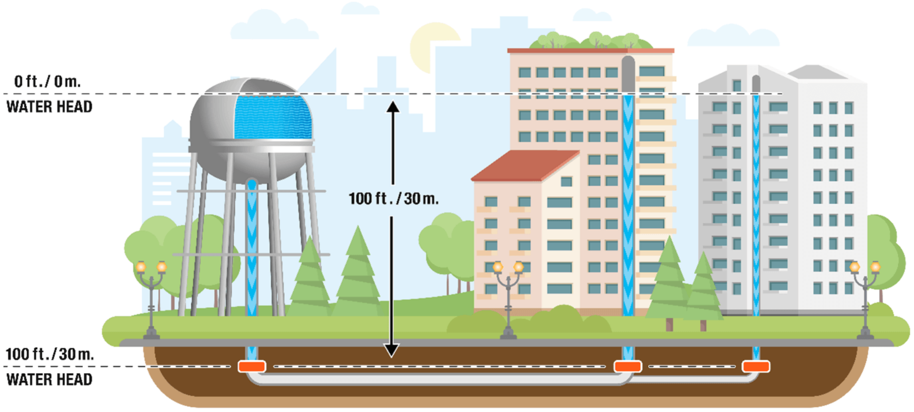

Figure 2.1: Pressure head representation

2.2 Velocity Triangles

A fundamental concept in turbomachinery analysis is the velocity triangle. In essence, it is a vectorial decomposition of the bulk flow of a fluid in both the stationary and rotating frames of motion. It allows for simplified analysis and description of the flow properties and further derivation of helpful non-dimensional parameters that characterize the performance of machines with varying characteristics. Assuming a circumferentially uniform flow, there are two velocity triangles for a radial impeller: One at the inlet and one at the outlet.

- **V**: Bulk flow velocity in the *absolute* (stationary) reference frame.
- **W**: Bulk flow velocity in the *relative* (rotating) reference frame.
- **U**: Blade circumferential velocity.
- α: Flow angle with respect to the blade in the *absolute* frame of reference.

- $\boldsymbol{\beta}$: Flow angle with respect to the blade in the *relative* frame of reference.

These quantities can be further decomposed into tangential and meridional components e.g: V_t, and V_m. In addition, subscripts are added to identify each station: ′0′ for the impeller inlet W_{0m}, and ′1′ for the outlet W_{1t}. Note that there are several numbering conventions for stations in the literature. Note that the location of these stations is not defined by convention so it is up to the reader to understand the numbering system used throughout literature. In the present work, the inlet of the impeller is defined as the ′0′ station. See Figure 2.2 (differing numbering convention).

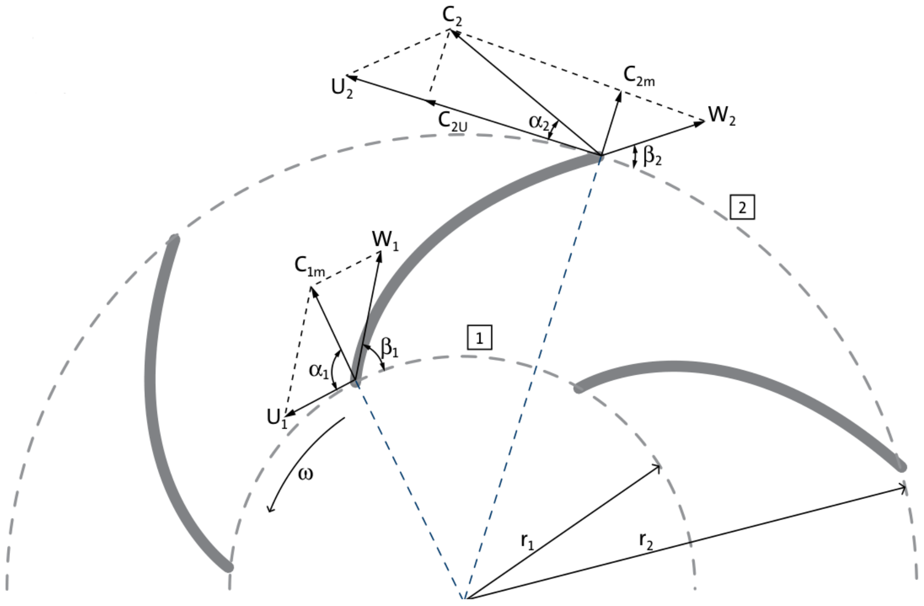

Figure 2.2: Impeller velocity triangles

For many applications, the inlet flow is assumed to have no pre-rotation i.e: pure axial flow into the impeller eye ($V_{t0} = 0$, $\alpha = 0$). The inlet and outlet velocity triangles look as follows:

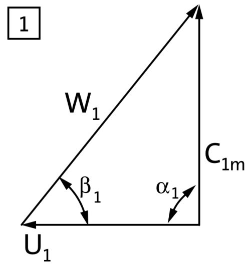

Figure 2.3: Inlet velocity triangle with no pre-rotation

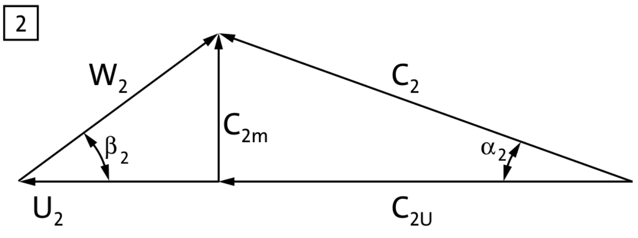

Figure 2.4: Outlet velocity triangle

Note: α and β can be defined with respect to the circumferential direction (as shown above), or alternatively with the meridional (radial) velocity component. This work uses the ′alternative′ definition, with α and β measured with respect to the meridional velocity component V_m. To convert from one convention to the other: $\alpha_{V_t} = 90° - \alpha_{V_m}$.

2.3 Flow Analysis

The three-dimensional flow inside a centrifugal pump can only be accurately assessed through experimental test campaigns or transient (often multi-phase) CFD simulations. However, the flow modeling can be simplified by considering uniform thermodynamic properties of the flow at the various stations through the machine. This kind of analysis is called a 1D lumped-parameter system model and can yield relatively accurate results compared to CFD simulations. These stations are located at each component's immediate inlets and outlets along the main flow path. We now describe each component in a turbopump and their fundamental working principles.

2.3.1 Impeller

The impeller is a rotating component that adds energy to the flow. Looking at Figure 2.5, the flow enters the impeller *axially* and leaves the impeller *radially*.

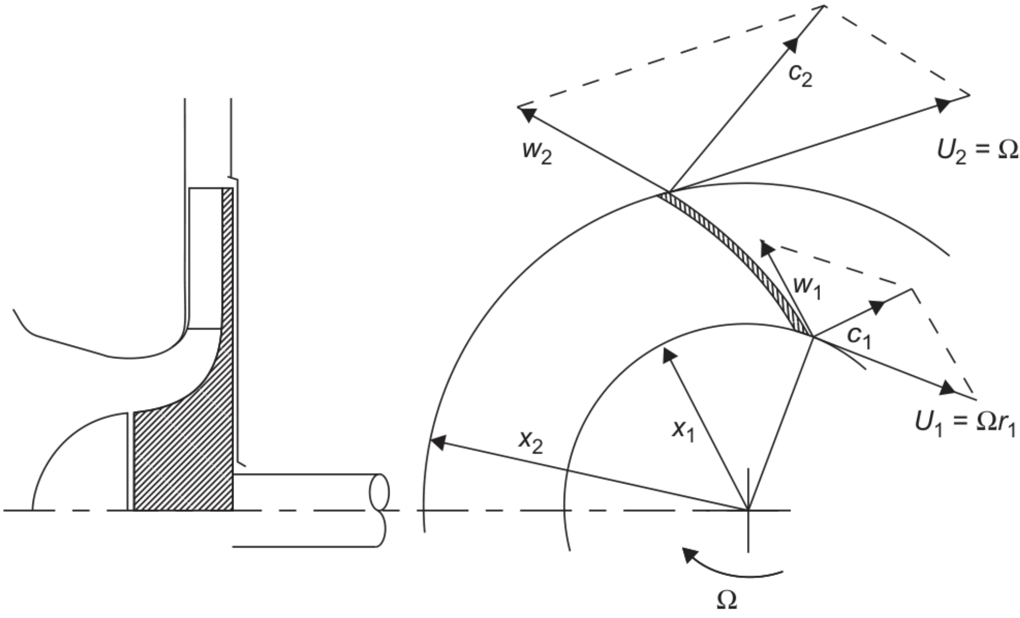

Figure 2.5: Impeller velocity triangles [25]

If we consider that we have both inertial (stationary) and rotating frames of reference with a fixed angular velocity ω, we can define the *rothalpy* I of the fluid. Rothalpy is known as the relative stagnation enthalpy of a flow in a rotating system, and it is commonly used to analyze turbomachines. Assuming a steady, adiabatic, and irreversible flow, the value of rothalpy across a blade remains constant along a streamline:

$$I = h_{0,rel} - \frac{1}{2}\left(V_t^2 + V_m^2 - 2 \cdot U \cdot V_t\right) \tag{2.7}$$

By adding and subtracting $u^2/2$ and considering that $W = V - U$, we can obtain a simplified form, as Equation 2.8.

$$I = h - \frac{1}{2}\left(W^2 - U^2\right) = h_{0,rel} - \frac{U^2}{2} \tag{2.8}$$

With the relative stagnation enthalpy $h_{0,rel} = h + \frac{1}{2}W^2$. Given that the rothalpy I of a turbomachine is constant, i.e., $I_1 = I_2$, the following expression can be defined:

$$h_2 - h_1 = \frac{1}{2}\left(U_2^2 - U_1^2\right) + \frac{1}{2}\left(W_1^2 - W_2^2\right) \tag{2.9}$$

With Equation 2.9, we can appreciate how the enthalpy rise is decomposed. The term on the right $\left(W_1^2 - W_2^2\right)$ is the contribution from the diffusion of the relative velocity. The first term $\left(U_2^2 - U_1^2\right)$ is the contribution from the centrifugal force. This term is unique to centrifugal machines due to the change in radius along a meridional streamline. It explains why they can achieve much higher pressure ratios than their axial counterparts. In Figure 2.6 below, the relationship between the enthalpies across an impeller and a diffuser is shown.

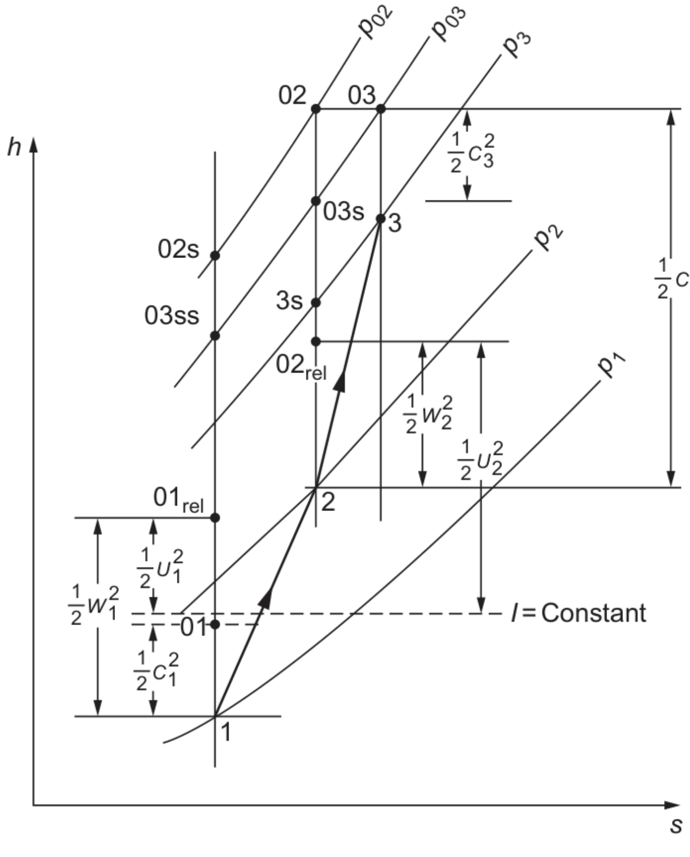

Figure 2.6: Enthalpy-Entropy (h-s) diagram for a pump impeller and diffuser.

Finally, the specific work of the pump can be found using Equation 2.9. Again, assuming no inlet pre-rotation ($V_{t1} = 0$), the specific work change done on the fluid is:

$$\boxed{\Delta w = U_1 \cdot V_{t1} = h_{t1} - h_{t0} = g \cdot H_i \tag{2.10}}$$

With H_i being the *ideal* pump head rise across the impeller. This excludes all internal losses—an isentropic process. In other words, it is the theoretical shaft work w needed to achieve a desired pressure rise without any losses considered. Last but not least, Equation 2.10 shows us that the final head H of a pump is a function of the outlet rotational speed U_1, and the outlet circumferential (tangential) flow velocity component V_{t1}. In later sections, we will delve into the design parameters that control these variables to obtain a prescribed head H.

2.3.2 Radial Diffuser

Centrifugal compressors and pumps are generally fitted with a vaned or vaneless diffuser. Diffusers exchange kinetic energy, leaving the impeller with pressure energy. Their operating principle is simple: the swirl velocity is reduced by an increase in radius (conservation of angular momentum), and the radial flow area controls the radial velocity component. We can find the radial velocity at the diffuser outlet V_{2t} from continuity:

$$V_{2t} = \frac{r_1 \cdot b_1 \cdot \rho_1 \cdot V_{1t}}{r_2 \cdot b_2 \cdot \rho_2} \tag{2.11}$$

The continuity equation requires that $r \cdot V_m$ is constant for a parallel-walled radial diffuser with incompressible flow. Assuming that $r \cdot V_t$ remains constant, the absolute flow angle $\alpha_2 = \tan(V_t/V_r)^{-1}$ is also constant as the fluid diffuses outward. Under these conditions, the flow follows a logarithmic spiral path.

The performance of a diffuser is typically measured with the non-dimensional pressure recovery coefficient C_p. This coefficient measures how much of the total pressure at the inlet is converted into static pressure. Note that the right side of Equation 2.12 is an idealization considering incompressible and isentropic flow, by using mass continuity $V_1 \cdot A_1 = V_2 \cdot A_2$ and the area ratio definition $AR = A_2/A_1$:

$$C_p = \frac{P_2 - P_1}{P_{1t} - P_1} = 1 - \frac{1}{AR^2} \tag{2.12}$$

Lastly, it is noted that some stability criteria to establish a critical flow angle α_{1c} in vaneless diffusers have been developed and implemented for centrifugal compressors [28], [25]. However, some studies have shown that rotating stall in vaneless pumps is, first, not as common as in centrifugal compressors [70], and secondly, while it does incur losses, it does not have a large detrimental effect [35].

2.3.3 Volute

The volute or scroll is a spiral-shaped channel with an increasing cross-sectional area that collects the flow from the diffuser (or directly from the impeller) and delivers it to the exit pipe.

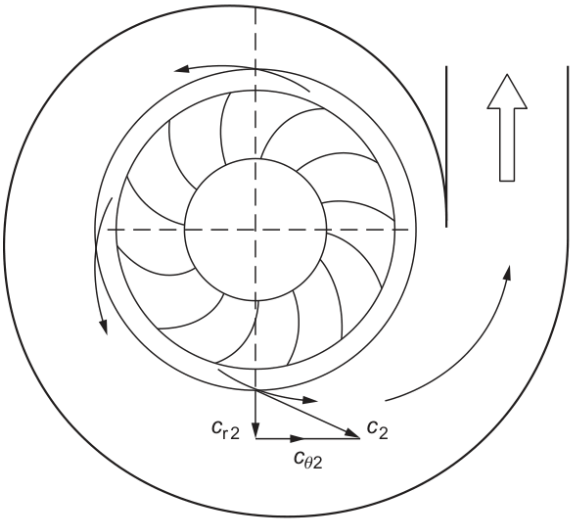

Figure 2.7: Top view of pump volute [25]

As the area from the inlet A_2 to the outlet A_3 of the volute increases, we again see an exchange of kinetic energy into static pressure governed by the conservation of mass. Lastly, it is noted that the volute of a centrifugal compressor can cause circumferential pressure distortion around the impeller at off-design flow rates. This is out of the scope of this project.

2.3.4 Conical Diffuser

Conical diffusers are commonly employed at the outlet of volutes to recover pressure energy further and provide a convenient port for the outlet piping. This is commonly expressed with the area ratio $AR = A_2/A_1$ of the inlet and outlet.

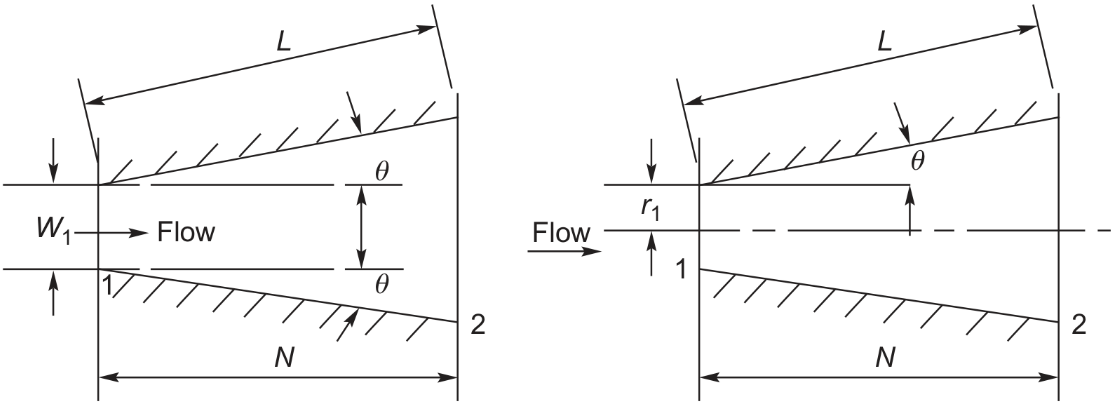

$$A_R = \frac{A_2}{A_1} = 1 + \frac{2N}{W_1} \tan\theta$$

$$A_R = \frac{A_2}{A_1} = \left(1 + \frac{N}{r_1} \tan\theta\right)^2$$

Figure 2.8: Diffuser geometries and their area ratios. Left: 2D, Right: Conical [25]

As no mechanical work is done on the fluid through a diffuser, the total pressure P_t is constant when assuming no losses. Recalling Equation 2.5, the kinetic energy term is exchanged with the pressure term. However, in practice, there is a reduction in total pressure due to viscous losses. A designer must consider two main flow phenomena when designing these types of diffusers. On the one hand, If the change in area is too large, flow separation can occur and lead to large mixing losses. On the other hand, if the rate of area change is very low, the boundary layer will grow excessively, leading to friction losses. The optimum diffusion rate, which is a combination of length and area ratio, is a function of the flow properties and surface roughness. However, several experimental campaigns have found that, as a rule of thumb, angles around 7-8° are optimal.

2.4 Performance Maps

Pump performance is usually described with a Head-Capacity or H-Q curve. It shows the relationship between the outlet head H and the volumetric flow rate Q (or alternatively mass flow rate $\dot{m}$) for each speed line n.

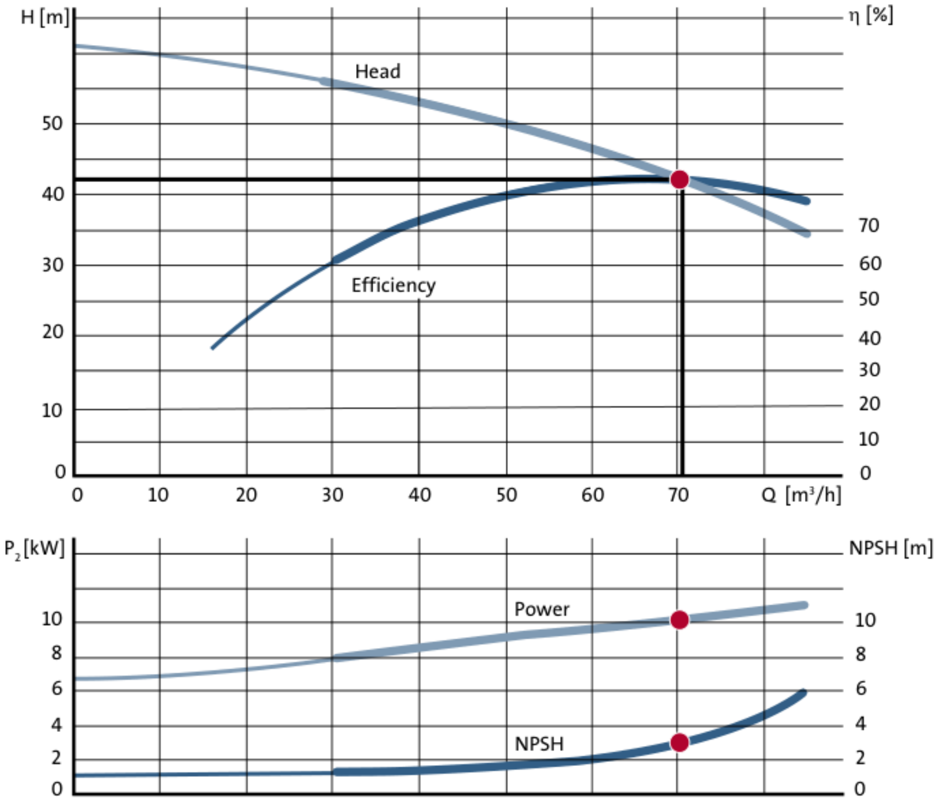

Figure 2.9: Typical performance curve for a centrifugal pump [38].

Usually, the efficiency across the operating range (OR) is shown, with the maximum corresponding to the best efficiency point (BEP), for which the pump is designed. When choosing or designing a pump, other parameters of interest are the required electrical power P_{el}, the required net positive suction head NPSH_R, and the axial thrust F_{ax}.

Lastly, the derivative of the H-Q curve is negative $dH/dQ < 0$, which indicates stable operation. A positive $dH/dQ > 0$ slope on a pump H-Q line leads to instability because small disturbances in flow rate create a positive feedback loop causing oscillations, increasing the risk of unstable behavior and cavitation. To ensure stable and efficient operation, pumps are designed to operate in regions with a negative H-Q slope.

2.5 Cavitation

Cavitation is a local phenomenon where the working fluid drops in pressure and changes into the gas phase. This is usually in the form of bubbles, which advect with the flow; see Figure 2.10. These bubbles implode once the local static pressure increases above the fluid vapor pressure P_v. This implosion is a very energetic event that erodes surrounding surfaces over time.

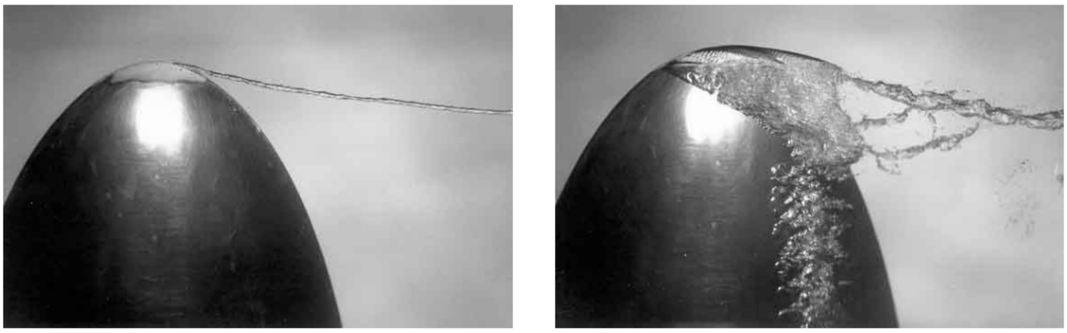

Figure 2.10: Cavitating tip vortices generated by a hydrofoil. [19]

Cavitation and bubble dynamics can be studied by considering the growth and collapse of cavitation nuclei as spherical bubbles in an unbounded, incompressible liquid. Although this idealized model simplifies the analysis, it still captures the essential physics of bubble-liquid interactions. However, real-world scenarios may deviate significantly, especially during the non-linear initial growth and final collapse stages. Factors such as proximity to boundaries, interactions with other bubbles, heat transfer, flow shearing effects, and cavity interface instabilities can all cause deviations from this simplification. Despite these complexities, focusing on spherical cavities allows for a more straightforward analysis while retaining the critical aspects of the phenomena. Under these assumptions, the bubble radius R is governed by the Rayleigh–Plesset equation [19].

$$\frac{P_B(t) - P_\infty(t)}{\rho_L} = R\frac{d^2R}{dt^2} + \frac{3}{2}\left(\frac{dR}{dt}\right)^2 + \frac{4\nu_L}{R}\frac{dR}{dt} + \frac{2S}{\rho_L R} \tag{2.13}$$

Where P_B is the bubble pressure, P_∞ is the free-stream static pressure, ν_L is the kinematic viscosity, and S is the surface tension. Note that thermal effects are not modeled in the above equation. We can see that bubble growth is a transient phenomenon, and even with this simplified model, the dynamics are non-linear. Furthermore, this model does not account for 'cavitation nuclei' or small dispersed flow impurities commonly present in industrial processes that strongly promote early cavitation inception at pressures above the vapor pressure P_v. In light of this, the detailed analysis of cavitation is regarded as complex and out of scope for this project.

However, from Equation 2.13, we can infer that the liquid density ρ_L and the upstream pressure P_∞ directly influence the bubble growth rate R, and thus the intensity of cavitation. As the density ρ_L increases, the bubble radius and growth rate decrease; as the upstream pressure P_∞ increases, the bubble radius and growth decrease.

2.5.1 Practical Approach

Given that the microscopic analysis of cavitation is complex, we turn to a more practical, macroscopic analysis. We begin by defining the available *net positive suction head* NPSH of a pump as the margin between the inlet absolute total pressure and the liquid absolute vapor pressure, normalized by density:

$$\boxed{\mathrm{NPSH}_A = \frac{P_{t_0} - P_v}{\rho g} = \left(\frac{P_0}{\rho g} + \frac{V_0^2}{2g}\right) - \frac{P_v}{\rho g} \qquad (2.14)}$$

In practice, if the static pressure P, mass flow $\dot{m}$, and pipe diameter d_0 are known at the inlet, the net positive suction head *available* NPSH_A in the pump can be found for a given fluid vapor pressure. Confusingly, NPSH is calculated with the *total* pressure of the fluid, even though only the static pressure affects cavitation inception, as seen in Equation 2.13. This is a convention that allows pump manufacturers to prescribe an NPSH value with a defined inlet pipe size.

The point at which the total pressure reaches a minimum, or $P_0 = P_v$, is called *'cavitation inception'* (NPSH_i), and it is observed when the first vapor bubbles are generated. If the inlet pressure is decreased even further, the cavitation extent and intensity will increase, causing a drop in performance (from blockage due to cavitation and work lost changing the fluid phase). It is important to remember that different values of NPSH may be allowed depending on the design constraints. To this extent, several cavitation criteria have been established:

- **$\mathbf{NPSH}_i$**: Visual cavitation inception
- **$\mathbf{NPSH}_0$**: Beginning of head drop
- **$\mathbf{NPSH}_1$**: Impeller head drop of 1%
- **$\mathbf{NPSH}_3$**: Impeller head drop of 3%
- **$\mathbf{NPSH}_{\mathrm{FC}}$**: 'Full Cavitation' or 'Breakdown'. The impeller head is severely reduced and operates largely in 2-phase flow.
- **Other**: Prescribed drop in efficiency, loss of material due to erosion, noise level, or service life duration.

The most widely used cavitation criterion is NPSH_3, not because it is a technically relevant condition but because it is easier to measure. The behavior of cavitation inception can be visualized in Figure 2.11, with the cavitation coefficient σ as a function of the head coefficient ψ. Note that each $\sigma - \psi$ curve is a function of the flow coefficient ϕ.

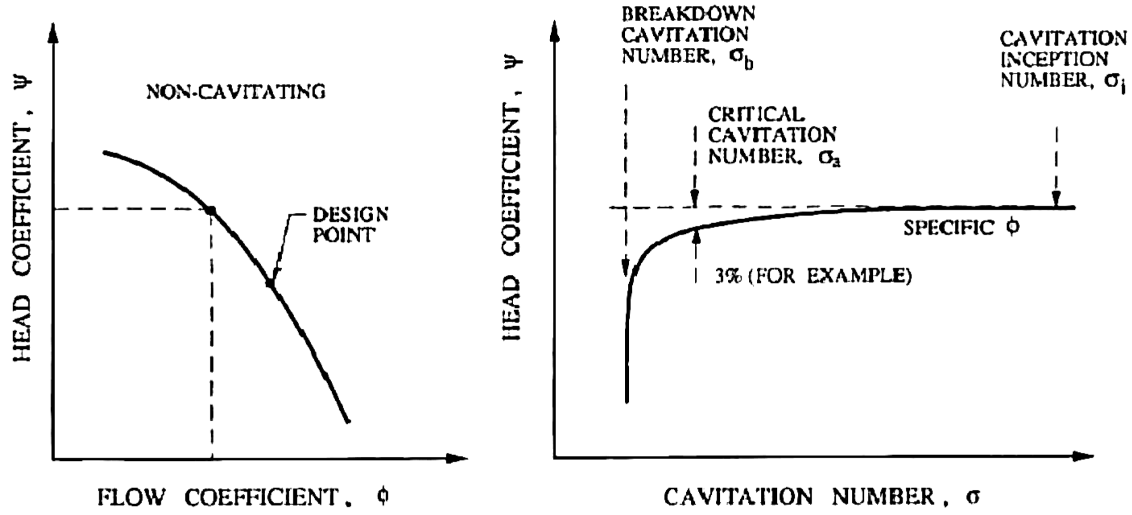

Figure 2.11: Schematic of cavitating performance [13]

With the fundamental parameter for cavitation scaling is the Euler number σ (also known as the cavitation number):

$$\sigma = \frac{P_0 - P_v}{1/2 \cdot \rho_L \cdot V_0^2} \tag{2.15}$$

As the fluid passes through the inlet of the impeller, there are changes in the static pressure due to the rotation of the impeller and the blade profile shape, analogous to the flow around an airfoil. The maximum suction pressure is experienced near the leading edge of the blade's suction side, causing the flow to accelerate rapidly to compensate for the pressure reduction. As the vapor cavity extends downstream of the impeller, the pressure gradually increases until the static pressure rises again above the liquid vapor pressure, and the cavity collapses. This bubble implosion creates violent shock waves, causing pitting and erosion on any surrounding structure.

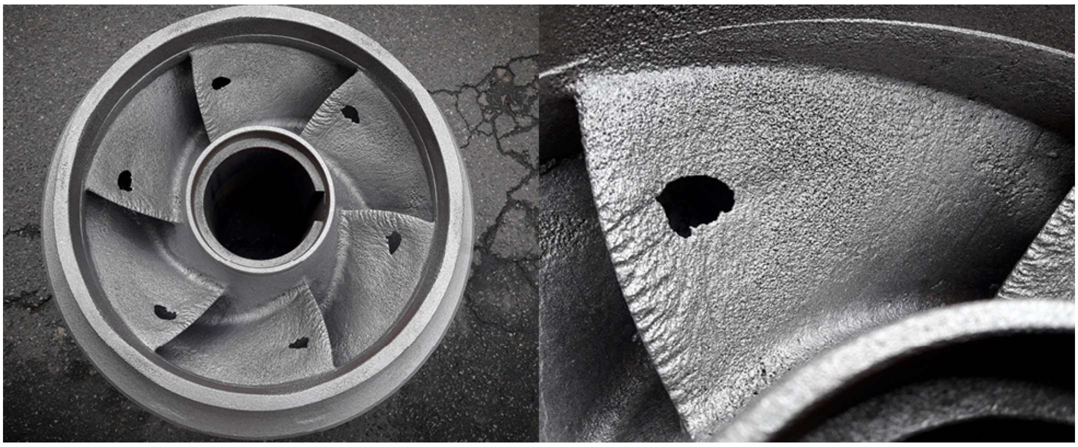

Figure 2.12: Pitting on an impeller due to cavitation

3

Design Methodology

First, a brief overview of various design approaches is given to help readers understand each method's strengths and weaknesses. Then, a step-by-step explanation of the selected method is presented.

3.1 Approach

The flow within a typical turbomachine is often a complex three-dimensional turbulent flow involving either compressible or incompressible fluids. Sometimes, the fluid may be formed by a two-phase or two-component mixture of liquid, vapor, gas, or solid particles. Analyzing these intricate flow processes, especially within rotating impellers, typically requires numerical simulations.

Preliminary design analysis relies on fundamental fluid mechanics and thermodynamics principles with necessary simplifications and assumptions. The Euler equation, derived from the momentum equation applied to fluid mechanics, is crucial for relating energy transfer between the flowing fluid and the rotating impeller. When physical relationships are unavailable, empirical models are often necessary to model losses due to friction and three-dimensional viscous effects.

For the past decade, the availability and affordability of computational fluid dynamics (CFD) software has facilitated more advanced design and analysis of turbomachines [59]. Today, many turbomachinery designers can either develop their own or choose from many publicly available (often commercial) software design programs. When designing a new turbomachinery component, various design paths can be followed:

- Refining an existing component: Surfaces are modified via feedback loops coupled with high-fidelity CFD simulations through an optimizer. This procedure is computationally expensive.
- Designing from first principles and validated empirical correlations: The performance and geometry of the component are derived from the basic laws of physics. Knowledge gaps can be filled with validated datasets or numerical simulations. This method is used in this work and has proven to be computationally inexpensive.
- Making use of data-driven methods: Large component families can be generated and classified with various criteria and made use of with an optimization technique of choice:

Design of Experiments (DoE), Response Surfaces, Genetic Algorithms, Neural Networks, and Multi-Objective Optimization algorithms. This is an emerging design methodology with proven results.

It is clear that expensive numerical simulations should be used sparingly to improve the last percentage points and validate models. This idea is represented in Figure 3.1 below. A design can be brought closely to the maximum efficiency point without numerical simulations.

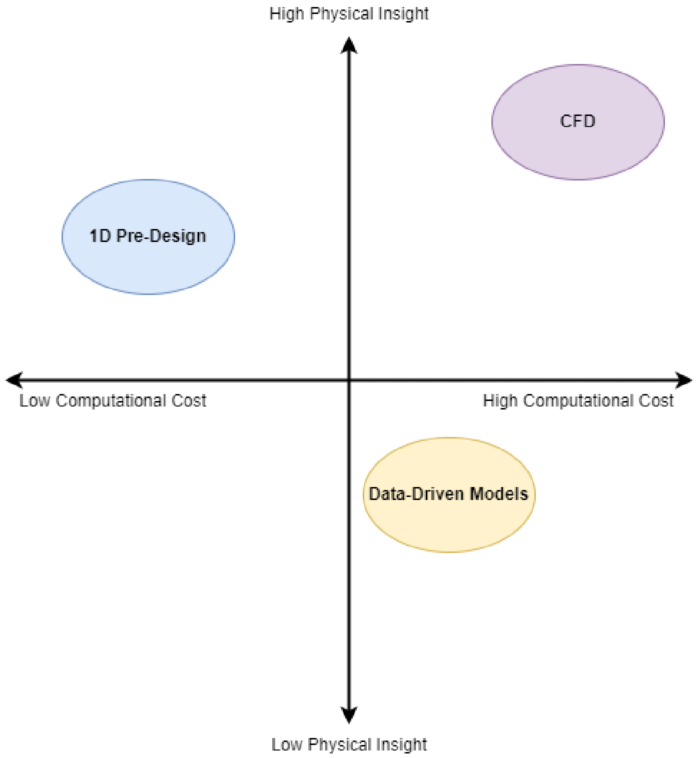

Figure 3.1: Comparing the computational cost against physical insight of various design approaches.

This work explores the use of 1D design methodologies in the pre-design stages of noncavitating centrifugal turbopumps using validated loss models. Then, a CFD study to assess the validity of the predictions is performed.

3.2 Performance Specification

Basic operational requirements are needed to design a pump: the rotational speed n, volumetric flow rate Q (or mass flow rate $\dot{m}$), and on-design head H (or pressure rise ΔP_t). These quantities are the basis for calculating the pump's specific speed n_q.

$$n_q = n \cdot \frac{\sqrt{Q}}{H^{0.75}} = n \cdot \frac{\sqrt{\dot{m}/\rho_0}}{H^{0.75}} \tag{3.1}$$

Various turbomachines are classified based on their specific speed. The *Cordier* Diagram illustrates this (Note $\Omega_s = n_q/(52.92 \text{ min}^{-1})$):

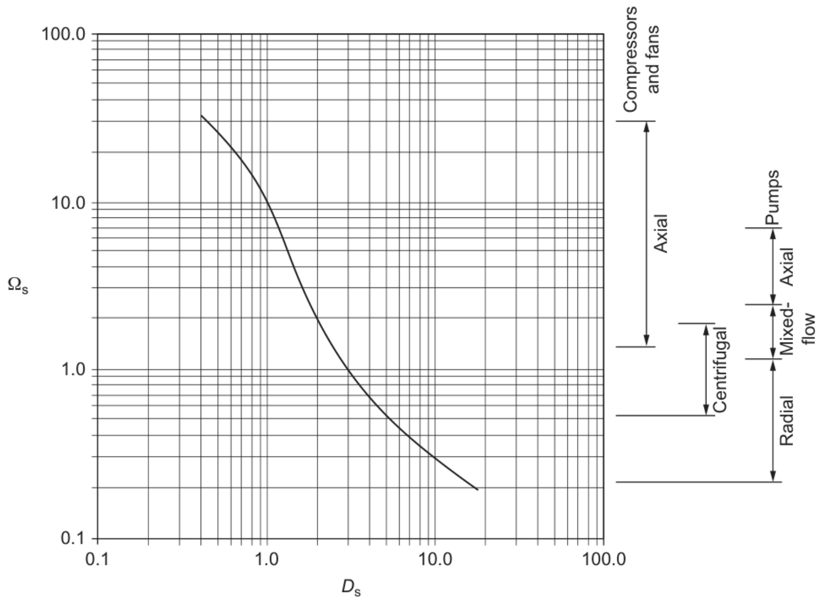

Figure 3.2: Cordier Diagram [25].

In addition, knowledge (or assumption) of the inlet approach flow angle α_0 and meridional velocity V_m distribution is required. The approach flow is typically assumed axial $\alpha_0 = 0°$ and the velocity distribution constant over the inlet area.

It is now possible to calculate an important variable–the isentropic head H_{is} at the best efficiency point (BEP)–if not explicitly known. This quantity predicts the head developed across the pump *without* any kind of losses.

$$H_{is} = \frac{h_{t1,is} - h_{t0}}{g} = \frac{P_{t1,is} - P_{t0}}{\rho g} = \frac{P_{1,is} - P_0}{\rho g} + \frac{V_{1,is} - V_0}{2g} \tag{3.2}$$

Lastly, two non-dimensional parameters used to classify turbomachines are the flow coefficient ϕ, and the work (head) coefficient ψ:

$$\phi = \frac{V_m}{U} \tag{3.3}$$

$$\psi = \frac{\Delta h_0}{U^2} = \frac{U \cdot (V_{0t} - V_{1t})}{U^2} = \frac{(V_{0t} - V_{1t})}{U} \tag{3.4}$$

3.3 Outlet Diameter

Given that the isentropic work required on the fluid is known from Equation 3.2, selecting a work coefficient (head coefficient) ψ to obtain the outlet diameter d_1 is possible. If the work coefficient is not prescribed, it can be chosen as a function of specific speed n_q by examining performance trends from multiple pump manufacturers.

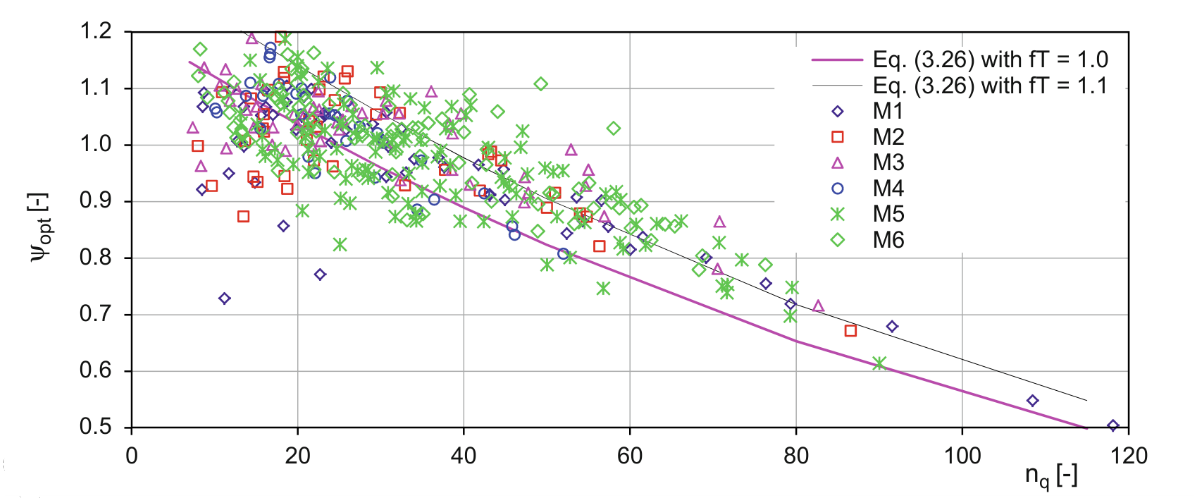

Figure 3.3: Head coefficient values for single-stage volute pumps from various pump manufacturers (M1-M6) [33].

The trends are expressed with Equation 3.5, where f_T can be chosen between 1.0-1.1. For multi-stage pumps $f_T = 1.0$ is appropriate, and low-head pumps can be designed with $f_T = 1.1$ [33].

$$\psi = f_T \cdot \frac{1}{2} \cdot 1.21 \cdot e^{-0.007713 \cdot n_q} \tag{3.5}$$

Note that two conventions for the work coefficient ψ exist in literature: $\psi = gH_{is}/U_1^2$, and $\psi = 2gH_{is}/U_1^2$. This work is consistent with the former definition.

Finally, from the definition of work coefficient ψ the impeller outlet diameter d_1 can be found with Equation 3.6, recalling that $U_1 = \omega \cdot r_1$ and $\omega = \frac{2\pi}{60}$.

$$d_1 = \frac{2}{\omega} \cdot \sqrt{\frac{g \cdot H_{is}}{\psi}} = \frac{60}{n \cdot \pi} \cdot \sqrt{\frac{g \cdot H_{is}}{\psi}} \tag{3.6}$$

3.4 Number of Blades

The selection of blade number N_{bl} can be chosen depending on various criteria: Many blades result in low blade loading but higher friction losses while choosing fewer blades results in higher blade loading, but the hydraulic losses may rise due to increased secondary flows and stronger deviation between blade and flow direction. Additionally, impellers with a very low blade pitch $s = \pi \cdot d_{0,s}/N_{bl}$ may be challenging to manufacture even with 5-axis CNC mills. This is especially the case for small shrouded impellers with splitter blades.

Typically, radial impellers with specific speeds in the range of $10 < n_1 < 120$ have between 5-7 main blades. If only a narrow operating range is required where the pump stability is not of importance, pumps with up to 9 (radial) blades have been designed. For suction impellers with high specific suction speed n_{ss} and flat $NPSH_3$ curves, it is recommended to select 5 or 6 main blades, as 7 or more become unstable [33].

Additionally, Pfleiderer [24] developed an empirical expression to obtain the number of blades. However, this should be only taken as a hint, as this equation disregards any criteria discussed above.

$$N_{bl} = 6.5 \cdot \frac{d_1 + d_0}{d_1 - d_0} \cdot \sin\left(\frac{\beta_{0B} + \beta_{1B}}{2}\right) \tag{3.7}$$

More recently, [63] developed a new method to estimate an optimum blade number considering slip, the boundary layer's influence over the blade, and the nonlinear velocity distribution.

$$N_{bl} = \frac{\pi \cdot \sin\beta_{1B}}{1 - \frac{V_{1m}}{U_1 \cdot t \cdot g \cdot \beta_{1B}[\text{deg}]} - \frac{g \cdot H_{is}}{\eta_h \cdot U_1}} \tag{3.8}$$

These equations use the blade angles β_B. As they are not defined yet, $\beta_{1B} = 25°$ can be chosen as an initial value, based on an optimum range of 23-27° recommended in a review [52]. Adding splitter blades–effectively doubling the number of blades at the outlet–has shown to improve performance in small-scale turbopumps [76].

3.5 Inlet Design

As the first station encountered by the fluid, the inlet has a strong influence on performance, efficiency, and risk of cavitation. At best, cavitation can result in a performance decrease and, at worst, in structural failure. A common approach for pump designers is to identify the conditions for cavitation inception NPSH$_i$ and operate as closely as possible to them. Other cavitation criteria, e.g., NPSH$_3$, are also valid depending on the design constraints and the amount of allowable cavitation.

The following figure illustrates well the cavitation sensitivity of the inlet. The link between the local pressure drop at the leading edge with the flow properties and geometrical variables makes cavitation avoidance possible.

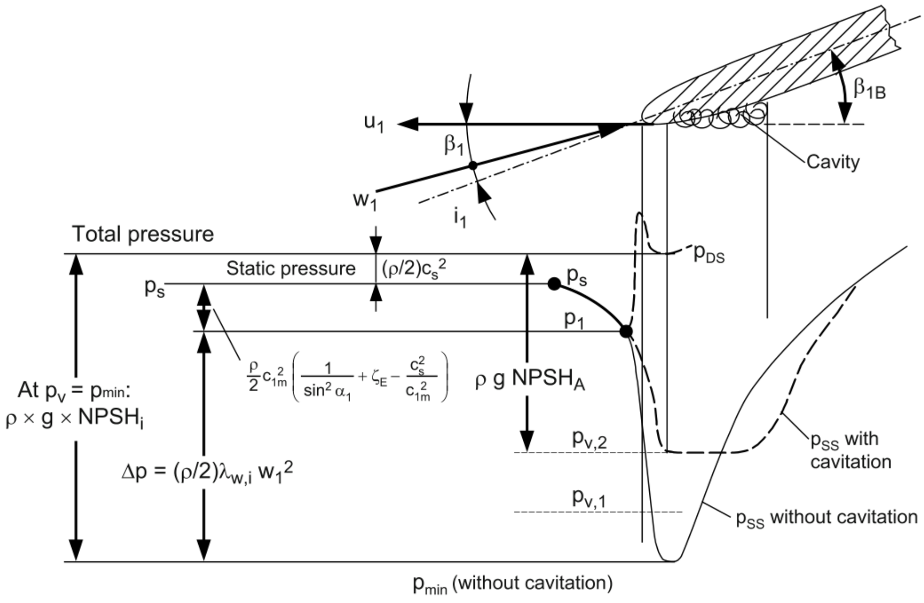

Figure 3.4: Cavitation at the impeller blade leading edge [33]

The main parameters to consider during inlet design are the inlet shroud (outer) diameter r_{1s}, the hub (inner) diameter r_{1h}, the blade inlet angle β_{0t}, blade leading edge thickness t_{le}, and main blade number N_{bl}. Additionally, the inlet size parameter $k_n = 1 - (\frac{r_{1h}}{r_{1s}})^2$ can be used to link the inlet hub and shroud sizes.

3.5.1 Hub Diameter $d_{0,h}$

Two methods are available to size the inlet hub diameter:

Method A: Maximum shaft shear stress

The minimum eye hub diameter $d_{0,h}$ is limited by the shaft size required to transmit the torque into the impeller. The maximum shaft diameter (minimum impeller eye diameter) can be calculated if the allowable shear stress τ_{al} of the shaft's material is known. A safety factor SF > 1 is recommended.

$$d_{0,h} = \text{SF} \cdot \left(\frac{16 \cdot P_{\text{max}}}{\pi \cdot \omega \cdot \tau_{\text{al}}} \right)^{1/3} \tag{3.9}$$

The maximum power P_{max} can be calculated:

$$P_{max} = \dot{m} \cdot \Delta h_t = \rho \cdot Q_{\text{max}} \cdot g \cdot H_{\text{max}} \tag{3.10}$$

Method B: Impeller shape factor

Alternatively, the impeller shape factor k_n can be used to size the inlet eye diameter. The shape factor links the inlet shroud and hub diameters:

$$k_n = 1 - \left(\frac{R_{1,\text{hub}}}{R_{1,\text{shroud}}} \right)^2 \tag{3.11}$$

The shape factor is usually kept in the bounds of $0.65 < k_n < 0.95$, with 0.8775 being a commonly used value [15]. By choosing k_n, the hub and shroud diameters can be found through the conservation of mass. As this depends on the inlet shroud diameter $d_{0,s}$, this procedure is continued in subsection 3.5.2.

3.5.2 Shroud Diameter $d_{0,s}$

There are various methods to design the inlet shroud diameter based on different criteria related to cavitation:

Method A: Minimum Relative Velocity

This design tends to minimize leakage, friction and shock losses. It is recommended when the available $NPSH_A$ is sufficiently high so that cavitation is avoided. The relative velocity at the inlet W_0 can be expressed as:

$$W_0 = \sqrt{V_{0m}^2 + \left(U_0 - \frac{V_{0m}}{\tan \alpha_0} \right)^2} \tag{3.12}$$

with absolute meridional velocity V_{0m} and tip velocity U_0:

$$V_{0m} = \frac{4 \cdot \dot{m}}{\pi \cdot \rho \cdot (d_1^2 - d_0^2)} = \frac{\dot{m}}{\pi \cdot \rho \cdot r_{0,s} \cdot k_n} \tag{3.13}$$

$$U_0 = d_{0,s} \cdot \pi \cdot \frac{n}{60} \tag{3.14}$$

Inserting Equation 3.13 and Equation 3.14 into Equation 3.12, the expression can be differentiated with respect to d_0. Setting then $dw_0/dd_0 = 0$ allows for the maximum relative velocity given a constant axial flow velocity:

$$d_{0,s} = d_1 \cdot f_{d_1} \sqrt{\left(\frac{d_{0,h}}{d_1}\right)^2 + 1.48 \times 10^{-3} \cdot \psi \cdot \frac{n_q^{1.33}}{(\eta_v \cdot \delta_r)^{0.67}}} \tag{3.15}$$

Or, more conveniently, using the impeller factor k_n:

$$d_{0,s} = d_1 \cdot \sqrt{\frac{1.48 \times 10^{-3} \cdot \psi \cdot \frac{n_q^{1.33}}{(\eta_v \cdot \delta_r)^{0.67}}}{f_d^{-2} + k_n - 1}} \tag{3.16}$$

Pre-rotation (if any) is covered iteratively by the swirl number δ_r. Note that assuming axial inflow gives $\delta_r = 1$.

$$\delta_r = 1 - \frac{V_{1m} \cdot \tan \alpha_1}{U_{1m}} \tag{3.17}$$

The inlet diameter is designed slightly above the minimum to allow for secondary effects, such as boundary layer blockage and uneven velocity distributions [33]. Recommendations for this f_{d1} factor are given:

- Normal impellers: f_{d1} = [1.15, 1.05]
- Suction impellers: f_{d1} = [1.25, 1.15]

Method B: Selected Specific Suction Speed n_{ss}

The inlet can also be sized by selecting an appropriate suction specific speed n_{ss} value. The suction specific is a dimensionless parameter describing the relationship between the rotational speed n, the flow rate Q, and the net positive suction head required NPSH_R of an impeller.

$$n_{ss} = n \cdot \frac{\sqrt{Q}}{\text{NSPH}_R^{0.75}} \tag{3.18}$$

Standard values are listed in Table 3.5.2 below:

Type	Lower range	Upper range
Standard suction impeller	160	220
Suction impeller, axial inflow	220	280
Suction impeller, cont. shaft	180	240
High pressure pump	160	190
Standard inducer	400	700
Rocket inducer	-	>>1000

Table 3.1: Common values for specific suction speed n_{ss} [33]

Now, the *normalized* suction specific speed n_{ss}^{**} is defined as:

$$n_{ss}^{**} = \frac{n_{ss}}{\sqrt{k_n}} * \left(\frac{n_{q,\text{ref}}}{n_q}\right)^{0.19} \tag{3.19}$$

Through experiments, many data points for impellers in the range $n_q = 10 - 160$ have been gathered and plotted against the approach flow angle β_{1a} in Figure 3.5.

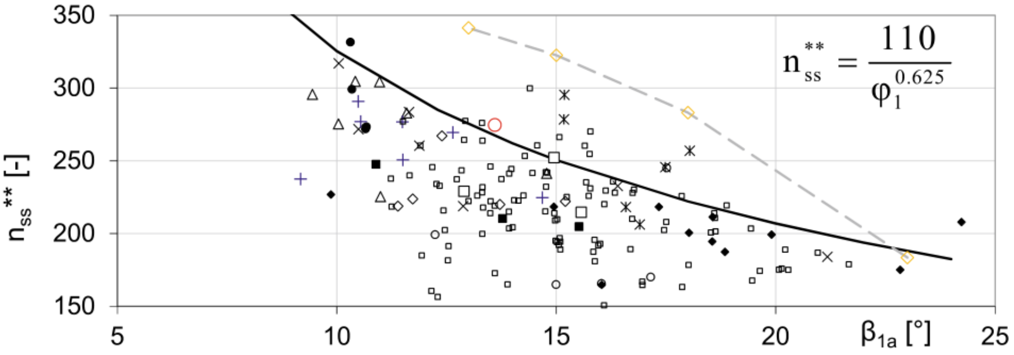

Figure 3.5: Normalized suction specific speed as function of the shockless flow angle at the outer streamline, with $n_{q,\text{ref}} = 27$

To determine the inlet diameter of an impeller for selected values of n_q, n_{ss} and d_n/d_1 (or k_n), it is possible to determine n_{ss}^{**} from Equation 3.19. So, the following expression can be derived to find ψ and β_{0B}.

$$\psi = \tan(\beta_{0B}) = k_n^{0.8} \cdot \left(\frac{110}{n_{ss}}\right)^{1.6} \cdot \left(\frac{n_q}{27}\right)^{0.3} \tag{3.20}$$

With this relationship, obtaining the leading edge blade angle β_{0B} is now possible. Finally, the inlet shroud diameter $d_{0,s}$ can be obtained by rearranging the velocity triangle with the following expression:

$$d_{0,s} = 2.9 \cdot \left(\frac{\dot{m}}{\rho \cdot n \cdot k_n \cdot \tan\beta_1} \cdot \left(1 + \frac{\tan\beta_1}{\tan\alpha_1}\right)\right)^{1/3} \tag{3.21}$$

Method C: Minimum Required Suction Head NPSH$_R$

The inlet blade tip of pumps is the most vulnerable location for cavitation. At the inception of cavitation, at some point on the blade's surface, the pressure is equal to the vapor pressure. Right upstream of the impeller inlet:

$$p_0 = p_{t0} - \sigma_b \cdot \left(\frac{1}{2} \cdot \rho \cdot W_1^2\right) \tag{3.22}$$

With the blade cavitation coefficient σ_b corresponding to the point of cavitation inception at NPSH$_i$. Experiments have shown that it usually lies in the range of $0.2 \leq \sigma_b \leq 0.4$ [58]. By making use of the velocity triangles and Equation 3.22, with NPSH$_R$ measured at the shroud radius, the following relationship can be written:

$$\mathrm{NPSH}_R = \frac{p_{t0} - p_v}{\rho} = \frac{1}{2} \cdot V_{0m}^2 + \frac{1}{2} \cdot \sigma_b \cdot W_1^2 = \frac{1}{2} \cdot V_{0m}^2 \cdot (1 + \sigma_b) + \frac{1}{2} \cdot \sigma_b \cdot U_{1,s}^2 \tag{3.23}$$

By inserting the suction specific speed $n_{ss} = n \cdot \frac{\sqrt{Q}}{\mathrm{NPSH}_R^{0.75}}$, volumetric flow $Q = \pi \cdot k_n \cdot r_{0,s}^2 \cdot V_{1m}$, and flow coefficient $\phi = V_{0m}/U_{0,s}$ into Equation 3.23:

$$\frac{n_{ss}^2}{\pi \cdot k_n} = \frac{U_{0,s}^2 \cdot V_{0m}}{\left[\frac{1}{2}\left(V_{0m}^2 \cdot (1 + \sigma_b) + \sigma_b \cdot U_{1,s}^2\right)\right]^{3/2}} = \frac{\phi}{\left[\frac{1}{2}\left(\phi^2 \cdot (1 + \sigma_b) + \sigma_b\right)\right]^{3/2}} \tag{3.24}$$

By taking the derivative of Equation 3.24 with respect to ϕ and setting it to zero, the maximum n_{ss} for a given axial inflow V_{0m} and blade cavitation coefficient σ_b can be found:

$$n_{ss}^2 = \frac{3.42 \cdot k_n}{\sigma_b \cdot \sqrt{1 + \sigma_b}} \tag{3.25}$$

The optimum flow coefficient ϕ and NPSH$_R$ under these conditions can be found with:

$$\phi = \sqrt{\frac{\sigma_b}{2 \cdot (1 + \sigma_b)}} \tag{3.26}$$

$$\mathrm{NPSH}_R = \frac{3}{4} \cdot \sigma_b \cdot U_{0,s}^2 \tag{3.27}$$

With these relationships, one can choose or determine a blade cavitation coefficient σ_b and find the optimal flow coefficient ϕ. Then, the inlet blade angle β_{0B} and shroud diameter $d_{0,s}$ can be found with Equation 3.20 and Equation 3.21, respectively.

Method D: Selected λ−Coefficients

Similar to the method in Equation 3.5.2, the blade cavitation coefficient σ_b can be decomposed into two λ parameters:

$$\sigma_b = (\lambda_c + \lambda_w) \cdot \phi_1^2 + \lambda_w \cdot \left(1 - \frac{\phi_1}{\tan \alpha_1}\right)^2 \tag{3.28}$$

One can choose a σ_b value and calculate a λ coefficient pair, or vice-versa. The impeller blade coefficients can be described as:

- λ_c: Suction pressure coefficient for absolute velocity V (inflow acceleration and losses). Typically 1.1 for axial inflow.
- λ_w: Suction pressure coefficient for relative velocity W (pressure drop at leading edge). Typically 0.10-0.30 for a standard impeller and 0.03-0.06 for inducers.

As seen in Figure 3.4, the minimum local pressure at the impeller inlet is a result of both the acceleration of the main flow and the losses in the inlet, and a local velocity increase from the flow around the blade leading edge in part due to blockage. Similar to Equation 3.23, the following relationship is frequently applied:

$$\mathrm{NPSH}_R = \lambda_c \cdot \frac{V_{1m}^2}{2g} + \lambda_w \cdot \frac{W_1^2}{2g} \tag{3.29}$$

Once an appropriate λ pair has been chosen, the optimal inlet diameter d_1 can be found via Equation 3.30

$$d_{0,s} = 3.25 \cdot \left(\frac{Q}{n \cdot k_n}\right)^{\frac{1}{3}} \cdot \left(\frac{\lambda_c + \lambda_w}{\lambda_w}\right)^{\frac{1}{6}} \tag{3.30}$$

Furthermore, given a size parameter k_n, the optimal flow coefficient ϕ, and specific suction speed n_{ss} can be found with Equation 3.31, and Equation 3.32 below:

$$\phi_1 = \sqrt{\frac{\lambda_w}{2(\lambda_c + \lambda_w)}} \tag{3.31}$$

$$n_{ss} = \frac{98}{(\lambda_c + \lambda_w)^{0.25}} \cdot \left(\frac{k_n}{\lambda_w}\right)^{0.5} \tag{3.32}$$

Note that these equations only apply to inflow without prerotation.

λ-Coefficient Estimation

The λ-coefficients can be assumed, determined experimentally, or found through empirical correlations. The biggest uncertainty lies with the λ_w coefficient as $W_0 >> V_0$. Experimental tests have shown that λ_w depends on the absolute blade angle β_1 (Figure 3.6). λ_c is typically 1.1 for axial-inflow impellers and does not depend on the operating conditions.

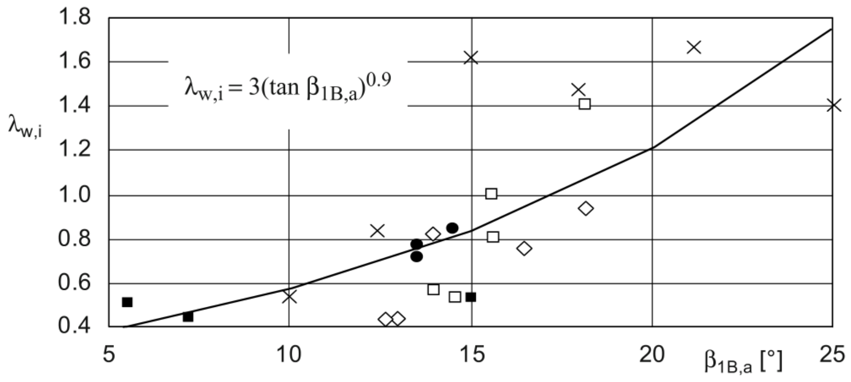

Figure 3.6: $\lambda_{w,i}$ for 3% head drop as a function of the flow angle at the outer streamline [33]

This correlation applies to pumps at the BEP with shockless inflow.

3.5.3 Inlet Blade Angle β_{0B}

It is now possible to calculate all quantities of the inlet velocity triangle. Recalling that $W_t = V_t - U$ and $W_m = V_m$, the relative *flow* angle β_0 can be found:

$$\beta_0 = \arctan \frac{W_{0t}}{W_{0m}} \tag{3.33}$$

This flow angle assumes a perfectly guided flow with no disturbances. However, setting the blade angle to the flow angle $\beta_{0B} = \beta_0$ would result in a non-zero incidence. The effect of blade incidence and blockage must be accounted for to address this.

Blockage

As the flow transitions from the inlet pipe to the leading edge of the impeller blades, there is an instant reduction in passage area, which in turn has an effect on the meridional flow velocity and, consequently, the inlet velocity triangle of the impeller. See Figure 3.7 below. Inducer impellers have blades with very thin leading edges to improve suction performance (6-10% of nominal blade thickness). This is also true for the outlet station of the impeller, however, the flow experiences a sudden deceleration leaving the impeller. Furthermore, the effect of blade blockage at the impeller outlet is less considerable as the ratio of blade thickness to circumferential outlet area is much greater than at the inlet.

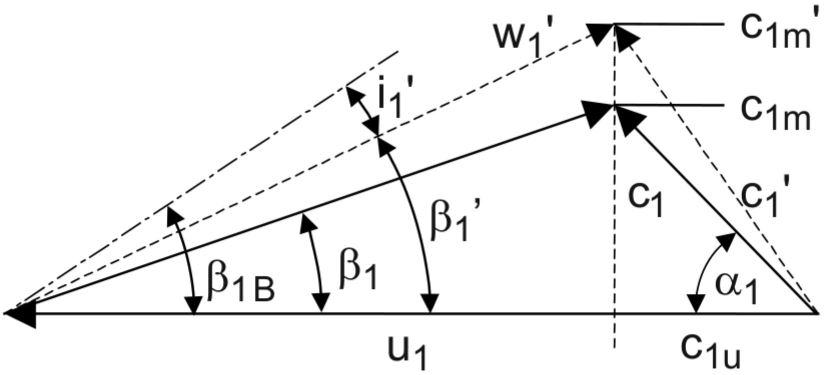

Figure 3.7: Inlet blockage [33]

Furthermore, considering blade blockage for blade angle calculations or not and in which way is a controversial issue. Exactly at the blade leading edge, the thickness is 0 due to the rounding of the blade edge. Immediately after the blade's leading edge (or before the blade's trailing edge), the blade is blocking the flow in a certain manner. But, this blockage depends on the blade thickness, angle, and distribution, which is more complex than considering a simple blade angle.

However, in this study, the influence of blade blockage at the inlet is non-negligible, as it measurably affects the suction performance. An incorrect estimation of the blockage can lead to an incorrect velocity triangle, degrade performance, and produce cavitation. As seen in Figure 3.7, the solid velocity triangles are just outside the blade passage, and the dashed vectors are just after the blade's leading edge. The meridional velocity component V_{0m} increases due to the area reduction, which changes the blade metal angle β_{0B}. To begin with, the flow angle without blockage β_0 is computed:

$$\beta_0 = \arctan \frac{W_{0m}}{W_{0t}} = \arctan \frac{V_{0m}}{V_{0t} - U_1} \tag{3.34}$$

The blade thickness σ_1 can be considered in either the absolute or relative reference frames:

$$\sigma_0 = \frac{t_{le}}{\cos \beta_{0B}} \tag{3.35}$$

$$\sigma_0 = t_{le} \tag{3.36}$$

For the remainder of this work, Equation 3.35 is considered, accounting for β_{0B}. Next, the inlet blade blockage factor τ_0 and pitch t_0 can be found with:

$$\tau_0 = \frac{t_0}{t_0 - \sigma_0} \tag{3.37}$$

$$t_0 = \frac{\pi \cdot d_{0,s}}{N_{bl}} \tag{3.38}$$

Then, the meridional velocity component V'_{0m} (inside of the blade passage) can be found with:

$$V'_{0m} = \tau_0 \cdot \frac{\dot{m}}{\rho \cdot \pi \cdot r_s^2 \cdot k_n} \tag{3.39}$$

Incidence

Blade incidence i is defined as the difference between the blade angle β_{0B} and the flow angle β_0:

$$i = \beta_{0B} - \beta_0 \tag{3.40}$$

Generally, inflow without incidence is intended $i = 0°$ at the BEP. If $i \neq 0°$, the flow around the leading edge accelerates unevenly, creating high local velocities and lower static pressure, which could increase or decrease the risk of cavitation:

- Positive incidence $i > 0$: $\beta_0 < \beta_{0B}$ – stagnation point on pressure side
- Negative incidence $i < 0$: $\beta_0 > \beta_{0B}$ – stagnation point on suction side

At off-design conditions, the inflow angle β_0 changes, and the incidence inevitably deviates from zero. By considering the effect of blockage and choosing an incidence value for the best efficiency point (BEP) of the pump, the blade metal angle can be calculated:

$$\boxed{\beta_{0B} = \beta_0' + i_0' = \arctan \frac{V_{0m}'}{V_{0t} - U_0} + i_0'} \tag{3.41}$$

Note that the blade metal angle, incidence, and the leading edge blade thickness influence the blockage factor. As τ_0 is a function of β_{0B}, the equations above must be solved iteratively to converge onto a valid configuration.

3.6 Outlet Design

The Euler head equation drives the design of the outlet station:

$$H = \frac{\Delta P_t}{\rho \cdot g} = \frac{h_{t1} - h_{t0}}{g} = \frac{U_1 \cdot V_{1t} - U_{0,s} \cdot V_{0t}}{g} \tag{3.42}$$

First, the isentropic head is calculated assuming no inlet pre-swirl ($V_{0t} = 0$). Since the inlet pressure $P_{t,0}$, and pressure rise ΔPt (or pressure ratio β_{tt}) are known, the outlet isentropic pressure ratio $P_{t,1}$ can be computed. Now, per the definition of the head coefficient ψ:

$$\psi = \frac{2 \cdot g \cdot H}{U_1^2} \tag{3.43}$$

It allows for rearrangement of the equation to find the outlet diameter d_1:

$$\boxed{d_1 = \frac{60}{\pi n} \cdot \sqrt{\frac{2gH}{\psi}}} \tag{3.44}$$

Since the head H and outlet radius r_1 have been found from Equation 3.42, and Equation 3.44 respectively, the impeller outlet circumferential velocity U_1 and the flow outlet circumferential velocity V_{1t} can be calculated–assuming no inlet prerotation.

$$U_1 = \frac{d_1}{2} \cdot \omega = \frac{d_1}{2} \cdot \frac{60}{2\pi} \cdot n \tag{3.45}$$

$$V_{1t} = \frac{H \cdot g}{U_1} \tag{3.46}$$

3.6.1 Width b_1

Now, since blade outlet angle β_{1B} and outlet width b_1 cannot be selected independently of one another, they must be matched so that the desired head through the outlet velocity V_{1t} is achieved with a stable Q-H-curve. The choice of each of these will determine the shape of the outlet velocity triangle.

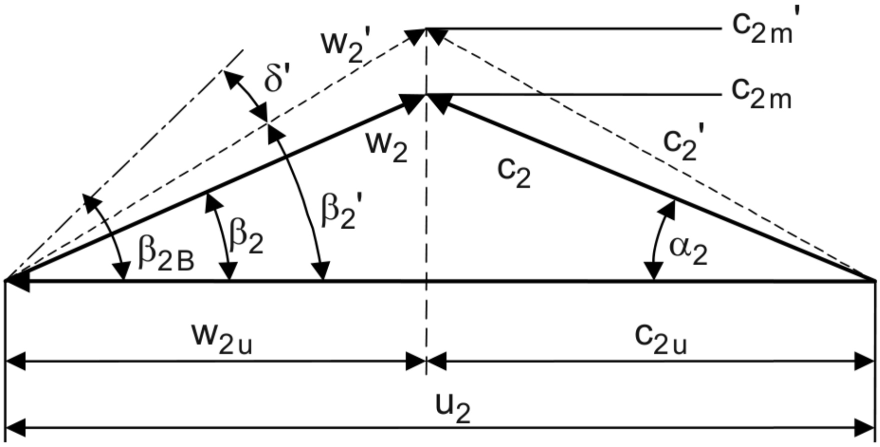

Figure 3.8: Outlet velocity triangle accounting for blockage and slip. [33]

Increasing the width of the outlet b_1 reduces the meridional velocity V_{1m}, leading to an increase in tangential velocity V_{1t} and consequently the head, unless flow separation occurs. Given specific values for the outlet angle and blade number, widening the outlet increases the head, making the Q-H curve flatter. It is crucial to maintain stability by ensuring $b_1 < b_0$. Since these effects cannot be precisely calculated theoretically, the relative outlet width $b_1^* = b_1/d_{1a}$ is typically chosen empirically. To optimize impeller discharge flow uniformity and minimize turbulent losses, a low b_1^* within the limits of Q-H curve stability is a good choice. Figure 3.9 provides a range for b_1^* based on empirical data.

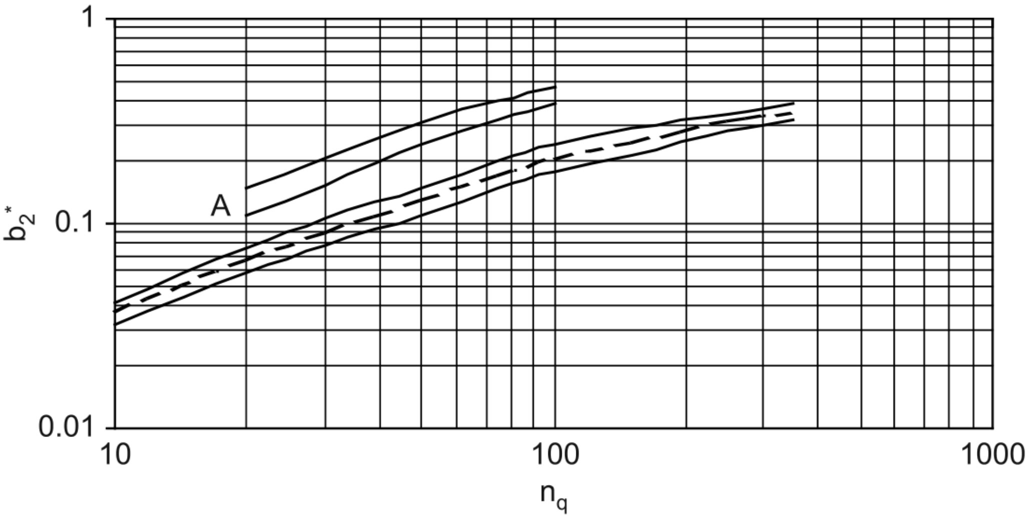

Figure 3.9: Impeller outlet width ratio data. ('A' curve is for sewage pumps) [33]

The mean curve for outlet width in Figure 3.9 can be approximated using Equation 3.47.

$$\boxed{b_1 = d_1 \cdot \left[0.017 + 0.262 \cdot \frac{n_q}{100} - 0.08 \cdot \left(\frac{n_q}{100}\right)^2 + 0.0093 \cdot \left(\frac{n_q}{100}\right)^3\right] \qquad (3.47)}$$

This allows the calculation of the outlet velocity triangle without accounting for slip and blockage (outside the blade passage). Finally, the outlet blade metal angle β_{1B} can be found.

Setting the Absolute Flow Angle α_1

Alternatively, the absolute velocity angle α_1 can also be controlled if more control over the outlet velocity triangle is desired. By finding the outlet meridional velocity V'_{1m} (accounting for blade blockage), a fixed outlet width b_1 can be found.

$$b_1 = \frac{\dot{m}}{2\pi \cdot R_1 \cdot \rho_1 \cdot V'_{1m}} \tag{3.48}$$

When implemented within an optimization routine, this option is useful to find an optimal design configuration that varies α_1 to minimize losses over a prescribed range, satisfy stability criteria, or match vaned diffuser inlet angles, for example.

3.6.2 Blade Angle β_{1B}

The outlet blade metal angle β_{1B} must be determined such that the specified head found in Equation 3.42 is achieved with the outlet diameter d_1, the total number of blades N_{bl} (including splitter blades), and the outlet width b_1 determined previously. Outlet blade angles for pump impellers usually lie between 15-45°, but many exceptions exist. Matching the outlet angle is an iterative process since slip and blockage are both a function of the blade angle β_{1B}, influencing the final velocity triangle, and by extension, the final head and stability of the impeller.

Two outlet velocity triangles can be defined: one just upstream of the blade trailing edge (inside the passage) and one directly downstream (outside the passage), as shown in Figure 3.8. The upstream velocity triangle experiences an increased meridional velocity component V_{1m} due to blade blockage compared to the downstream velocity triangle. The downstream velocity triangle experiences slip and a reduced tangential velocity component V_{1t}. The effect of both blade blockage and slip must be accounted for a priori when designing the outlet geometry to ensure that the required head is delivered.

To begin with, the outside (downstream of the passage) outlet velocity triangle without blockage is calculated. This is easily done, as the outlet area is defined, and from the conservation of mass, the outlet meridional velocity V_{1m} can be calculated:

$$V_{1m} = \frac{\dot{m}}{2\pi \cdot r_1 \cdot t_{te} \cdot b_1 \cdot \rho_1} \tag{3.49}$$

Note that since the outlet static density ρ_1 is unknown at this point, an initial guess is warranted– the density from the previous station ρ_0 being a good guess, given that liquids are highly incompressible. The final velocity can be computed by iteration and convergence of the thermodynamic state.

At this point, the outer velocity triangle is defined as V_{1m}, V_{1t}, and U_1 are known (along with their corresponding angles). These vectors are used as an 'inverse design problem', resulting from the blade geometry *after* slip and blockage effects. The next task is to find the upstream (inside the blade passage) velocity triangle, a function of β_{1B}.

Lastly, a first guess is required to begin this procedure: The outlet blade angle is assumed to be aligned with the flow angle $\beta_{1B} = \beta_1$.

Blade Blockage

Similar to the inlet section blade blockage, the outlet area is reduced due to the presence of the blades. This increases the meridional velocity component *inside* of the impeller. The meridional flow velocity diminishes as it exits the blade passage.

As in Equation 3.5.3, the blade thickness definition of Equation 3.35 is considered, accounting for β_{1B}. The inlet blade blockage factor τ_1 and pitch t_1 are found with:

$$\tau_1 = \frac{t_1}{t_1 - \sigma_1} \qquad (3.50) \qquad\qquad t_1 = \frac{\pi \cdot d_1}{N_{bl} + N_{split}} \qquad (3.51)$$

Then, the meridional velocity component V'_{1m} (inside of the blade passage) can be found with:

$$V'_{1m} = \tau_1 \cdot \frac{\dot{m}}{\rho \cdot 2 \cdot \pi \cdot b_1} \qquad (3.52)$$

Blade Slip

Blade slip is a prominent phenomenon in all rotating machinery. The flow is assumed to follow the blade in the derivation of Euler's pump equation. This is not the case in practice since the flow angle is usually smaller than the blade angle.

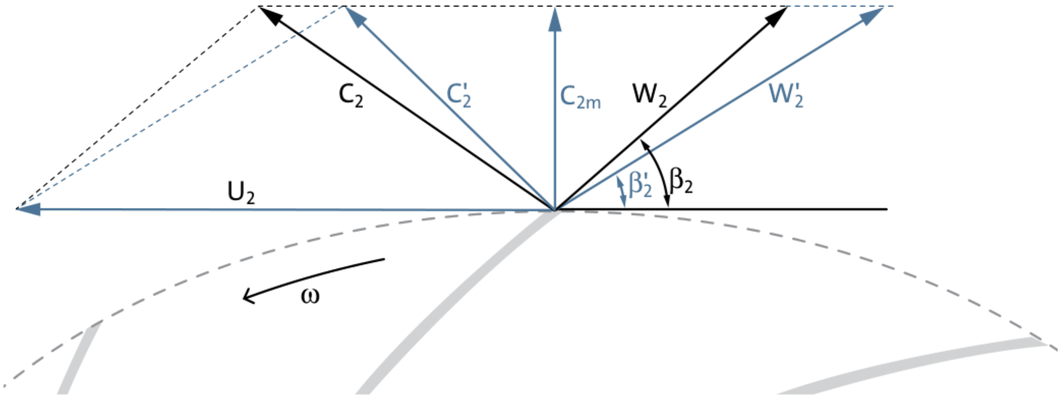

Figure 3.10: Outlet velocity triangle with slip. β_1 and W_1 are the blade metal angles, and β'_1 and W'_1 are the flow angles after slip. [38]

An impeller with an infinite number of infinitely thin blades would result in *blade congruent flow:* flow lines with the same outlet angle as the blades. In practice, the flow does not follow the shape of the blades completely in an impeller with a limited number of blades with finite thickness. The tangential velocity V_{1t} out of the impeller and thus the head is reduced due to this. Various empirical slip factor models have been developed over the years to account for this slip effect. It is important to emphasize that slip is not a loss mechanism but simply an expression of the flow not following the blade. A slip factor is defined as:

$$\sigma = 1 - \frac{V_{1t}}{U_1} \tag{3.53}$$

A value of $\sigma = 1$ would imply *blade congruent* flow, or in other words, the flow angle matches the blade angle $\beta_1 = \beta_{1B}$.

The Relative Eddy Considering a scenario where a frictionless and irrotational fluid flow traverses through an impeller without any rotational motion, it must also exit with zero spin due to the conservation of angular momentum. The impeller rotates with an angular velocity ω, causing the fluid to have a relative angular velocity of $-\omega$ with respect to the impeller, known as the relative eddy: See Figure 3.11. A straightforward explanation for the slip phenomenon in an impeller arises from the concept of a relative eddy.

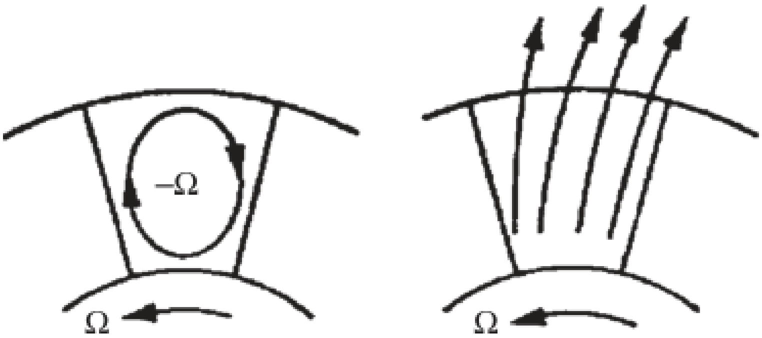

Figure 3.11: Relative eddy without through-flow (left), and relative flow at impeller exit (right)

Upon exiting the impeller, the relative flow can be seen as a main flow with an additional relative eddy. These two motions combine, resulting in the average relative flow leaving the impeller passages at an angle relative to the vanes and in a direction opposite to the blade's movement.

Slip Factor Correlations There have been many attempts to determine correlations for the slip factor. Below is a list of commonly used slip factor σ correlations applicable to centrifugal pumps, implemented in this work:

- **Stanitz** [68]: solved the potential flow field between the blades of eight impellers. He concluded that the computed slip velocity was independent of vane angle and depended only on blade spacing (number of blades).

$$\sigma = 1 - \frac{0.63 \cdot \pi}{N_{bl}} \tag{3.54}$$

- **Wiesner** [75]: reviewed all available methods to date and obtained a simple empirical expression. This expression is still today the most accurate and widely used:

$$\sigma = 1 - \frac{\sqrt{\sin \beta_{1B}}}{N_{bl}^{0.7}} \tag{3.55}$$

- **Aungier/Wiesner** [6]: Aungier noted that Wiesner's model holds up to a limiting radius ratio ϵ_{Lim} and corrects for this:

$$\sigma = 1 - \frac{\sqrt{\sin \beta_{1B}}}{N_{bl}^{0.7}} \tag{3.56}$$

  With the radius ratio $\epsilon = r/r_1 > \epsilon_{Lim}$

$$\sigma_{cor} = \sigma \cdot \left(1 - \left(\frac{\epsilon - \epsilon_{Lim}}{1 - \epsilon_{Lim}}\right)^{\sqrt{(90^\circ - \beta_{1B})/10}}\right) \tag{3.57}$$

  And limiting radius ratio[1]

$$\epsilon_{Lim} = \frac{\sigma - \cos\left(19^\circ + 0.2 \cdot (90^\circ - \beta_{1B})\right)}{1 - \cos\left(19^\circ + 0.2 \cdot (90^\circ - \beta_{1B})\right)} \tag{3.58}$$

- **Wiesner/Gülich** [33]: Gülich modified the Wiesner formula by introducing the correction factor f_1 to adapt the slip factor to a wider database of pumps accounting for blade blockage. He also modified the limiting radius ratio ϵ_{Lim} introduced by Aungier and added a factor k_w to include the influence of the impeller inlet diameter.

$$\sigma = f_1 \cdot \left(1 - \frac{\sqrt{\sin \beta_{1B}}}{N_{bl}^{0.7}}\right) \cdot k_w \tag{3.59}$$

  With the correction factor,

$$f_1 = \begin{cases} 0.98 & \text{for radial impellers} \\ 1.02 + 1.2 \times 10^{-3}(n_q - 50) & \text{for mixed-flow impellers} \end{cases} \tag{3.60}$$

  Inlet diameter influence factor,

$$k_w = \begin{cases} 1 & \text{if } d_{0m}/d_1 \leq \epsilon_{Lim} \\ 1 - \left(\frac{d_{0m}/d_1 - \epsilon_{Lim}}{1 - \epsilon_{Lim}}\right)^3 & \text{otherwise} \end{cases} \tag{3.61}$$

  Mean outlet diameter,

$$d_{0m} = \sqrt{0.5 \cdot \left(d_{0,s}^2 + d_{0,h}^2\right)} \tag{3.62}$$

---

[1] 90° is added to the blade angle since this work uses the alternative definition of β, as discussed in chapter 3.

And limiting radius ratio

$$\epsilon_{Lim} = \exp\left(-\frac{8.16 \cdot \sin(\beta_{1B})}{N_{bl}}\right) \tag{3.63}$$

- **Backström** [8]: Von Backström developed an empirical equation for estimating the outflow coefficient assuming one relative eddy in the rotor.

$$\sigma = 1 - \frac{1}{F_0 \cdot \mathrm{sol} \cdot \sqrt{\sin\beta_{1B}}} \tag{3.64}$$

with solidity `sol` as:

$$\mathrm{sol} = \frac{1 - \epsilon \cdot N_{bl}}{2\pi \cdot \sin\beta_{1B}} \tag{3.65}$$

with the limiting radius ratio $\epsilon_{Lim} = 0.5$, radius ratio $\epsilon = \max(r_0/r_1, \epsilon_{Lim})$, and constant $F_0 = 5.0$

- **Qiu** [62]: Qiu presented a *unified* correlation for the slip factor applicable to axial, radial, and mixed flow impellers. The model is composed of three components:

$$\sigma = 1 - \Delta\sigma_{\mathrm{radial}} - \Delta\sigma_{\mathrm{turn}} - \Delta\sigma_{\mathrm{passage}} \tag{3.66}$$

with the decrement in slip due to the effect of radial rotation, with the blade lean angle γ and shape factor F,

$$\Delta\sigma_{\mathrm{radial}} = \frac{F \cdot \pi \cdot \cos\beta_{1B} \cdot \sin\gamma_1}{N_{bl}} \tag{3.67}$$

the decrement due to blade turning,

$$\Delta\sigma_{\mathrm{turn}} = \frac{F \cdot s_1 \cdot \phi_1}{4\cos\beta_{1B}}\left(\frac{d\beta}{dm}\right)_1 \tag{3.68}$$

the decrement due to any variations of passage width and density

$$\Delta\sigma_{\mathrm{passage}} = -\frac{F \cdot \phi_1 \cdot s_1 \cdot \sin\beta_{1B}}{4\rho_1 \cdot H_1}\left(\frac{d(\rho b)}{dm}\right)_1 \tag{3.69}$$

The author noted that Equation 3.69 is negligible compared to the other terms and can be neglected. Furthermore, there are mixed results of this model in the literature. Zhang [80] and Wiesner [75] noted in their slip factor reviews that Qiu's model may be unsuitable for 1D preliminary design due to the unknown blade turning term σ_{turn}. However, a recent study [22] has found that this model is the most accurate at predicting slip in CFD for high-speed centrifugal compressors.

These slip factor correlations are well-validated. In a centrifugal impeller slip factor meta-review [74], the *Wiesner's* original slip factor was shown to provide the best fit with experimental data across impellers of many specific speeds despite its simplicity. New data-driven models have been developed recently, such as Zakeralhoseini's data-driven slip model for small-scale ORC turbopumps with leakage flow [77]. However, this was not implemented in this work due to inaccurate results after testing and the lack of validation surrounding this method.

The next step to determine the outlet blade angle β_{1B} is to obtain the *internal* outlet tangential flow velocity V'_{1t} by making use of a suitable slip model. The blade angle is adjusted (increased) to account for slip and result in an *external* velocity triangle with the desired head such that $\beta_{1B} \geq \beta_1$. This is done with Equation 3.70.

$$V'_{1t} = V_{1t} + (1 - \sigma) \cdot U_1 \tag{3.70}$$

With Equation 3.52, the full velocity triangle is defined, and β_{1B} can be found.

$$\beta_{1B} = \arctan \frac{V'_{1t} - U_1}{V'_{1m}} \tag{3.71}$$

However, since both Equation 3.52 and Equation 3.70 are a function of β_{1B}, the velocity triangle must be iterated to converge on to the desired outlet tangential velocity.

Outlet Angle Limit While forward-swept blades provide increased outlet pressure in turbomachines, they increase blade loading and lead to flow instabilities [33]. Avoiding forward-swept blades and limiting the blade angles to 90° (radial blades) is common practice.

In this work, the user can limit the blade angle (90° as default). Given that $\beta_{1B} \geq \beta_1$, the blade angle could exceed these bounds when accounting for slip. To avoid this, the blade angle is limited to the imposed bound, and the resulting velocity and head will be decreased. In this scenario the user is warned and advised to edit other design variables such as the outlet width b_1 or the outlet diameter d_1 to achieve the desired head.

Finally, remember that only the *external* outlet velocity triangle affects the final pump head. The *internal* velocity triangles are used to obtain the required blade and impeller geometry to provide the required head.

3.7 Vaneless Diffuser

As the flow exits the rotating impeller outlet, it carries a lot of kinetic energy. In most applications, this kinetic energy is converted into pressure energy, which is most useful in this form. Additionally, friction losses are a function of the square of the velocity V^2, so by decreasing the flow velocity the total pressure losses are also decreased during transportation of the working fluid.

$$P_t = P + \rho \cdot \frac{V^2}{2} \tag{3.72}$$

As the amount required to be converted from kinetic to pressure energy is application-dependent, the diffuser section has to be flexible enough to accommodate various design conditions. This can be done by sizing the diffuser outlet diameter d_{diff} (the inlet is fixed on the impeller outlet diameter d_1). See Figure 3.12 for a clearer picture.

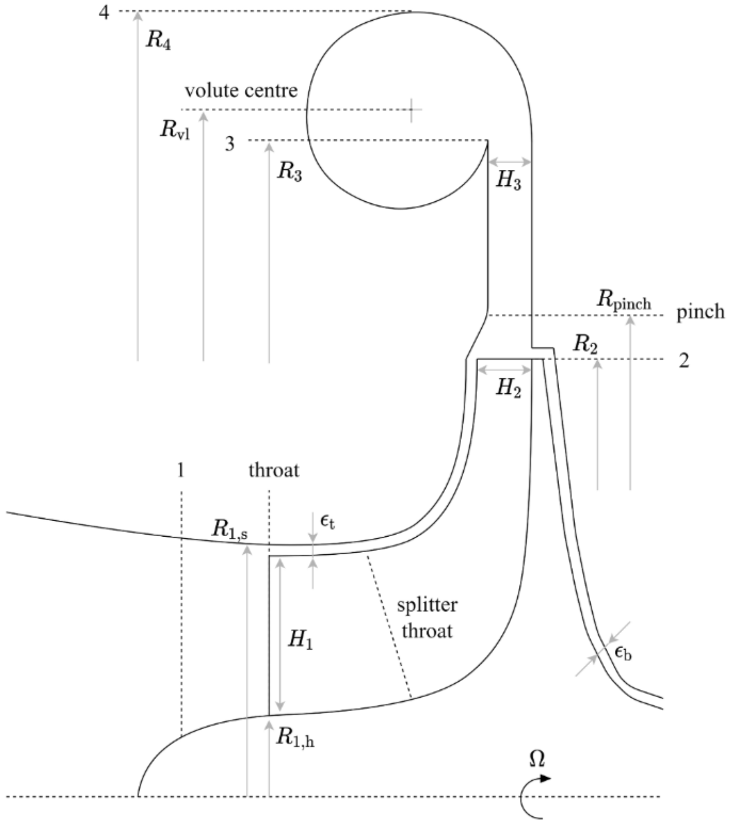

Figure 3.12: Meridional section view of a centrifugal pump stage with a pinched vaneless diffuser and an overhung volute [28]

Since the impeller outlet velocity is known, the diffuser outlet flow quantities can be found for a given geometry using the conservation of mass. The outlet density ρ_2 can be assumed to be equal to the inlet density ρ_1 or computed given the outlet thermodynamic state. To conveniently express the diffuser geometry, each dimension is 'normalized' by the impeller outlet radius and blade height, such that the radius is taken as R_2/R_1. Note that the impeller exit area does *not* account for the influence of blade blockage.

$$V_2 = \frac{\rho_1 V_1 A_1}{\rho_2 A_2} = \frac{\rho_1 V_1}{\rho_2} \cdot \frac{b_1}{b_2} \cdot \left(\frac{R_1}{R_2}\right)^2 \tag{3.73}$$

As the outlet radius R_2 increases, the velocity V_2 decreases, and per the energy conservation with Equation 2.5, the static pressure P_2 increases.

3.8 Volute

The volute is an essential component in centrifugal turbomachines. It collects the radially directed flow and guides it smoothly toward the outlet to minimize losses. It is often designed as a spiral, which increases the area circumferentially up to the outlet discharge. Some volutes may have a square or oval cross-section.

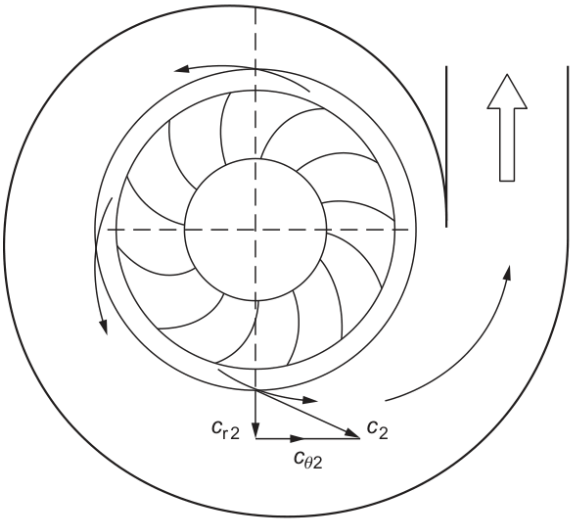

Figure 3.13: Top view of pump volute [25]

While the volute is spiral-shaped, it acts just like a linear diffuser. Again, the difference in the area between the inlet and outlet causes a deceleration of the flow velocity. Taking a closer look at the spiral shape, by considering a stationary, fixed point around the impeller (or diffuser) circumference, the flow exits with both a tangential and meridional component. To smoothly guide the flow without large velocity gradients and to maintain a constant mass flow, the radius is progressively increased around the circumference until the 'tongue', where the outlet pipe is connected. The area ratio from the inlet to outlet R_2/R_3 dictates the flow deceleration. Again, the outlet density ρ_3 can be assumed equal to the inlet density ρ_2, but the outlet area A_3 will depend on the cross-section of the volute, commonly circular or square.

$$V_3 = \frac{\rho_2 \cdot V_2 \cdot \pi R_2 \cdot b_2}{\rho_3 A_3} \tag{3.74}$$

Finally, the exit pressure can be computed with Equation 2.5.

3.9 Exit Cone

The final section to be considered is the exit cone, which is essentially another kind of diffuser. As the name suggests, the shape is conical, with a circular or square cross-section. The length-to-diameter ratio L/D determines the cone geometry, and the cone semi-angle θ.

This choice of geometry parametrization is taken since it has been found that cone semi-angles above 10° (rapid area increase) lead to separation and mixing losses, and below 2.5° (slow area increase) incur excessive friction losses [67].

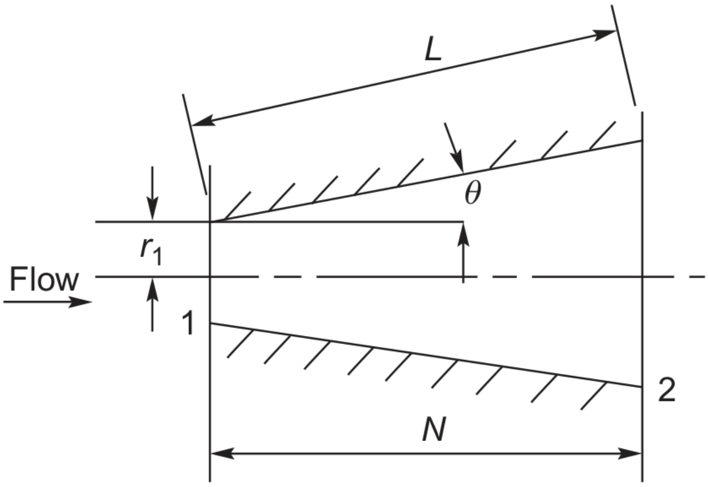

Figure 3.14: Exit cone geometry [25].

3.10 Loss Modeling

Every design step taken so far has been assuming isentropic conditions. To account for the various losses incurred by the flow, researchers have developed various *loss models* over time. Researchers and engineers have noticed that while the flow within impellers exhibits a complex behavior, some common flow structures can be found within the chaos. Models have been built systematically by isolating these phenomena and assessing their impact on hydraulic performance. Some losses are simple enough to be described with basic fluid dynamics principles, and some are more complex, requiring experimental campaigns or data-driven methods to characterize them. This project aims to use models based on first principles and only use applicable empirical models where necessary.

As shown in section 3.6, Euler's pump equation provides a simple, loss-free description of the impeller performance. In reality, because of mechanical and hydraulic losses inside the impeller and pump casing, the actual pump head is lower than predicted by the Euler pump equation, and the power consumption is higher than theoretically predicted, see Figure 3.16. This section describes the various types of losses and introduces models for calculating their magnitude, developed by many researchers over time. Some of these models are based on first principles, while others rely on experimental campaigns or data-driven methods. The project focuses on using models based on first principles, incorporating empirical models only when necessary.

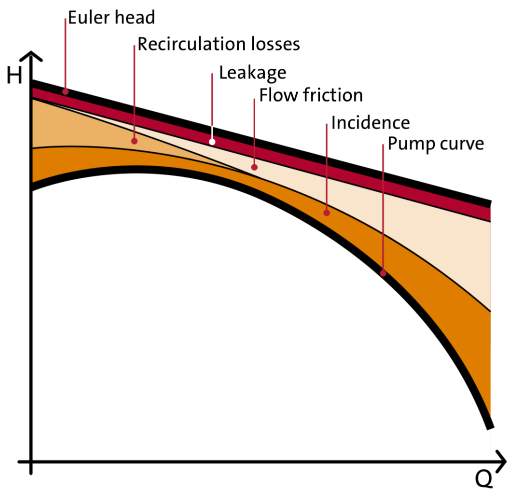

Figure 3.15: Head losses on the head-capacity curve. [38]

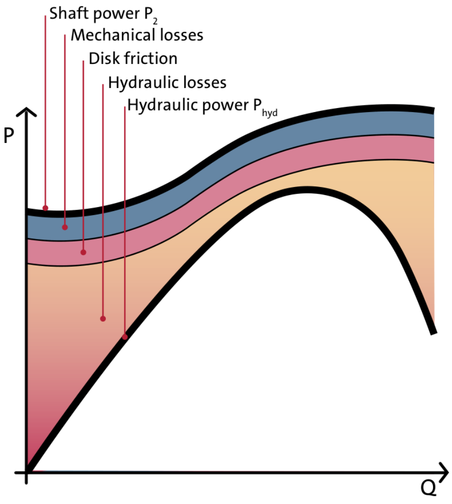

Figure 3.16: Power increase due to losses on the head-capacity curve. [38]

Losses are accounted for by altering the total enthalpy change Δh_t through a component. This is done by distinguishing two types of losses:

- **Internal Losses** $\Delta h_{t,int}$: These losses occur *inside* the primary flow path of a component. These increase the static temperature T and thus the entropy s of the fluid. Internal losses reduce the amount of mechanical energy added to the flow.
- **External Losses** $\Delta h_{t,ext}$: These losses occur *outside* the primary flow path of a component. These are considered as a h_t rise. External losses do not affect the amount of energy added to the flow, but they increase the required shaft work to deliver a certain amount of mechanical work to the flow.

Given these two loss categories, two efficiency measures can be defined to assess the performance of a pump. Firstly, the total-to-total efficiency η_{tt}:

$$\eta_{tt} = \frac{w_{eul} - \Delta h_{t,int}}{w_{eul} + \Delta h_{t,ext}} \tag{3.75}$$

With w_{eul} as the Euler work and $\Delta h_{t,int}$, and $\Delta h_{t,int}$ as the sum of internal and external losses, respectively. Furthermore, to assess the isolated hydraulic efficiency of a component, the internal efficiency $\eta_{tt,int}$ can be defined by neglecting the external losses:

$$\eta_{tt,int} = \frac{w_{eul} - \Delta h_{t,int}}{w_{eul}} \tag{3.76}$$

Over the last decades, many researchers have developed sets of loss models suitable to study the performance of turbomachines. Loss models are either developed from first principles, experimental data, or a data-driven approach. This variety in model design, coupled with the various assumptions introduced into each model, adds uncertainty and limitations that should be considered by the design engineer making use of them. Various studies have focused on providing optimal sets of loss models for various turbomachines ([56], [55], [31], [50], [2], [77], [79]). A thorough review of these studies has been done to build the most up-to-date and comprehensive list of loss models, giving various options to the design engineer, presented in Table 4.3.

3.10.1 Internal Losses

The internal loss models commonly applied throughout literature for centrifugal turbopump impellers are introduced below.

- **Incidence:** Incidence loss occurs when there is a difference between the flow angle β_0 and blade angle β_{0B} at the impeller leading edge. This is typically the case at off-design conditions or when inlet prerotation exists. A recirculation zone occurs on one side of the blade when the incidence is nonzero, causing recirculation and mixing. The designer should match flow and blade angles to minimize incidence losses. Rounding the blade's leading edge can help reduce the incidence loss.
  - Conrad [17] first introduced the semi-empirical incidence loss correlation as proportional to the tangential relative velocity squared at the impeller inlet, with an incidence coefficient f_{inc} set between 0.5-0.7. Galvas [27] later added that the loss is related to the difference between the actual flow incidence angle i and the optimum flow angle i_{opt} at the on-design point (typically zero).

$$\Delta h_{t,inc} = f_{inc} \cdot \frac{\Delta W_{0t}^2}{2} = \frac{f_{inc}}{2} \cdot \left(W_0 \cdot \sin|i - i_{opt}|\right)^2 \tag{3.77}$$

  - Aungier [6] proposed an incidence loss correlation assuming axial inflow. The loss is evaluated by the difference between actual and ideal relative velocity:

$$\Delta h_{t,inc} = 0.4 \cdot \left(W_0 - \frac{V_{0m}}{\sin \beta_{0B}}\right)^2 \tag{3.78}$$

- **Skin Friction:** Friction occurs when the fluid is in contact with the rotating impeller and the stationary pump casing surfaces. The friction causes a pressure loss, which reduces the head. The magnitude of the friction loss depends on the roughness of the surface and the fluid velocity relative to the surface.
  - Jansen [39] introduced correlation based on the assumption of a pipe flow, which does not consider the non-uniform velocity distribution in the impeller channel due to the boundary layer. The impeller skin friction coefficient C_f estimate is discussed in Appendix A (Equation A.5).

$$\Delta h_{t,sf} = 2 \cdot C_f \cdot \frac{L_{\text{hyd}}}{D_{\text{hyd}}} \cdot \overline{W^2} \tag{3.79}$$

    With the weighted average relative velocity proposed by Aungier [6],

$$\overline{W} = \frac{V_{0,s} + V_1 + W_{0,s} + 2 \cdot W_{0,h} + 3 \cdot W_1}{8} \tag{3.80}$$

    Impeller hydraulic flow length L_{hyd},

$$L_{\text{hyd}} = \frac{\pi}{8} \cdot \left(d_1 - \frac{d_{0,s} + d_{0,h}}{2} - b_1 + 2 \cdot L_z \right) \cdot \left(\frac{4}{\cos\beta_{0,s} + \cos\beta_{0,h} + 2\cos\beta_1} \right) \tag{3.81}$$

The impeller's axial length L_z can be prescribed as a function of the outer diameter d_1 if the ratio $\frac{L_z}{d_1}$ is known:

$$L_z = d_1 \cdot \frac{L_z}{d_1} \tag{3.82}$$

Or it can be estimated with an empirical correlation proposed by Aungier [6]:

$$L_z = d_1 \cdot \left(0.014 + 0.023 \cdot \frac{d_1}{d_{0,h}} + 1.58 \cdot \phi_{t1} \right) \tag{3.83}$$

Finally, the impeller's average hydraulic diameter D_{hyd}:

$$D_{\text{hyd}} = d_1 \cdot \left(\frac{\cos\beta_1}{\left[\frac{N_{bl}}{\pi} + \frac{d_1 \cdot \cos\beta_1}{H_1} \right]} + \frac{0.5 \cdot \left(\frac{d_{0,s}}{d_1} + \frac{d_{0,h}}{d_1} \right) \cdot \left(\frac{\cos\beta_{0,s} + \cos\beta_{0,h}}{2} \right)}{\frac{N_{bl}}{\pi} + \left(\frac{d_{0,s} + d_{0,h}}{d_{0,s} - d_{0,h}} \right) \cdot \left(\frac{\cos\beta_{0,s} + \cos\beta_{0,h}}{2} \right)} \right) \tag{3.84}$$

– Gülich also proposed a correlation by considering the influence of different roughnesses on the casing walls and impeller shrouds [33]:

$$\Delta h_{t,sf} = 2 \cdot C_d \cdot \frac{L_{\text{hyd}}}{D_{\text{hyd}}} \cdot \overline{W^2} \tag{3.85}$$

$$C_d = \left(C_f + 0.0015 \right) \left(1.1 + 4 \cdot \frac{H_1}{R_1} \right) \tag{3.86}$$

$$C_f = \frac{0.136}{\left(-\log\left(0.2 \frac{e}{L_{\text{hyd}}} + \frac{12.5}{Re} \right) \right)^{2.15}} \tag{3.87}$$

- **Tip Clearance:** With unshrouded impellers, clearances exist between the blades and the casing. The adverse pressure gradient between the two surfaces of the impeller blade induces a loss and a leakage flow through the clearance gap. This efficiency drop and pressure loss are almost proportional to the relative tip clearance.
  - Jansen [39] found that the fluid experiences a rapid contraction and expansion process through the tip clearance, considering the ratio of the inlet to outlet density. Note that since this model was developed for a mean-line code, the flow properties should also be mean-line.

$$\Delta h_{t,cl} = 0.6 \cdot \frac{\epsilon_t \cdot |V_{t,1}|}{b_1 + \frac{\epsilon_t}{2}} \sqrt{\frac{4\pi \cdot |V_{t,1}| \cdot V_{m,0} \cdot k_{cl}}{\left(b_1 + \frac{\epsilon_t}{2} \right) \cdot N_{bl}}} \tag{3.88}$$

$$k_{cl} = \frac{r_{0,s}^2 - r_{0,h}^2}{(r_1 - r_{0,s})\left(1 + \frac{\rho_1}{\rho_0}\right)} \tag{3.89}$$

- Gülich proposed an empirical correlation for the tip clearance losses. [33]

$$\Delta h_{t,cl} = U_1^2 \cdot \psi_{is} \cdot (1 - R) \tag{3.90}$$

$$R = \frac{2.5 \cdot \frac{\epsilon_t}{d_2}}{\sqrt{\frac{b_1}{d_2} \cdot \left(1 - \frac{d_1}{d_2}\right) \cdot N_{bl} \cdot \left(\frac{e}{t_2}\right)^{0.2}} \cdot n_q^{0.1} \cdot \sin\beta_2{}^{1.2} \cdot \sin\beta_1{}^{0.4}} \tag{3.91}$$

- Gülich-mod: Zakeralhoseini modified Gülich's model to include a wider array of specific-speed pumps and conditions [77].

$$\Delta h_{t,cl} = U_1^2 \cdot \psi_{is} \cdot (1 - R) \tag{3.92}$$

$$R = \frac{0.465 \cdot n_q^{0.051} \cdot \left(\frac{\epsilon_t}{b_1}\right)^{0.483} \cdot \left(\frac{d_1}{d_2}\right)^{0.383}}{\sin\beta_1{}^{0.142} \cdot \sin\beta_2{}^{0.834} \cdot N_{bl}^{0.053}} \tag{3.93}$$

- Van Den Braembussche also proposed an experimental model from his own research [71].

$$\Delta h_{t,cl} = 2.43 \cdot |\epsilon_t| \cdot H_1 \cdot \left(1 - \left(\frac{R_{0,h}}{R_1}\right)^2\right) \cdot U_1^2 \tag{3.94}$$

- **Separation:** The separation loss is caused by the reverse pressure gradient along the flow direction and corresponding boundary layer loss. Well-designed impeller blades should not suffer from flow separation losses at their design operating conditions. However, at off-design conditions, the diffusion levels can become very high, and the flow can separate, leading to excessive losses and possibly stall.
    - Oh determined a critical ratio after which the flow separates from the impeller blades [56].

$$\Delta h_{t,sep} = \begin{cases} 0.61 \cdot \left(\frac{W_0}{W_1} - 1.4\right)^2 \cdot W_1^2 & \text{for } \frac{W_0}{W_1} > 1.4 \\ 0 & \text{for } \frac{W_0}{W_1} < 1.4 \end{cases} \tag{3.95}$$

- **Blade Loading:** The work transfer by the blades is inherently linked to non-uniform flow over the pitch of the blades. However, as it increases, the non-uniformity of the flow causes losses induced by the pressure difference from the pressure side to the suction side, affecting the secondary flow and boundary layer separation inside the impeller passage.

- Coppage [18] thought of flow diffusion as the main cause of boundary layer growth. He proposed the following equation to calculate the blade loading loss:

  $$\Delta h_{t,bl} = 0.05 \cdot (DF \cdot U_1)^2 \tag{3.96}$$

  The diffusion factor DF is given by:

  $$DF = 1 - \frac{W_1}{W_0} + 0.75 \cdot \frac{|\Delta h_{tt}|}{U_1^2} \cdot \frac{W_1}{W_{0,s}} \cdot \left(\frac{N_{bl}}{\pi\,(1 - d_{0,s}/d_1)} + 2 \cdot \frac{d_{0,s}}{d_1} \right)^{-1} \tag{3.97}$$

  With $|\Delta h_{tt}|$ as the impeller's Euler work.

- Aungier [6] proposed that the blade-to-blade pressure gradient produces a strong secondary flow. He presented the loss correlation as a function of the relative velocity difference between the suction and pressure sides:

  $$\Delta h_{t,bl} = \frac{\Delta W}{48} \tag{3.98}$$

  $$\Delta W = \frac{2\pi \cdot d_1 \cdot V_{1t}}{N_{bl} \cdot L_{hyd}} \tag{3.99}$$

- **Mixing:** The mixing loss arises from mixing the suction surface and pressure surface boundary layers with the flow region just behind the trailing edge. The sudden expansion at the impeller's trailing edge creates a jet wake region at the impeller outlet.

  - Johnston and Dean [43] theorized that a jet flow mixes with a wake flow at the impeller outlet as a rapid expansion process. They assumed that the static pressure in the jet and wake are the same at the impeller outlet and that there is no relative flow in the wake. Where ϵ_w represents the wake width, ranging from 0.366 to 0.482, and B is an expansion coefficient, relating the outlet area of the impeller to the inlet of the diffuser (commonly set to 1).

    $$\Delta h_{t,mix} = \frac{1}{1 + \tan^2(\alpha_1)} \cdot \left(\frac{1 - \epsilon_w - B}{1 - \epsilon_w} \right)^2 \cdot \frac{V_1^2}{2} \tag{3.100}$$

  - Aungier [6] realized that once flow separation occurs, there is no further diffusion in the impeller channel, and the relative velocity difference between the separation point and the impeller outlet can be used to evaluate the mixing loss.

    $$\Delta h_{t,mix} = 0.5 \cdot \left(W_{sep} - W_{out} \right)^2 \tag{3.101}$$

    With

    $$W_{out} = \sqrt{\left(\frac{V_1 \cdot A_1}{\pi \cdot d_1 \cdot b_1} \right)^2 + W_{0t}^2} \tag{3.102}$$

The wake flow mixes with the jet flow at a relative separation velocity W_{sep}. If the equivalent diffusion factor $D_{eq} > 2$, separation is assumed to occur inside the flow passage.

$$W_{sep} = \begin{cases} W_1 & D_{eq} \leq 2 \\ \frac{W_1 D_{eq}}{2} & D_{eq} > 2 \end{cases} \tag{3.103}$$

With

$$W_{max} = \frac{W_0 + W_1 + \Delta W}{2} \tag{3.104}$$

$$D_{eq} = \frac{W_{max}}{W_1} \tag{3.105}$$

The relative velocity difference ΔW between the pressure and suction sides is given as:

$$\Delta W = \frac{2\pi \cdot d_1 \cdot V_{1t}}{N_{bl} \cdot L_{hyd}} \tag{3.106}$$

3.10.2 External Losses

List of available external loss models applicable to centrifugal turbopumps. Again, these models are only applicable to the impeller.

- **Leakage:** Leakage loss occurs because of flow circulation through gaps between the rotating and fixed parts of the pump (impeller and casing). Leakage loss results in a loss in efficiency since the flow in the impeller is increased compared to the flow through the entire pump. To minimize the leakage flow, the gaps should be made as small as possible. When the pressure difference across the gap is large, the gaps must be small.
    - Aungier [6] proposed the following correlation:

$$\Delta h_{t,lk} = \frac{\dot{m}_{lk} \cdot U_{lk} \cdot U_1}{2\dot{m}} \tag{3.107}$$

$$U_{lk} = 0.816\sqrt{\frac{2 \cdot \Delta P_{lk}}{\rho_1}} \tag{3.108}$$

$$\dot{m}_{lk} = \rho_1 \cdot U_{lk} \cdot N_{bl} \cdot \epsilon_{cl} \cdot L_{hyd} \tag{3.109}$$

$$\Delta P_{lk} = \frac{\dot{m} \cdot (R_1 V_{1t} - R_{0,s} V_{0t,s})}{N_{bl} \cdot L_{\text{hyd}} \cdot \left(\frac{R_{0,s}+R_0}{2}\right) \cdot \left(\frac{b_0+b_1}{2}\right)} \tag{3.110}$$

    - Jansen [39] developed the following model:

$$\Delta h_{lk} = 0.6 \cdot \frac{\epsilon_{cl}}{b_1} \cdot V_1 \sqrt{\frac{4\pi}{b_1 \cdot N_{bl}} \cdot \frac{r_{0,t} - r_{0,h}}{r_1 - r_{0,t}} \cdot \left(1 + \frac{\rho_1}{\rho_0}\right)^{-1} \cdot V_{1t} \cdot V_0} \tag{3.111}$$

- **Recirculation:** Under partial flow rates, part of the fluid flows back to the impeller due to the relatively large adverse pressure gradient at the impeller outlet, consuming additional shaft work from the impeller and reducing the effective cross-section area which the flow experiences. The result is a considerable mixing loss. Recirculation is a complex phenomenon that strongly depends on the geometry and operating point. In a high-pressure and highly-loaded centrifugal compressor, high recirculation loss occurs due to the large exit absolute flow angle and high diffusion factor[2].
  - Oh [56] examined the exit absolute flow angle and applied a hyperbolic function. The loss correlation was validated with experimental results using low-pressure ratio centrifugal compressors. It is not recommended for highly loaded centrifugal pumps:

$$\Delta h_{t,rc} = 8 \cdot 10^{-5} \cdot \sinh(3.5 \cdot \alpha_1^3) \cdot (DF \cdot U_1)^2 \tag{3.112}$$

  - Coppage established the following correlation [18]

$$\Delta h_{t,rc} = 0.02 \cdot \tan \alpha_1 \cdot (DF \cdot U_1)^2 \tag{3.113}$$

- **Disk Friction:** Disk friction occurs on the shroud and hub of the impeller because it rotates in a fluid-filled pump casing. The fluid in this cavity between the impeller and pump casing starts to rotate, creating primary and secondary vortices. The geometry of the cavity and the surface roughness play an important role.
  - Daily and Nece [21] conducted an experimental study where a smooth plane disk rotated within a right-cylindrical chamber. They analyzed the experimental phenomena to establish the following loss correlation

$$\Delta h_{t,df} = K_f \cdot \frac{\rho_0 + \rho_1}{2} \cdot \frac{R_1^2 \cdot U_1^3}{4\dot{m}} \tag{3.114}$$

$$K_f = \begin{cases} \left(\frac{\epsilon_b}{H_1}\right)^{0.1} \cdot \frac{3.7}{Re_1^{0.5}} & \text{for } Re_1 < 3 \times 10^5 \\ \left(\frac{\epsilon_b}{H_1}\right)^{0.1} \cdot \frac{0.102}{Re_1^{0.2}} & \text{for } Re_1 \geq 3 \times 10^5 \end{cases} \tag{3.115}$$

3.10.3 Vaneless Diffuser Losses

The flow continually diffuses along the radius of the vaneless diffuser, resulting in an enthalpy loss due to friction and diffusion. Stanitz [68] developed a radially discretized flow solution from the conservation of mass, momentum, and energy that can be solved through Runge-Kutta integration.

---

[2] The diffusion factor DF is shown in Equation 3.97

$$V_m \frac{dV_m}{dR} - \frac{V_t^2}{R} + C_f \frac{V^2 \cos\alpha}{H \sin\chi} + \frac{1}{\rho} \frac{dP}{dR} = 0 \tag{3.116}$$

$$V_m \frac{dV_t}{dR} + \frac{V_m V_t}{R} + C_f \frac{V^2 \cos\alpha}{H \sin\chi} = 0 \tag{3.117}$$

$$\frac{1}{\rho} \frac{d\rho}{dR} + \frac{1}{V_m} \frac{dV_m}{dR} + \frac{1}{H} \frac{dH}{dR} + \frac{1}{R} = 0 \tag{3.118}$$

$$V_m \frac{dV_m}{dR} + V_m \frac{dV_m}{dR} + V_t \frac{dV_t}{dR} = 0 \tag{3.119}$$

The skin friction coefficient C_f is discussed and shown in Appendix A (Equation A.7).

3.10.4 Volute Losses

Japikse [41] reported a loss modeling technique for an overhung volute based on the geometrical area ratio $AR = A_3/A_2$. The loss in the volute is expressed as a total pressure loss $\Delta P_{t,vol}$:

$$\Delta P_{t,vol} = (K_m + K_\theta) \cdot (P_{t,2} - P_2) \tag{3.120}$$

With the flow swirl $\lambda = V_{2,t}/V_{2,m}$ entering the volute, tangential K_θ and meridional K_m loss factors are computed. The tangential flow component is modeled assuming that losses only occur if the tangential flow decelerates (diffusion):

$$K_\theta = \begin{cases} F_2 \cdot \left(\frac{R_3}{R_{vol}}\right)^2 \cdot \frac{(\lambda - 1/AR)^2}{1+\lambda^2} & \text{if } AR \cdot \lambda > 1 \textit{ (Diffusion)} \\ 0 & \text{if } AR \cdot \lambda \leq 1 \textit{ (Acceleration)} \end{cases} \tag{3.121}$$

Furthermore, it is assumed that the meridional component of kinetic energy entering the volute is completely lost.

$$K_m = \frac{F_1}{1 + \lambda^2} \tag{3.122}$$

Empirical correction factors F_1 and F_2 are included, with values of [0.6 - 1.0] and [0.5 - 1.0], respectively.

3.10.5 Exit Cone Losses

The exit cone total pressure loss $\Delta P_{t,cn}$ is estimated using well-known duct flow correlations [1].

$$\Delta P_{t,cn} = \rho_3 \cdot \frac{V_3^2}{2} \cdot \frac{8 \cdot C_f \cdot L_{cn}}{\rho_3 + \rho_4} \tag{3.123}$$

The friction factor C_f can be found with Equation A.5 in Appendix A.

3.11 NPSH$_\mathrm{R}$ Modeling

Assessing if–and when–a pump is experiencing cavitation is a crucial component in the design methodology. The inception of cavitation is very simply given when the static pressure falls below the vapor pressure $P < P_v$. As explained in subsection 2.5.1, the *available* net positive suction head NPSH$_A$ measures how much pressure 'margin' is available before cavitation inception occurs.

$$\mathrm{NPSH}_A = \frac{P_t - P_v}{\rho g} \tag{3.124}$$

However, in practice, cavitation inception NPSH$_i$ is not commonly used, as it is hard to measure, and it does not affect performance significantly. The most used NPSH$_R$ criterion is NPSH$_{3\%}$, which is usually found via experimental campaigns. Transient multiphase CFD simulations are still prohibitively expensive during the design exploration phase; therefore, this work uses several empirical models and conservatively makes use of the maximum value provided from the following set:

Source	Equation
Pfleiderer [60]	$\mathrm{NPSH}_R = \lambda_c \frac{V_{m,0}^2}{2g} + \lambda_w \frac{W_0^2}{2g}$
Gülich [33]	$\mathrm{NPSH}_R = \left(\frac{n\sqrt{Q}}{n_{ss}}\right)^{4/3}$
Stepanoff [69]	$\mathrm{NPSH}_R = 1.22 \cdot 10^{-3} \cdot n_q^{4/3} \cdot H$
Petermann [60]	$\mathrm{NPSH}_R = \frac{1}{g} \cdot \left(\frac{n\sqrt{Q}}{S_q}\right)^{4/3}$
	with suction number $S_q = (0.2)\,0.4 \ldots 0.6\,(2.0)$
Europump [61]	$\mathrm{NPSH}_R = (0.3 \ldots 0.5) \cdot n\sqrt{Q}$

Table 3.2: Summary of NPSH$_\mathrm{R}$ Equations from Various Sources

These simple models give a rule-of-thumb estimate to avoid cavitation regimes during design. They are calculated at each design point, and the maximum NPSH$_R$ value is chosen as a conservative approach. This is compared against the computed NPSH$_A$ such that NPSH$_A$ > NPSH$_R$ over the entire operating range.

4

Software Tool

This chapter discusses the details of the reduced-order model program structure, methodology implementation, and other various features. This work aims to consolidate these methodologies and provide options for the end-user to fulfill their design goal.

4.1 Reduced Order Model

This pump design program has been implemented into *TurboSim*, a general turbomachinery design framework developed at the Aerospace Power and Propulsion department of TU Delft. Extensive work has already been done to develop design models for axial turbines, radial inflow turbines, and centrifugal compressors. This in-house tool allows design exploration in a wide region for a relatively low computational cost.

The program is written in `Python` and uses an object-oriented approach. It computes the fluid-dynamic performance of a pump stage based on various design variables and the *lumped parameters* system modeling method while including the spanwise distribution of flow properties. Furthermore, it uses loss models based on first principles and validated correlations to deal with arbitrary flow regimes and working fluids.

4.1.1 Lumped Parameter Method

A lumped parameter model considers discrete flow properties at a component inlet and outlet; it does not consider radial or axial gradients in the fluid properties. A fully distributed model (such as CFD) would consider the variation of fluid properties and interaction with its neighboring elements in all three dimensions and over time.

The impeller has two stations: at the inlet and the outlet. Quantities like *Pressure*, *Temperature*, and *Density* are computed at these locations. The first station lies upstream of the impeller inlet, and the second station lies immediately downstream of the impeller outlet. This approach is efficient at obtaining first-order estimates of the performance of a machine.

The remaining components downstream of the impeller are symmetrical along their span (radial diffuser, volute, and exit cone), so instead, they are discretized into multiple elements streamwise.

4.1.2 Thermophysical Modeling

A thermophysical property library is used to update the thermodynamic state of the working fluid at each station. Two highly accurate and efficient options, CoolProp and REFPROP, are available.

- **CoolProp** [10] is an actively maintained, open-source, cross-platform thermophysical property library written in C++. It provides accurate and consistent thermodynamic and transport properties for various fluids. The library is widely used in engineering and scientific applications, particularly thermodynamics, heat transfer, and fluid mechanics.
- **REFPROP** [46] (Reference Fluid Thermodynamic and Transport Properties Database) is a highly accurate, commercial software developed by the National Institute of Standards and Technology (NIST). It is widely regarded for its precise property calculations, especially in the refrigeration and air conditioning industries. REFPROP is a commercial package developed by NIST and is not freely available.

In this implementation, CoolProp is used as a high-level wrapper. If desired, the backend can be changed from the recommended HEOS (Helmholtz Equation of State) to REFPROP (if locally available). The HEOS model [47] can represent pure fluid and mixture states with uncertainties of 0.1% in density and 1% in heat capacities with relatively simple functions given experimental data of comparable uncertainties.

4.2 Program Structure

The main goal of the program is to provide a detailed performance analysis of a specific machine based on a set of inputs. It can be used to evaluate the performance of an existing pump design or to create a new and optimized design to meet specific performance criteria.

Below is a meridional section of the pump, with stations: 0 (impeller inlet), 1 (impeller outlet / diffuser Inlet), 2 (diffuser outlet/volute inlet), and 3 (volute outlet / exit cone inlet).

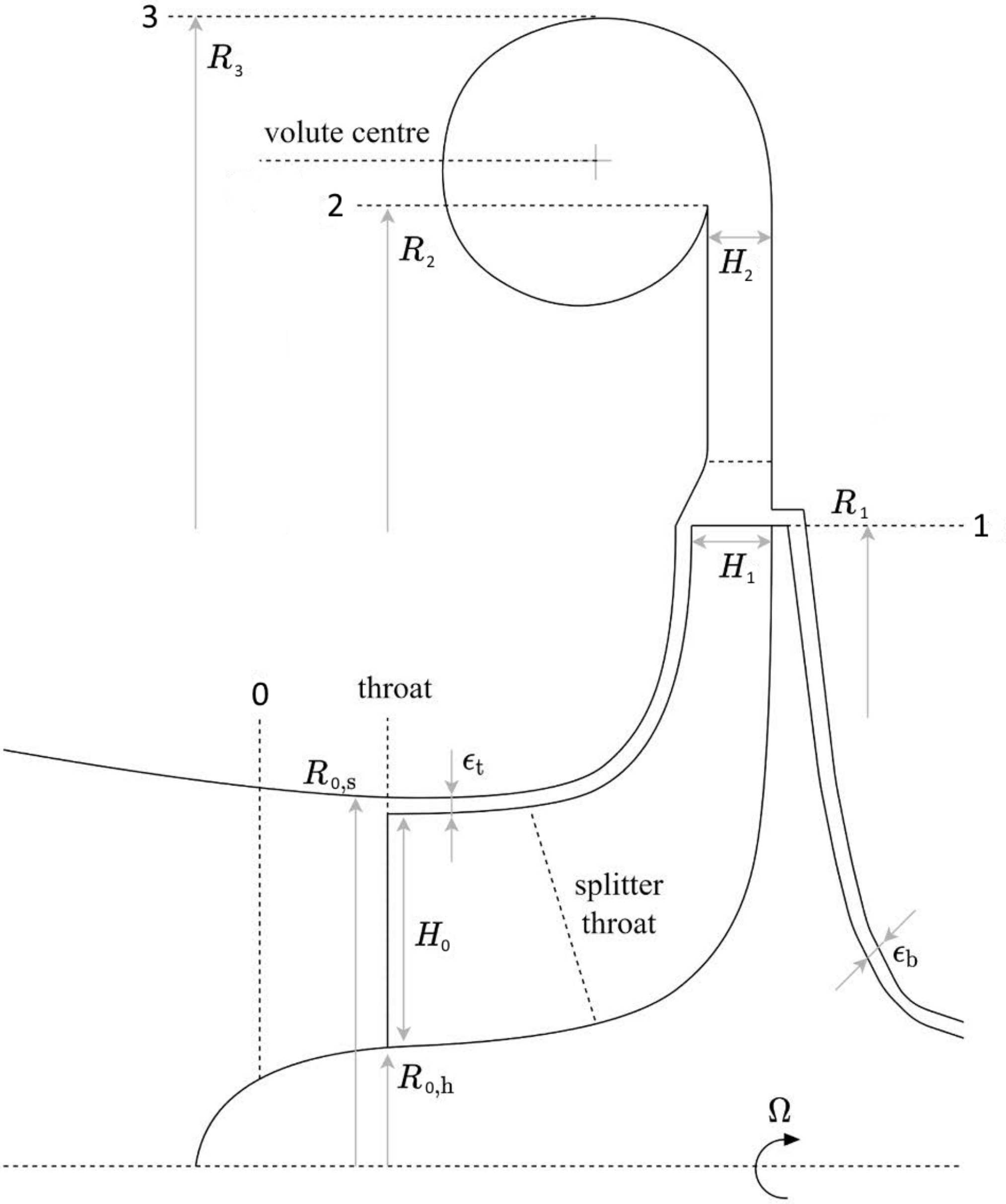

Figure 4.1: Meridional channel of the pump with numbering convention. Adapted from [28].

The program is built using an object-oriented approach. This means that every function and method can quickly access and update the flow properties at each station. It computes flow properties in the same order as the flow passing through the machine but in an iterative manner. The overall design workflow of the program is shown in Figure 4.2 below.

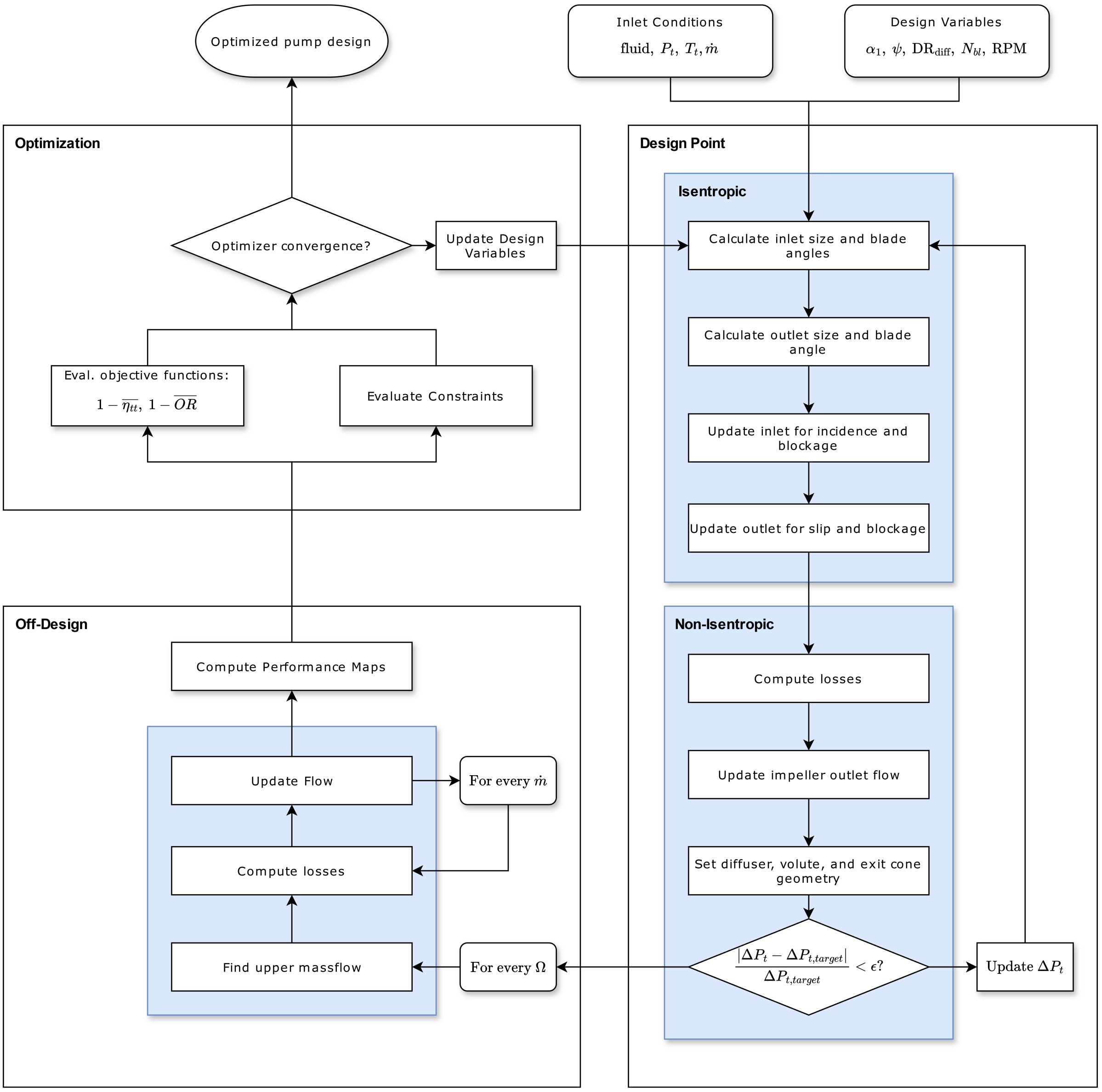

Figure 4.2: TurboSim architecture

The following sections briefly overview the programs' various modules. The fundamental methodology is laid out in chapter 3. However, practical considerations are not accounted for. This is explained here.

4.2.1 On-Design Performance

This module is at the core of the reduced-order model. It designs a pump stage to achieve the prescribed pressure rise. The following set of inputs are required to initialize the process:

	Parameter	Symbol	Unit	Data type
Basic Settings	Fluid	-	-	string
	Equation of State	EoS	-	string
	Outlet Station	-	-	int
	Inlet Total Pressure	P_{t0}	Pa	float
	Inlet Total temperature	T_{t0}	K	float
	Inlet Mass Flow	$\dot{m}$	kg/s	float
Design Variables	Total Pressure Rise	ΔP_t	Pa	float
	Outlet Absolute Flow Angle	α_2	deg	float
	Isentropic Work Coefficient	ψ_{is}	-	float
	Diffuser radius ratio	R_3/R_2	-	float
	Impeller Inlet Shape Factor	k_n	-	float
	Total Number of Blades	N_{bl}	-	int
	Rotational Speed	RPM	rev/min	int

Table 4.1: Inputs required to initialize the On-Design performance routine

A few notes about these inputs:

- The selected fluid should be available in the corresponding thermodynamic library chosen through the equation of state (EoS) model (HEOS, REFPROP).
- Parameters in *italic* are optional. They can be set to zero for default settings. If the impeller outlet absolute flow angle α_2 or the total number of blades N_{bl} are unknown, setting them to zero to allow for an automatic computation, as explained in chapter 3.
- The number of components modeled is determined by the outlet station number, as follows:
  - **1**: Impeller
  - **2**: Impeller + Vaneless Diffuser
  - **3**: Impeller + Vaneless Diffuser + Volute
  - **4**: Impeller + Vaneless Diffuser + Volute + Conical Diffuser
- To size the inlet, various options are available:
  - *None*: Minimum relative inlet velocity (subsection 3.5.2.A)
  - n_{ss}: Selected suction speed (subsection 3.5.2.B)
  - λ_w, λ_c: Selected λ_c coefficients (default λ_c = 1.1), (subsection 3.5.2.D)

Furthermore, one of the following slip models must be selected:

Model	Options	Data type
Slip	backstrom wiesner gulich qiu none	string

Table 4.2: Available Slip Models

This first module begins by sizing the pump geometry while only considering the isentropic head. This geometry serves as a baseline to which the effects of incidence, blockage, slip, and losses are added. The baseline geometry is modified accordingly to account for these effects.

Firstly, the inlet blade angle β_{0B} is designed to have zero incidence at the design point (BEP) while accounting for blade blockage. The outlet blade angle β_{1B} is designed such that the effects of slip and blockage are iteratively compensated for to achieve the prescribed *isentropic* head. This angle is limited to a radial design $\beta_{1B} = 90°$, after which performance is degraded due to a reduction in the tangential velocity component V_{1t} from slip.

Now that the blade angles are set, losses are accounted for through the multiple models available. Based on several loss-model reviews ([79], [56], [55], [28]), the following loss set is recommended for centrifugal turbopumps.

	Loss	**Model**	**Reference**
Internal Losses	Incidence	**aungier** galvas isentropic	Equation 3.78
	Skin Friction	**jansen** gulich isentropic	Equation 3.79
	Tip Clearance	**jansen** gulich gulich-mod isentropic	Equation 3.88
	Separation	**oh** isentropic	Equation 3.95
	Loading	**aungier** coppage rodgers isentropic	Equation 3.98
	Mixing	**aungier** johnston isentropic	Equation 3.101
External Losses	Leakage	**jansen** aungier isentropic	Equation 3.111
	Recirculation	**coppage** oh isentropic	Equation 3.113
	Disk Friction	**daily** isentropic	Equation 3.114
Other Losses	Vaneless Diffuser	**stanitz** isentropic	Equation 3.116
	Volute	**japikse**	Equation 3.120
	Exit Cone	**friction**	Equation 3.123

Table 4.3: Available loss models. Recommended set highlighted in bold and referenced.

With the impeller geometry set and the loss models selected, the remaining components are designed (if chosen so). The procedure is fairly straightforward. The diffuser, volute, and exit cone are discretized streamwise from the input to the output. Through the conservation of energy and momentum, the flow properties are known. If desired, friction losses can be accounted for, as explained in chapter 3. Once the losses for each component are computed, the resulting enthalpy rise at the outlet station is calculated:

$$\Delta h_t = \Delta h_{t,\text{is}} - \sum \Delta h_{t,\text{loss}} \tag{4.1}$$

With this newfound enthalpy rise, the total quantities (p_t, ρ_t, T_t) at the outlet are found by updating the thermodynamic state of the flow. Now, the actual pressure rise after losses is computed and normalized to obtain a residual:

$$\text{res} = \frac{\Delta P_{t,\text{target}} - \Delta P_{t,\text{designed}}}{\Delta P_{t,\text{designed}}} \tag{4.2}$$

Every step up to this point is wrapped into the `fsolve` optimizer from `SciPy`, which attempts to minimize the value of Equation 4.2 by varying the target pressure rise $\Delta P_{t,target}$. In other words, the optimizer searches for an isentropic pressure rise such that when including losses, the resulting pressure rise matches the input target. As expected, this results in a higher isentropic pressure rise than prescribed from the inputs.

4.2.2 Off-Design Performance

The pump off-design performance module is fairly straightforward. First, the operating range is established from zero mass flow to the mass flow corresponding to zero head under isentropic conditions. This is not achieved in practice, as the thermophysical model does not converge at mass flows far from the design point (relative to the rpm). Then, the on-design module is run at each speed line for each mass flow rate. By doing this, an operational map of the pump is constructed. Every variable of interest is stored for each mass flow rate and speed line.

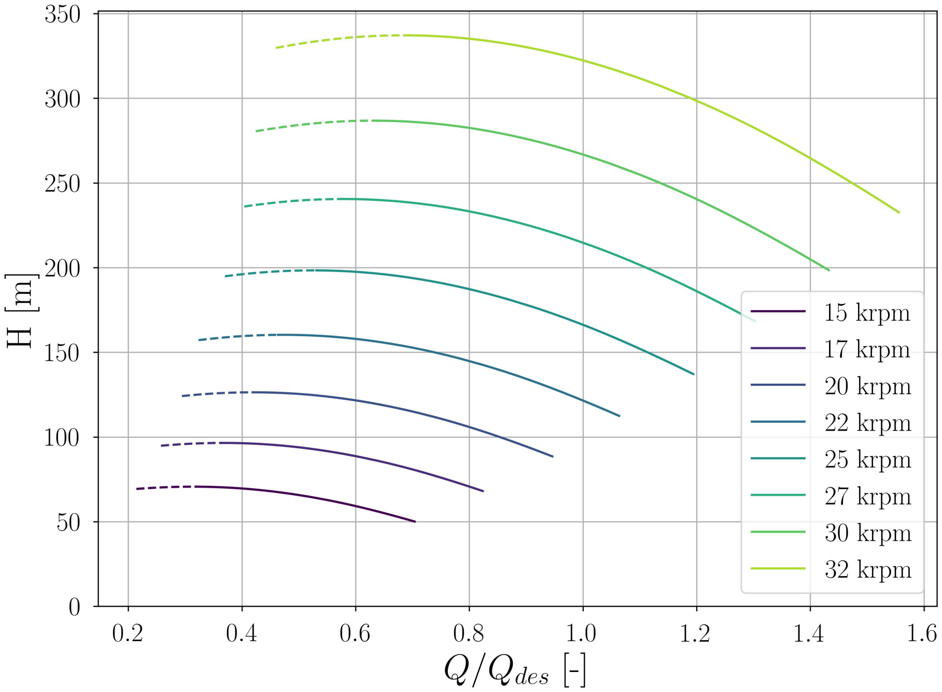

Figure 4.3: H-Q operational map of a pump running on R245FA. Dashed lines represent an unstable operating regime.

For each operational point, both the NPSH$_R$ and NPSH$_A$ are calculated to assess if cavitation may occur.

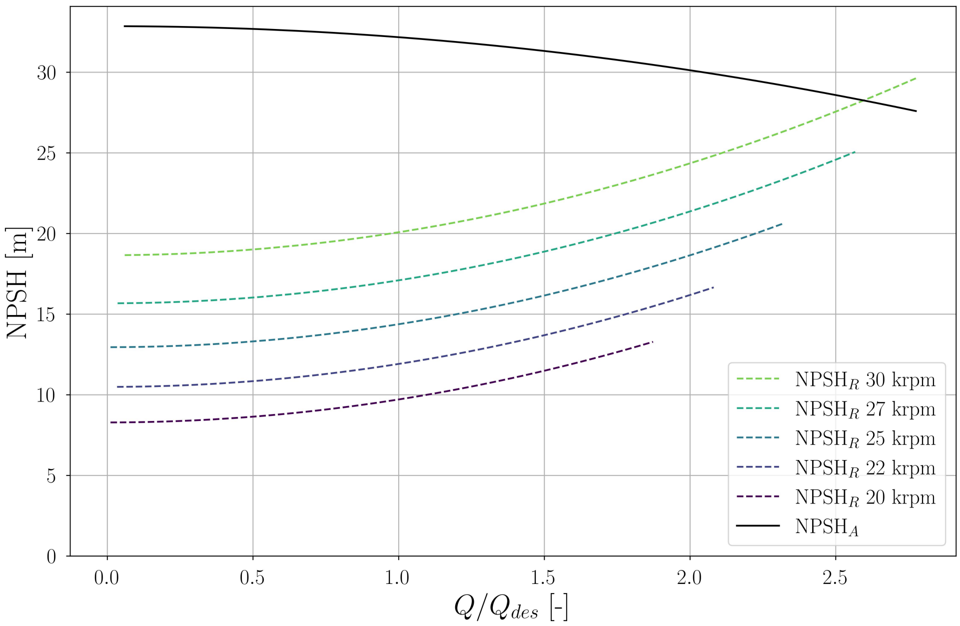

Figure 4.4: NPSH$_R$, and NPSH$_A$ for a R245FA pump. The region to the right of the intersection of the NPSH$_R$ and NPSH$_A$ lines indicates a cavitating regime.

4.2.3 Optimization

The optimization algorithm used in this study is `NSGA-II` [23], an evolutionary algorithm for multi-objective constrained optimization problems. This is implemented through `Pymoo` [12], an open-source Python library. A genetic algorithm has the following benefits over a gradient-based method:

1. The gradients of the objectives and constraints are discrete and cannot be determined analytically.
2. The multiple design variables and non-linear constraints make numerical computation of the gradients very costly.
3. Genetic algorithms allow for efficient design space exploration and are less prone to getting stuck in a local minimum than a gradient-based method.

An initial population of ten individuals for each design variable is initialized, sampling the design space using the Latin hypercube method (LHM), a statistical method for generating a near-random sample of parameter values from a multidimensional distribution. Then, the population evolves until either the maximum number of generations is reached or the relative improvement of the previous generations falls below a predefined threshold. The optimization variables are floating-point numbers except for the number of blades and RPM, which are integers. The optimization problem definition is shown below:

$$
\begin{array}{lll}
\text{minimize} & (1-\overline{\eta_{tt}}),\,(1-\overline{\mathrm{OR}}_{\mathrm{des}}) & \\
\text{subject to} & \dfrac{R_{1,\mathrm{hub,\,min}}-R_{\mathrm{inlet}}}{R_{1,\mathrm{hub,\,min}}}\leq 0, & \text{Min. hub radius} \\
 & \dfrac{D_{\mathrm{mill\ tip}}-D_{\mathrm{throat}}}{D_{\mathrm{mill\ tip}}}\leq 0, & \text{Min. throat dimension} \\
 & \dfrac{H_{2,\mathrm{min}}-H_2}{H_{2,\mathrm{min}}}\leq 0, & \text{Min. impeller outlet blade height} \\
 & \dfrac{R_3-R_{4,\mathrm{max}}}{R_{4,\mathrm{max}}}\leq 0, & \text{Max. volute outlet radius} \\
 & \dfrac{\mathrm{AR}_{\mathrm{vol,\,min}}-\mathrm{AR}_{\mathrm{vol}}}{\mathrm{AR}_{\mathrm{vol,\,min}}}\leq 0, & \text{Min. volute AR} \\
 & \dfrac{\mathrm{AR}_{\mathrm{vol}}-\mathrm{AR}_{\mathrm{vol,\,max}}}{\mathrm{AR}_{\mathrm{vol,\,max}}}\leq 0, & \text{Max. volute AR} \\
 & \dfrac{|\Delta P_{t,\mathrm{des}}-\Delta P_{t,\mathrm{target}}|}{\Delta P_{t,\mathrm{target}}}-\dfrac{\Delta P_{t,\mathrm{err\ max}}}{100}\leq 0, & \text{Max. deviation w.r.t. design point } \Delta P \\
 & \dfrac{\max(F_{ax,\mathrm{des}})-F_{ax,\mathrm{max}}}{F_{ax,\mathrm{max}}}\leq 0, & \text{Max. bearing axial thrust} \\
 & \dfrac{\max(P_{el,\mathrm{des}})-P_{el,\mathrm{max}}}{P_{el,\mathrm{max}}}\leq 0, & \text{Max. electric motor mech. power} \\
 & \dfrac{\max(T_{\mathrm{des}})-T_{\mathrm{max}}}{T_{\mathrm{max}}}\leq 0, & \text{Max. electric motor torque} \\
 & \dfrac{\max(\mathrm{NPSH}_R)-\min(\mathrm{NPSH}_A)}{\max(\mathrm{NPSH}_R)}\leq 0, & \text{Net Positive Suction Head (NPSH)} \\
\text{with design variables} & \alpha_1,\psi,k_n,N_{bl},\mathrm{DR}_{\mathrm{diff}},\mathrm{RPM} &
\end{array}
$$

Furthermore, the optimizer requires convergence criteria to terminate the process. These have been set as the following:

- **xtol** = 5×10^{-4}: Tolerance for the change in the decision variables (x). If the change in the decision variables is less than a certain number of iterations, the optimization will terminate. This ensures that the algorithm stops when the solution has converged in the decision space.
- **cvtol** = 1×10^{-6}: Tolerance for the constraint violation (cv). The optimization will terminate if the maximum constraint violation exceeds this value. This ensures that the solutions are feasible with respect to the constraints.
- **ftol** = 1×10^{-3}: Tolerance for the change in the objective function values (f). If the change in the objective function values is less than a certain number of iterations, the optimization will terminate. This ensures that the algorithm stops when the solution has converged in the objective space.
- **n_skip** = 1: Number of generations to skip between checks for convergence.
- **period** = 3: Frequency (in generations) at which the convergence criteria are checked.
- **n_max_gen** = `int(config['Optimization']['n_max_gen']) * len(lower_bounds)`: Maximum number of generations allowed for the optimization process. This provides an upper limit on the number of generations to prevent the algorithm from running indefinitely.
- **n_max_evals** = 100: Maximum number of function evaluations allowed, providing another upper limit to prevent excessively long runs.

4.3 Verification Methodology

This section documents the results of the TurboSim model and the computational fluid dynamics (CFD) simulation, and 1D calculations from commercially available software packages. Then, these results are compared.

In this work, `CFTurbo` [15] and `ANSYS CFX` [4] are made use of to assess the accuracy of the results obtained with `TurboSim`. `CFTurbo` is a proprietary turbomachinery design software built on turbomachinery fundamentals using meanline design principles. It can generate 3D computer-aided design (CAD) geometry and calculate and report isentropic flow quantities. Furthermore, `ANSYS` Workbench is used to model and mesh the 3-dimensional geometry required for CFX using TurboGrid. The CFD simulations are run on the `DelftBlue` high-performance cluster (HPC) provided by `TU Delft` running on 32 cores of an Intel Xeon Gold E5-6226R 16C at 2.9GHz.

Verification is carried out in two steps. First, on-design, isentropic meanline results and geometry generation results are compared against `CFTurbo`. Then, off-design 3D viscous simulations are carried out in `ANSYS CFX` to assess loss model performance.

4.3.1 CFTurbo

As a general turbomachinery design program, `CFTurbo` has several capabilities from which the centrifugal pump design module is used. `CFTurbo` has limited loss modeling capabilities as it only considers global efficiency using a hydraulic loss efficiency factor η_h and a volumetric efficiency factor η_v. This approach is overly simplistic for the verification purposes of this work. Therefore, `CFTurbo` is only used to verify the main calculation routine of this work under isentropic conditions by setting these efficiency factors to 100%.

`CFTurbo` is fed the same inputs used in TurboSim, allowing for a straightforward process. The fluid, inlet conditions (P_t, T_t), and main performance parameters (Head H, mass flow rate $\dot{m}$, and rotational speed n) are set. In subsequent steps, other design variables are input: Blade number N_{bl}, blade thicknesses t_{le}, t_{te}, work coefficient ψ, inlet shape factor k, and inlet diameter d_1.

4.3.2 ANSYS

The figure below shows that various modules are used and connected to run automated simulations within the ANSYS Workbench environment.

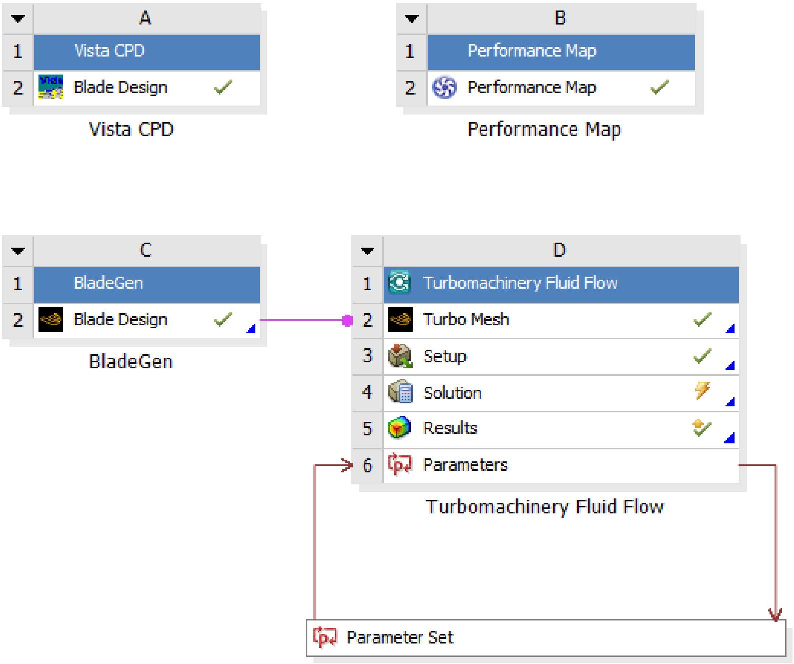

Figure 4.5: ANSYS Workbench set-up.

First, `Vista CPD` generates a default pump impeller geometry, which is fed into `BladeGen` and modified to precisely match the meridional and blade shapes generated by the presented ROM. Then, `Turbo Mesh` creates a structured mesh and sends it into `CFX` for pre-processing, solving, and post-processing. Lastly, the setup process is automated to obtain speedline performance data. The `Performance Map` block generates discrete design points for the parametric `Parameter Set` block that monitors and runs simulation batches with changing rotational speeds and mass flows.

BladeGen (Geometry Definition)

`BladeGen` is a specialized software tool within the `ANSYS` software suite that designs blades for turbines, compressors, pumps, and fans. It provides a graphical interface to parametrically define the blade's profile by specifying key parameters such as blade angles, thickness distributions, blade wrap distributions, and meridional contours. `VistaCPD` initializes the geometry, which is then modified to the exact design specifications. As the impeller is axisymmetric, only one passage is modeled with periodic boundary conditions to reduce the computational cost.

TurboGrid (Meshing)

`TurboGrid` is a powerful meshing program that creates structured meshes for various turbomachinery components. After importing the desired geometry, the rotational axis and machine type are selected, and `TurboGrid` can automatically generate a reasonably structured mesh. The mesh block topology partitions for the impeller of Case A are shown below.

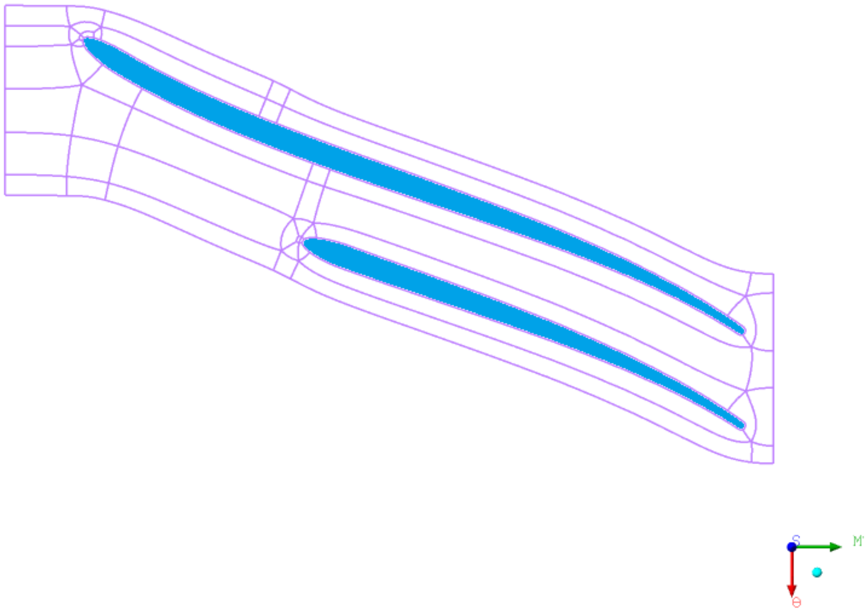

Figure 4.6: Unwrapped blade-to-blade mesh topology for Case A

The generated mesh is refined further to ensure a high-quality but computationally reasonable mesh. A mesh sensitivity study is done in Figure 4.3.2. It uses elements with proportional boundary layer refinement control and adaptive first-element offset. A detailed view of the meridional inlet mid-section mesh projection is seen below. The inlet section has an H-Grid type mesh, with a target of 10 elements at the outlet section. The outlet region is further refined to better capture flow non-uniformities for the mass flow averaging of flow properties. Additionally, this enables a better domain interface if modeling a diffuser downstream.

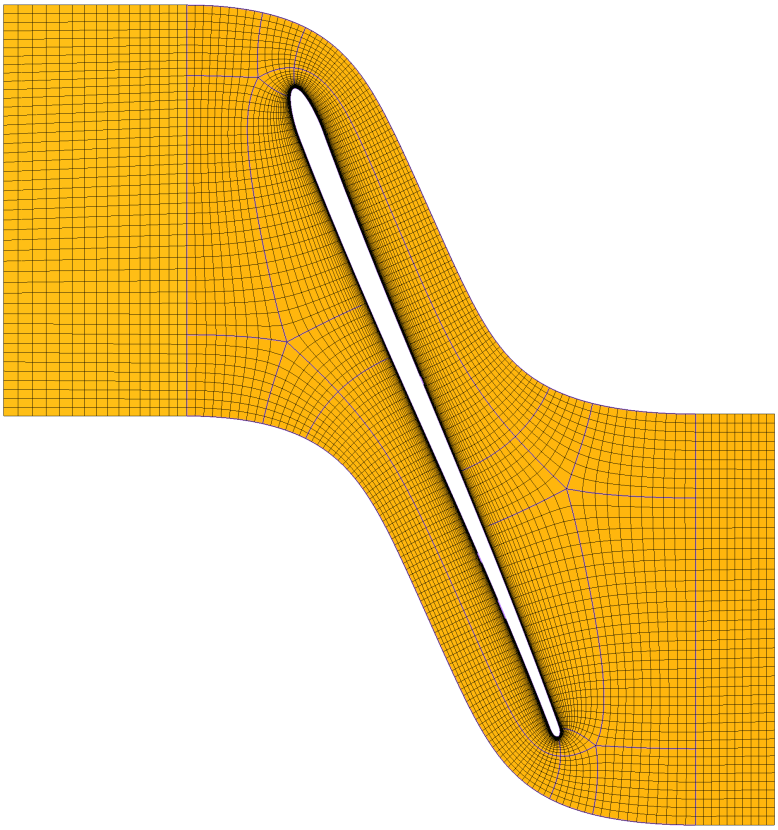

Figure 4.7: Truncated blade-to-blade mesh view of a LOX pump blade at the shroud. The inlet is on the left, and the outlet is on the right.

CFX (CFD Solver)

`CFX` is used for steady-state, single passage RANS simulations to assess the pump performance by running multiple simulations where the rotational speed and mass flow rate are varied over a prescribed operating range.

After importing the mesh into `CFX-Pre`, the *Turbo Setup* tool is used to set up the simulation. The rotational speed, mesh regions, fluid properties, periodic boundary conditions, and inlet and outlet boundary conditions are set. The fluid properties are imported from *REFPROP* in a tabulated format as an `.RGP` file, which allows for very quick fluid thermodynamic state updates. The boundary conditions imposed are rotational speed n, inlet total pressure P_t and temperature T_t, and the outlet mass flow rate $\dot{m}$. The turbulence intensity at the inlet is set to $\kappa = 5\%$. The $\kappa - \omega$ SST turbulence model is also used with total energy heat transfer and the viscous work term enabled. The high-resolution advection scheme and turbulence numerics are used. This 'High Resolution' scheme implements a non-linear blending factor between a first-order and a second-order upwind discretization scheme, which is adjusted throughout the solution. A summary of the settings used through the project is shown in Table 4.4 below.

Setting	Value
Advection Scheme	High Resolution
Turbulence Numerics	High Resolution
Min Iterations	200
Max Iterations	1000
Min RMS	1e-5
Time Scale Control	Auto
Boundary Conditions	$P_t, T_t - \dot{m}$
Inlet Turbulence Intensity	5%

Table 4.4: CFX-Pre Settings

To monitor convergence, RMS residuals of pressure, momentum, turbulence, and heat transfer rates are monitored until dropping below a value of 1e-5. Additionally, a monitor is defined to track the evolution of the head during the simulation to quickly assess problems. The mass flow averaging method is used since the flow may be highly nonuniform at the outlet region due to separation and mixing. Since the flow is subsonic and density is quasi-constant, the averaged velocity conserves the momentum flux. This monitor is defined as an `ANSYS CEL` (`CFX` Expression Language):

```
Head Monitor = (
massFlowAve(Total Pressure in Stn Frame)@Blade TE -
massFlowAve(Total Pressure in Stn Frame)@Blade LE)
/(9.81 * ave(Density)@Blade LE)
```

It was seen that most simulations with 400k mesh elements could converge successfully from initial conditions after around 300 iterations. Those that did not successfully converge usually lay at the extremes of the operating range and showed large separation and recirculation regions in the flow field solution. These unsteady phenomena do not converge well in a steady-state RANS simulation; see Figure 4.8. Furthermore, most simulations are initialized with the previous solution as initial conditions (this is done when simulating various speed lines and mass flow rates). A minimum and maximum iteration count of 200 and 1000 per design point was set to ensure convergence without high computational cost. Simulations with non-converged solutions are discarded.

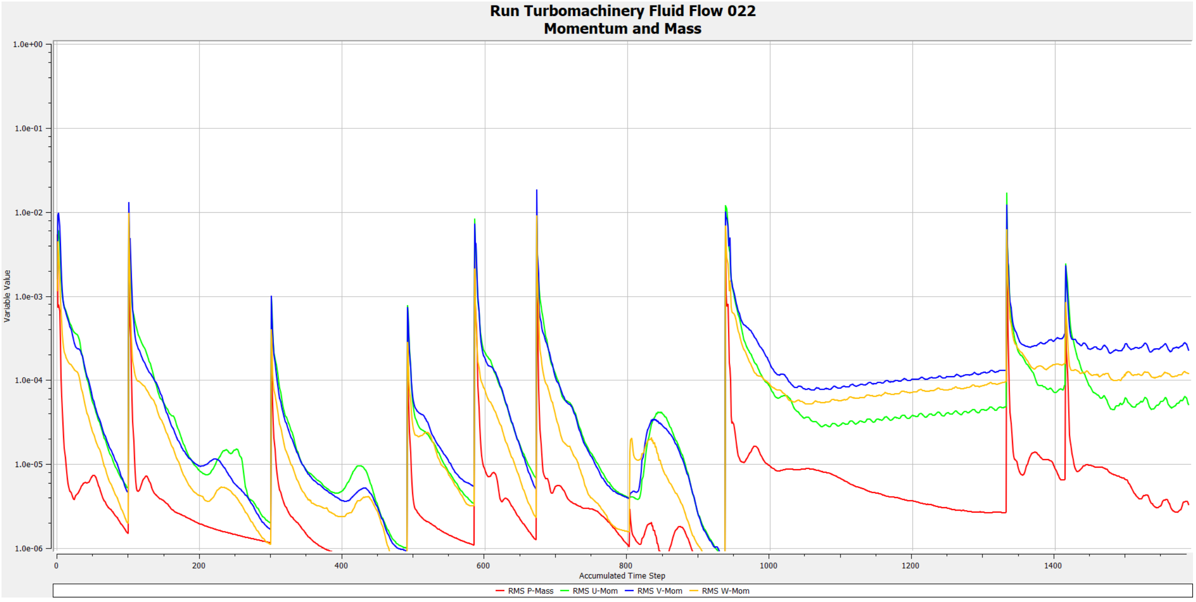

Figure 4.8: Pressure and velocity RMS residuals of a speed line simulation batch.

Lastly, two options are available as domain interfaces when modeling a stationary diffuser downstream: Mixing plane or frozen rotor. A mixing plane interface is the most commonly used in steady-state turbomachinery simulations since it performs a circumferential averaging of the flow quantities. This is the option used in this project. Alternatively, a frozen rotor interface is another common option, where the flow field is solved for a given angular offset between both components. This is useful when fluid structures must be preserved downstream.

4.4 Verification Study Results

The results of the CFD simulations and CFTurbo meanline calculations are shown in this section. The output from the CFD solver is inspected using CFX-Post. A pump impeller report is generated with the variables of interest at various points: inlet, outlet, blade leading edge, and blade trailing edge.

4.4.1 Test Cases

Two cases are studied to verify TurboSim. Due to time and resource constraints, only the impeller is modeled.

For **Case A**, a low specific speed pump (n_q = 8.3) with a refrigerant (R245FA) as a working fluid is chosen, based on the work from [78]. Only the impeller is modeled. The BEP design parameters are listed below. For **Case B**, a moderate specific speed (n_q = 51.4) liquid oxygen turbopump is modeled after the space shuttle's main engines (RS-25). A summary of the two cases is shown below.

	Parameter	Symbol	Unit	Case A	Case B
Basic Settings	Fluid	-	-	R245FA	Oxygen
	Equation of State	EoS	-	HEOS	HEOS
	Outlet Station	-	-	1	1
	Inlet Total Pressure	P_{t0}	bar	6.35	60
	Inlet Total temperature	T_{t0}	K	308.15	80
	Inlet Mass Flow	$\dot{m}$	kg/s	0.5	48
Design Variables	Total Pressure Rise	ΔP_t	bar	19.05	200
	Impeller Inlet Shape Factor	k_n	-	0.8775	0.8
	Total Number of Blades	N_{bl}	-	14	6
	Rotational Speed	RPM	rev/min	25000	22000

Table 4.5: Input summary for verification cases

4.4.2 CFTurbo

The results of the isentropic on-design meanline calculation from TurboSim are compared with with `CFTurbo`. Below, the main flow quantity outputs from this work are compared with `CFTurbo` and shown in Table 4.5

		Case A			Case B		
Variable	**Unit**	**ROM**	**CFTurbo**	**Difference**	**ROM**	**CFTurbo**	**Difference**
U_0	[m/s]	11.86	11.90	0.34%	98.31	98.34	0.03%
V_0	[m/s]	3.06	3.10	1.31%	45.78	45.79	0.02%
V_{0t}	[m/s]	0.00	0.00	0.00%	0.00	0.00	0.00%
V_{0m}	[m/s]	3.06	3.10	1.31%	45.78	45.79	0.02%
W_0	[m/s]	12.30	12.35	0.41%	109.72	109.74	0.02%
W_{0t}	[m/s]	-11.86	-11.90	0.34%	-98.31	-98.34	0.03%
β_0	[deg]	-73.72	-71.80	2.60%	-62.19	-62.20	0.01%
β_{0B}	[deg]	-68.75	-66.25	3.64%	-57.11	-57.14	0.05%
U_1	[m/s]	51.21	51.20	0.02%	202.68	202.69	0.01%
V_1	[m/s]	28.41	28.40	0.04%	86.94	87.28	0.39%
V_{1t}	[m/s]	28.35	28.40	0.18%	81.54	81.91	0.46%
V_{1m}	[m/s]	1.71	1.70	0.58%	30.17	30.19	0.06%
W_1	[m/s]	22.91	22.90	0.04%	124.84	124.41	-0.34%
W_{1t}	[m/s]	-22.85	-22.90	0.22%	-121.14	-120.78	-0.30%
β_1	[deg]	-85.71	-85.70	0.01%	-76.01	-75.94	-0.10%
β_{1B}	[deg]	-84.16	-84.20	0.05%	-68.87	-69.96	1.56%

Table 4.6: Flow properties at the impeller inlet and outlet mid-span from TurboSim and `CFTurbo`.

The resulting geometry from both methods is in very good agreement. These results are consistent with other case studies performed.

4.4.3 CFD

The CFD results are now shown and compared to the results obtained with TurboSim. First, a mesh independence study follows the methodology shown in Figure 4.3.2. Then, the qualitative flow field is shown. Finally, the performance and efficiency maps are shown.

Mesh independence

The results of CFD simulations are very sensitive to the given inputs and configuration parameters. Furthermore, performing a grid independence study is important to show that the results obtained from CFD are independent of the mesh resolution. This is done by running the same simulation multiple times while increasing the mesh size without changing any other parameter. The BEP of the pump was chosen as the benchmark point. A table with the various mesh sizes and quantities of interest is shown in Figure 4.10, and Figure 4.10 below.

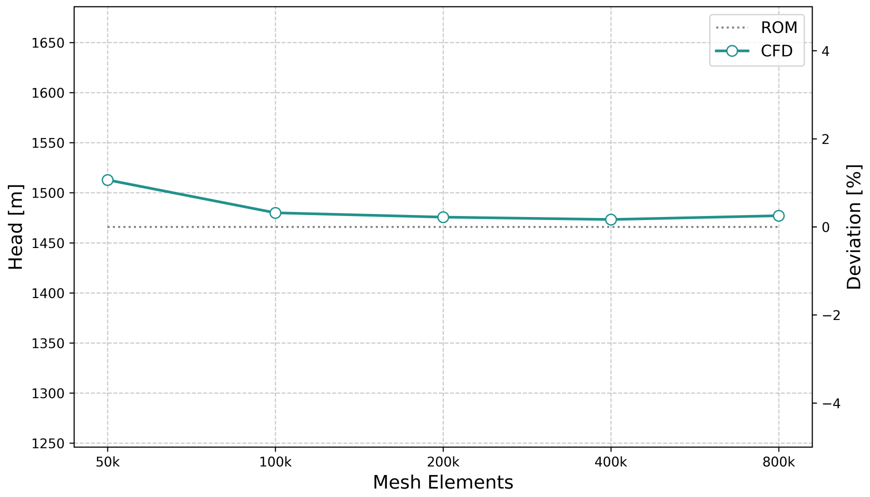

Figure 4.9: Case A CFD mesh sensitivity analysis

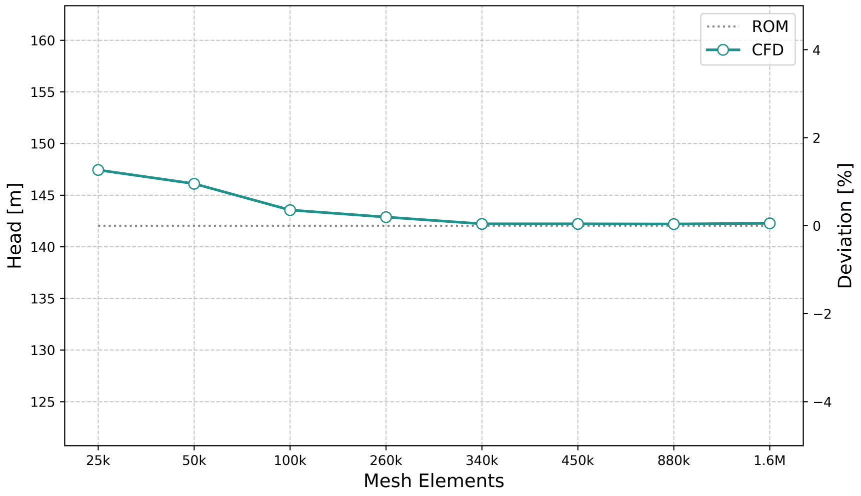

Figure 4.10: Case B CFD mesh sensitivity analysis

As the number of elements increases, the simulated head converges to a steady value. This is also in good agreement with the expected head from TurboSim. A 400k element mesh was conservatively chosen as computationally affordable while sufficiently accurate.

Flow Fields

Looking at the flow field of the impeller for Case A at the design point qualitatively, the direction of rotation is positive around the Z-axis.

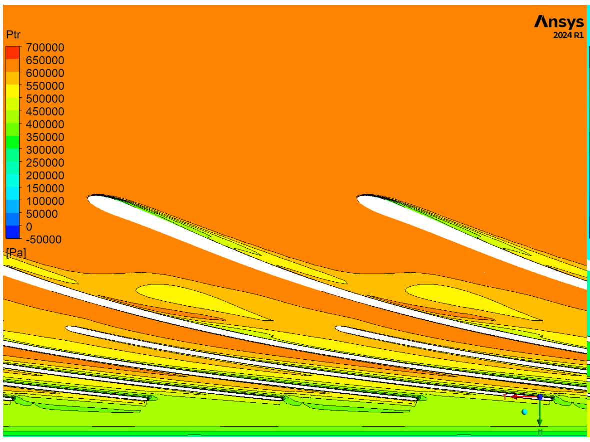

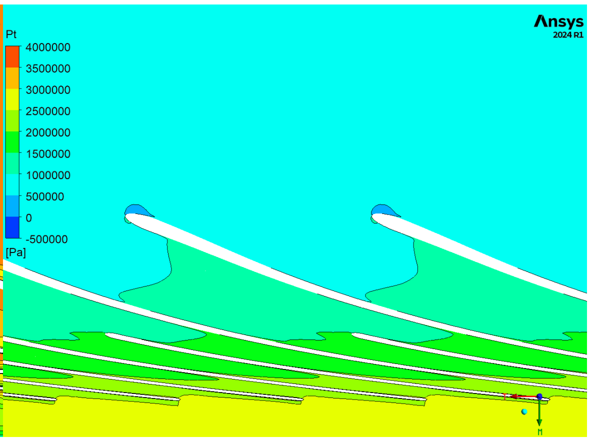

Figure 4.11: Blade-to-blade contour plot of the total pressure in the relative frame at 50% span.

Figure 4.12: Blade-to-blade contour plot of the total pressure in the stationary frame at 50% span.

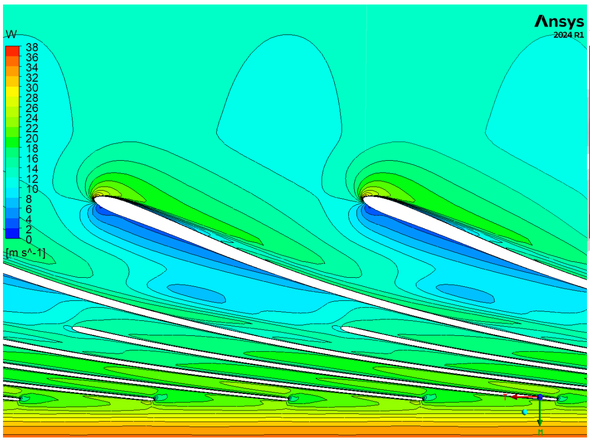

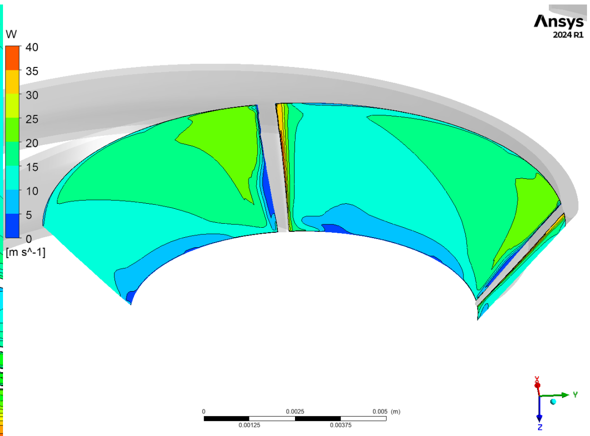

Figure 4.13: Blade-to-blade contour plot of the relative velocity in the stationary frame at 50% span.

Figure 4.14: Blade-to-blade contour plot of the relative velocity in the stationary frame at 50% span.

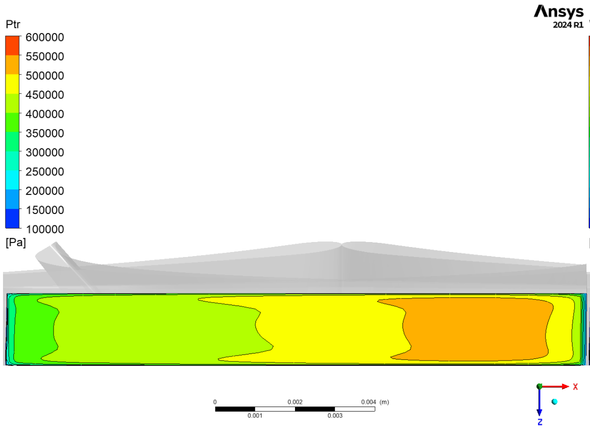

Figure 4.15: Blade trailing edge contour plot of the total pressure in the relative frame.

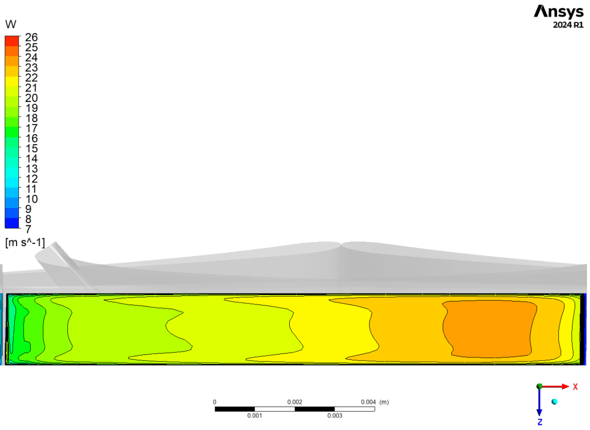

Figure 4.16: Blade trailing edge contour plot of the relative velocity in the stationary frame.

The flow remains attached throughout the impeller passage. Given that this is a steady-state RANS simulation with circumferential periodicity enabled per passage, the flow is mostly uniform. As expected, the total pressure increases along the meridional channel, and the trailing edge contour of the total pressure and relative velocities show that the pressure side of the blades is more highly loaded than the suction side. This trailing edge view also shows the boundary layers along the passage surfaces. Additionally, there seems to be a local pressure reduction bubble on the suction side of the leading edge, which, at higher flow rates or rotational speeds, could lead to the inception of cavitation.

4.4.4 Performance Maps

Examining the various performance maps resulting from both TurboSim and CFD to assess their relative agreement, the Flow-Head (H-Q) maps and the total-total efficiency η_{tt} maps are of interest, as they give a good insight into the loss modeling and the resulting head. Additional maps showing the expected torque, axial thrust, power, and NPSH margin are also shown.

Flow - Head map

predicted head, measured from the leading edge to the trailing edge. Three speedlines have been computed and simulated with CFD. Beginning with Case A:

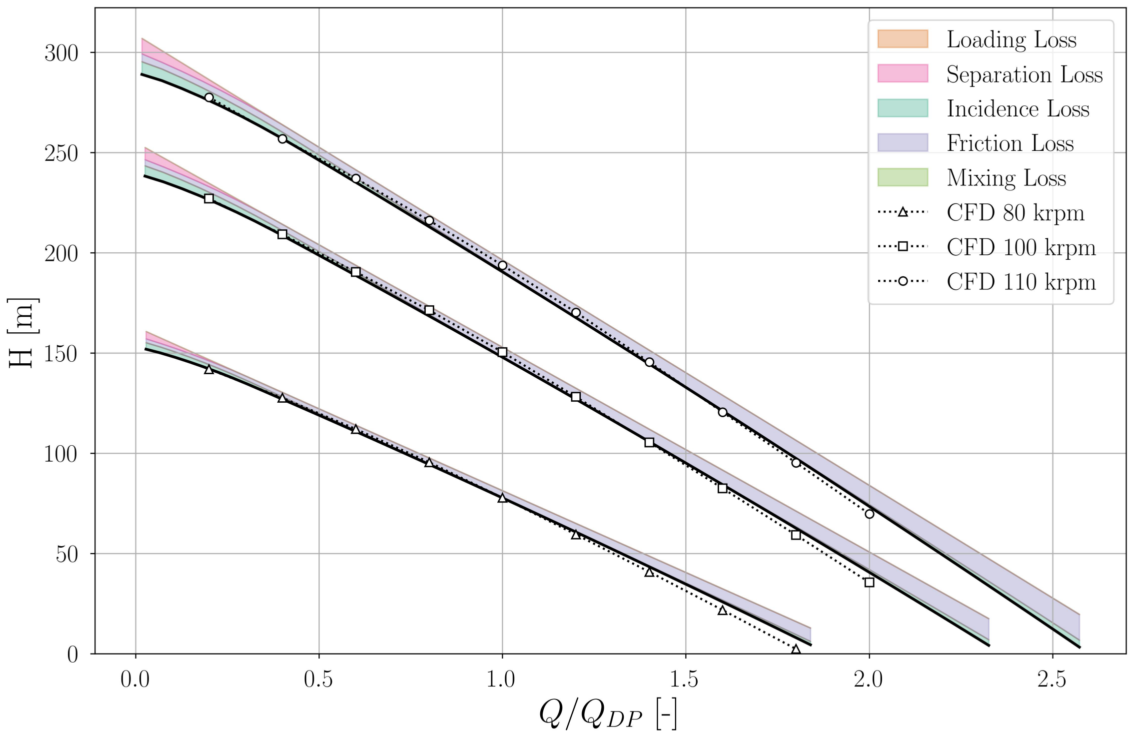

Figure 4.17: Head-Flow performance map from CFD vs. TurboSim for Case A

The head predictions with losses from TurboSim agree very well with the CFD results, even in off-design conditions. Some discrepancies are appreciable on the upper and lower ends of the working curve due to flow instabilities in the region. Furthermore, friction and loading losses dominate the operational map, especially away from the BEP. TurboSim overestimates the head at higher volumetric flow rates, suggesting that the loss mechanisms are not captured well in this regime. Furthermore, it is also apparent that in the region around the design point ($Q/Q_{des} \approx 1$), the CFD head is slightly higher than is expected with TurboSim.

Similarly, looking at Figure 4.18, the losses and CFD results for Case B superimposed:

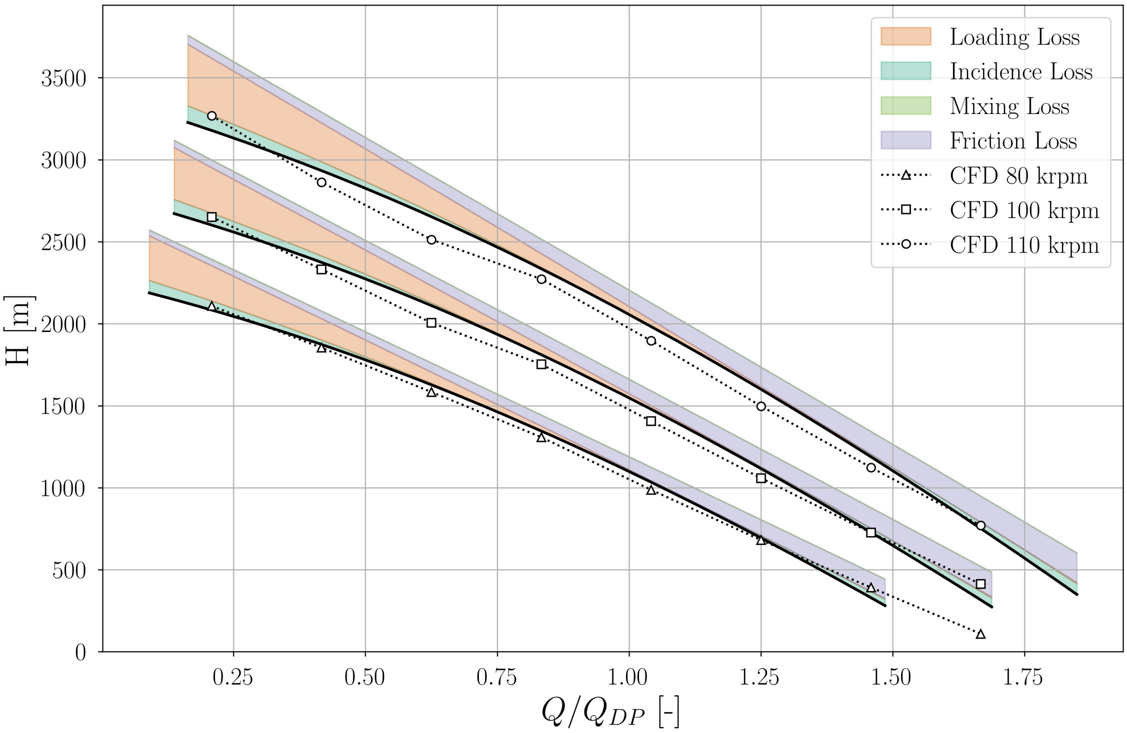

Figure 4.18: Head-Flow performance map from CFD vs. TurboSim for Case B

First of all, the loss breakdown is apparently different from that of Case A. Loading losses are much greater, and there seems to be no separation losses (which could be due to the different fluid, design, or operating conditions). The slope of the H-Q curve is in good agreement except at high flow rates. It looks like TurboSim overestimates the losses in this region. Furthermore, at the low volumetric flow and higher rotational rate region, the discrepancies grow, indicating that the loss mechanisms do not fully agree with the CFD results.

Blade loading is again a major source of losses. Friction losses, however, are not as predominant in this case. This makes sense as the Reynolds number has substantially decreased as the mass flow has increased.

Finally, it is worth noting that the CFD results my not be entirely accurate and likely do not represent real-world performance. Many assumptions and simplifications have been taken to allow for computationally acceptable simulations (steady state, RANS, limited domains, moderate mesh element count, single-phase fluids, adiabatic).

Efficiency Map

Now, the efficiency of the simulation is compared against the 1D model, using an alternative (but equally useful) definition of internal efficiency. This definition is chosen because it can be directly obtained from TurboSim and is easier to measure directly from CFD. The analysis begins by decomposing the mechanical work $w = w_{\text{net}} + w_w$ input to the system into useful effect w_{net} and lost work w_w. The useful effect term is known:

$$w_{\text{net}} = \frac{\Delta P}{\rho} + \frac{V_1^2 - V_0^2}{2} + g\Delta z \tag{4.3}$$

The gravitational head is assumed negligible. Furthermore, given the incompressible, low-mach regime of centrifugal pumps and assuming adiabatic flow, the dissipated work can be obtained from the Gibbs relations:

$$w_w = \int T \cdot ds = C_v \cdot \Delta T \tag{4.4}$$

Arriving at a definition for internal efficiency:

$$\eta_{tt,int} = \frac{w_{\text{net}}}{w_{\text{net}} + w_w} \tag{4.5}$$

External losses are not considered as these are not captured by CFD without complex secondary flow modeling. Now, the pump efficiency over various speed lines can be compared to the 1D model.

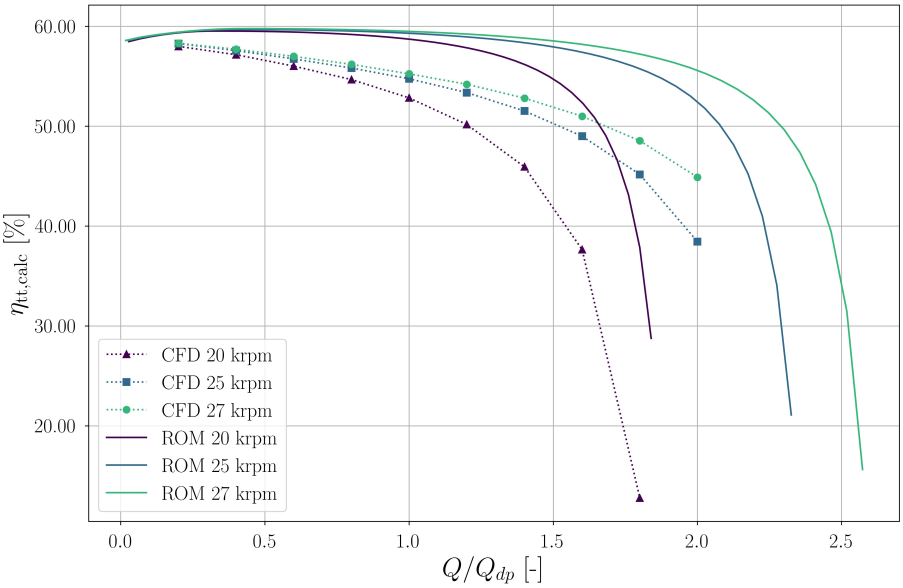

Figure 4.19: Efficiency map results from CFD vs. TurboSim for Case A

While the efficiency lines for both methods follow the same trends, appreciable discrepancies are seen. ROM and CFD efficiency lines show a similar trend where each speedline begins with similar efficiency, and as the mass flow increases, their efficiency quickly diverges. Lower RPMs show a faster decline in efficiency than higher RPMs.

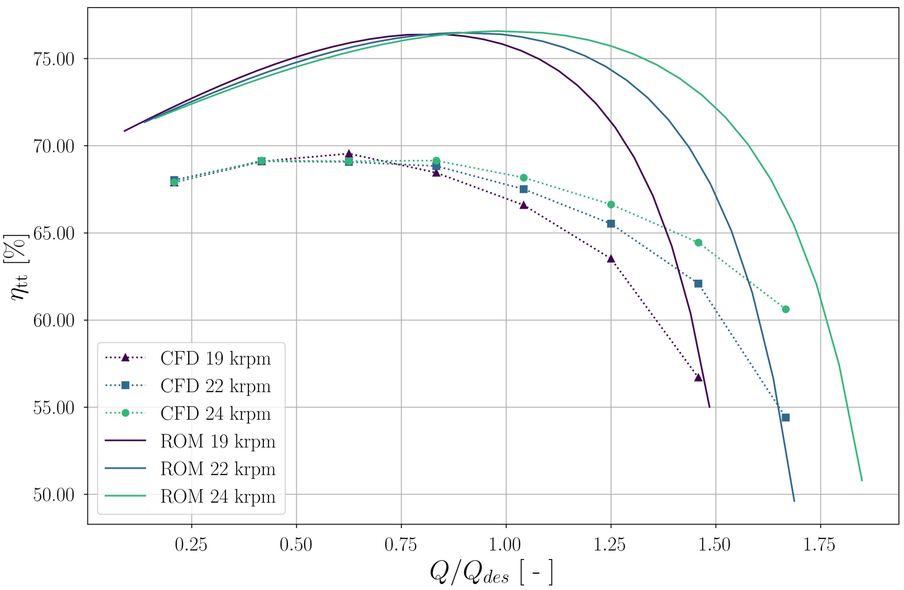

Figure 4.20: Efficiency map results from CFD vs. TurboSim for Case B

For Case B, CFD and ROM efficiency lines are qualitatively similar and follow almost the same trends. TurboSim predicts about a 20% higher efficiency compared to the CFD results.

It is hypothesized that the discrepancies in efficiency can be attributed to either the ROM loss models not accurately capturing the loss mechanisms of the flow, and/or a physically incorrect CFD simulation.

NPSH Map

The predicted NPSH operating map of Case A using the methodology from section 3.11 is shown below. The dashed lines indicate the required NPSH$_A$ at each rotational speed to avoid cavitation.

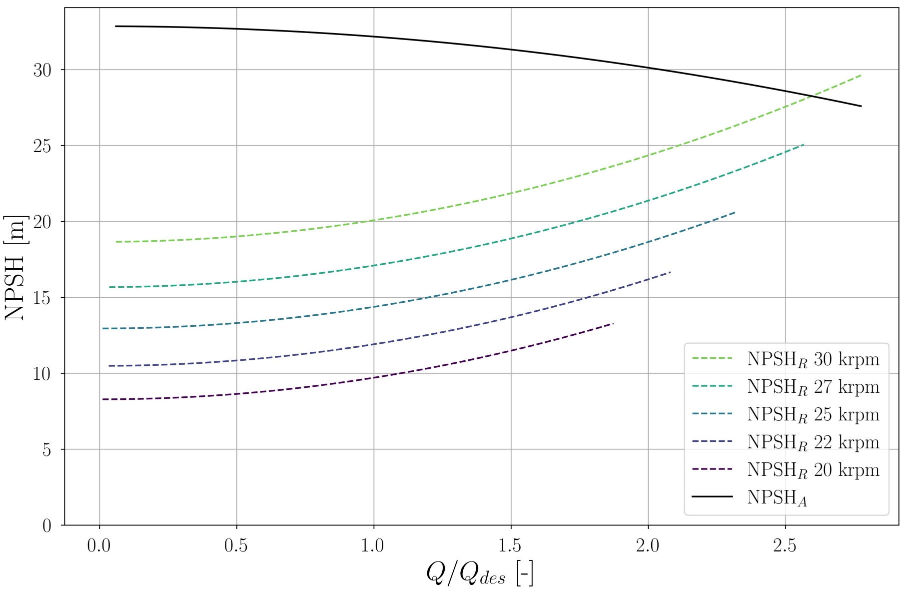

Figure 4.21: Net Positive Suction Head margin as a function of flow rate. The region to the right of the intersection of the NPSH$_R$ and NPSH$_A$ lines indicates a cavitating regime.

As the mass flow rate and the rotational speed increases, the local pressure around the leading edge of the blade decreases, in turn increasing the risk for cavitation. This is seen in Figure 4.21 as a rising NPSH$_R$ value with increasing flow rate. The NPSH$_A$ value steadily decreases with increased flow rate as the kinetic component of the total pressure increases, decreasing the static pressure $P_t = P + \frac{V^2}{2}$. At flow rates above the intersection of the NPSH$_A$–NPSH$_R$ curves, cavitation is expected.

5

Case Study: The ORCHID Pump

Organic Rankine Cycle (ORC) power systems are increasingly recognized for their ability to convert low-grade thermal energy into electricity, with particular interest in mini-ORC units (3-50 kWe) for heat recovery in the automotive and solar energy sectors. Efficient pumps and expanders are crucial for these systems, yet there is a lack of experimental data to validate design methodologies, which rely on non-validated tools [34].

To address this, TU Delft has developed the Organic Rankine Cycle Hybrid Integrated Device (ORCHID), a versatile research facility capable of continuous operation with different working fluids and operating conditions. The ORCHID has two interchangeable test sections: a supersonic nozzle with optical access for gas dynamic experiments on dense organic flows and a test bench for various mini-ORC expander configurations up to 80 kWe [34]. The facility aims to validate numerical codes, develop semi-empirical correlations for fluid-dynamic losses, and evaluate turbomachinery design methodologies. The initial focus is testing turbines for applications like solar power conversion and heat recovery from long-haul trucks.

As an applied case study, the design methodology presented in the previous chapters is used to design a centrifugal pump for the ORCHID, replacing the current reciprocating pump.

5.1 Overview of the ORCHID

Here is a summary of the key features and parameters of the ORCHID. Below is an isometric view of the facility.

- **Operating Conditions:** The operational limits are summarized below, from [34]:
  - Maximum pressure $P_{\text{max}} = 25$ bar
  - Minimum pressure $P_{\text{min}} = 0.4$ bar
  - Maximum temperature $T_{\text{max}} = 350$ °C
  - Maximum mass flow $\dot{m}_{\text{max}} = 1.5$ kg/s
- **Working Fluids:** The facility is primarily designed for siloxane MM but can also operate with other fluids such as MDM, MD2M, D4, D5, D6, pentane, cyclopentane, NOVEC649, PP2, PP80, PP90, and toluene.
- **Test Sections:** The ORCHID features two interchangeable test sections:

  - **Supersonic/Transonic Vapor Tunnel:** This section features a supersonic nozzle with a throat area of 150 mm^2 and optical access for gas dynamic experiments.
  - **ORC Turbine Test Bed:** Designed for testing mini-ORC expanders with a fully instrumented 10 kWe machine, extendable to machines with up to 80 kWe power.
- **Measurement Techniques:**
  - Advanced laser diagnostic techniques like Particle Image Velocimetry (PIV).
  - Optical measurements like Schlieren imaging for visualizing flow characteristics.
  - Conventional measurements, including temperature, pressure, and mass flow rate.
- **Commissioning Results:**
  - Successfully tested with MM as the working fluid.
  - Achieved steady-state operation with key parameters such as mass flow rate, temperature, and pressure closely monitored and maintained.
  - The setup and experiments are designed to provide high-quality data with uncertainties typically lower than 0.6% for key process variables.

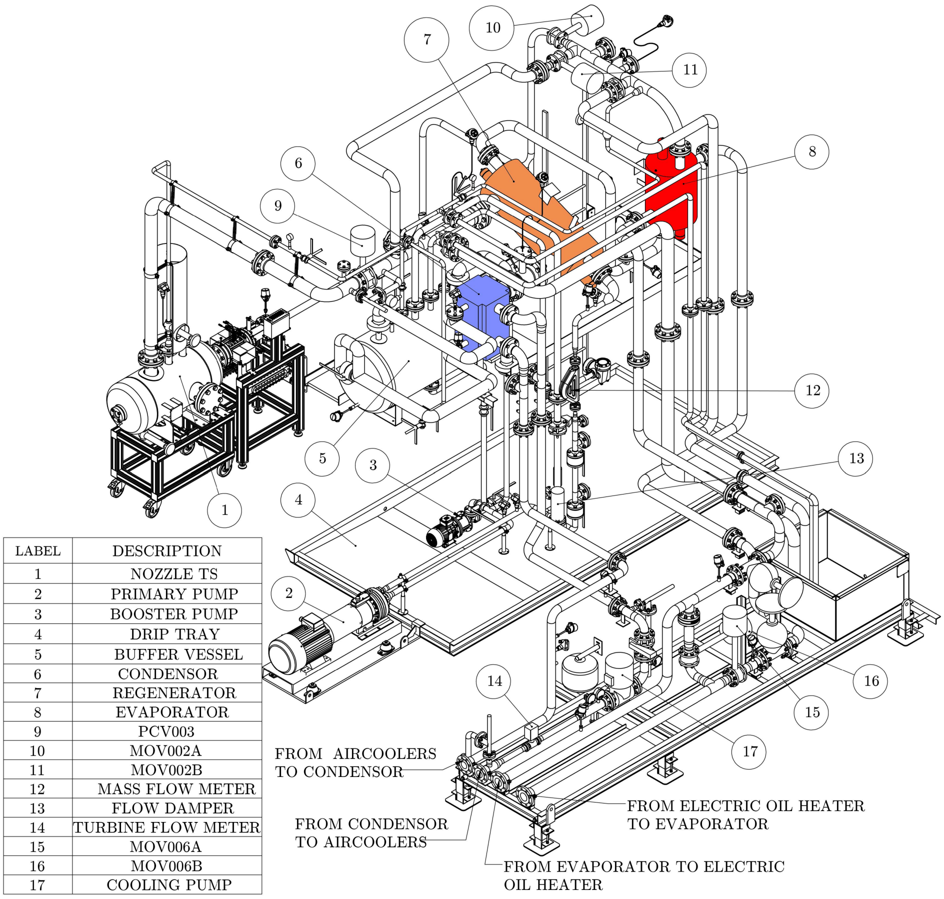

LABEL	DESCRIPTION
1	NOZZLE TS
2	PRIMARY PUMP
3	BOOSTER PUMP
4	DRIP TRAY
5	BUFFER VESSEL
6	CONDENSOR
7	REGENERATOR
8	EVAPORATOR
9	PCV003
10	MOV002A
11	MOV002B
12	MASS FLOW METER
13	FLOW DAMPER
14	TURBINE FLOW METER
15	MOV006A
16	MOV006B
17	COOLING PUMP

Figure 5.1: CAD isometric view of the ORCHID, highlighting all its main components. Reprinted from [34].

The ORCHID represents a significant advancement in the study of NICFD, providing essential data for validating and improving computational models used in various industrial applications involving non-ideal fluid dynamics.

5.2 Design Requirements

The first step in developing a new pump is to understand the current setup and the design requirements. There are currently two pumps installed:

- **Feed Pump:** Wanner Hydra-Cell G35, a positive displacement diaphragm pump.
- **Booster Pump:** ROTOS SDM 3x12, a single-stage magnetically driven centrifugal pump ensuring adequate suction head for the feed pump.

The operating conditions of each test section in the facility are the following:

Test Section	Inlet Temperature	Inlet Pressure	Mass Flow Rate
Supersonic Nozzle	T = 252 °C	P = 18.36 bara	1.15 kg/s
ORC Turbine	T = 275 °C	P = 20.8 bara	0.17 kg/s

Table 5.1: ORCHID test section properties

Since the facility has a wide pressure and mass-flow operational range, the newly designed pump should be able to accommodate this. The booster pump is kept in place to provide enough NPSH to prevent cavitation. The pump inlet pressure is taken as 5 bar, which is the target exit pressure of the turbine test section.

5.3 Pump Optimization

Now that the current set-up has been laid out, the inputs for the pump design optimization can be defined. The chosen fluid is MM (hexamethyldisiloxane), most commonly used in the ORCHID. An impeller and diffuser are modeled. Due to time and resource constraints, the volute and exit cone are not included. The working pressure, temperature, and mass flow are taken from the working specifications of the ORCHID [34]. The values of the design variables reporten in Table 5.2 are unimportant as they only serve as an initialization point for the optimization algorithm. Note that these input variables and the resulting design serve only as a demonstration of the ROM for preliminary design and should not be taken as final.

	Parameter	Symbol	Unit	ORCHID Pump
Basic Settings	Fluid	-	-	MM
	Equation of State	EoS	-	REFPROP
	Outlet Station	-	-	2
	Inlet Total Pressure	P_{t0}	bar	5
	Inlet Total temperature	T_{t0}	K	350
	Inlet Mass Flow	$\dot{m}$	kg/s	0.4
Design Variables	Total Pressure Rise	ΔP_t	bar	15
	Impeller Inlet Shape Factor	k_n	-	0.8775
	Total Number of Blades	N_{bl}	-	12
	Rotational Speed	RPM	rev/min	20000

Table 5.2: ORCHID Pump design parameters

The mass flow has been chosen as 0.4 kg/s as an intermediate point between the operating conditions of the supersonic nozzle and turbine test sections. The optimizer should be able to achieve a design that accommodates all operating conditions. Furthermore, the following optimization design variable bounds are imposed:

Constraint	Symbol	Unit	Bounds
Outlet Absolute Flow Angle	α_1	[deg]	[60, 90]
Work Coefficient	ψ	[-]	[0.4, 1.0]
Impeller Shape Factor	k_n	[-]	[0.65, 0.95]
Diffuser Radius Ratio	$\mathrm{DR}_{\mathrm{diff}}$	[-]	[1.01, 2]
Blade Number	N_{bl}	[-]	[6, 16]
Rotational Speed	RPM	[rev/min]	[50% $\mathrm{RPM}_{\mathrm{des}}$, 150% $\mathrm{RPM}_{\mathrm{des}}$]

Table 5.3: Optimization variable bounds

With,the following optimization constraints:

Constraint	Symbol	Unit	Value
Minimum Hub Radius	$\mathrm{R}_{1,\mathrm{hub,\,min}}$	[m]	2e-3
Minimum Allowable Mill Tip	$\mathrm{Mill}_{\mathrm{tip}}$	[-]	1e-3
Minimum Impeller Outlet Width	$\mathrm{H}_{1,\mathrm{min}}$	[m]	1e-3
Maximum Total Pressure Deviation	$\mathrm{P}_{t,\mathrm{err\,max}}$	[%]	10
Maximum Axial Thrust	$\mathrm{F}_{\mathrm{ax,\,max}}$	[N]	3000
Maximum Electric Power	$\mathrm{P}_{\mathrm{el,\,max}}$	[W]	7000
Maximum Shaft Torque	$\mathrm{T}_{\mathrm{max}}$	[Nm]	6

Table 5.4: Optimization variable constraints

5.3.1 Results

This section reports and discusses results from the optimization study. Below is a report detailing the progress of each generation in the optimization routine after the termination criteria were met.

n gen	n eval	n nds	cv min	cv avg	eps	indicator
1	60	1	nan	nan	-	-
2	120	1	nan	nan	-	-
3	180	1	0.0009491293	0.4274472363	-	-
4	240	1	0.000000E+00	0.2219974989	-	-
5	300	1	0.000000E+00	0.0822918547	2.9187500000	ideal
6	360	2	0.000000E+00	0.0340216481	1.0000000000	ideal
7	420	3	0.000000E+00	0.0162729380	0.2206564313	f
8	480	4	0.000000E+00	0.0043472473	0.5000000000	ideal
9	540	2	0.000000E+00	6.951353E-06	1.4298578366	nadir
10	600	2	0.000000E+00	0.000000E+00	0.0575037660	nadir
⋮	⋮	⋮	⋮	⋮	⋮	⋮
50	3000	17	0.000000E+00	0.000000E+00	0.0474710302	ideal

Table 5.5: Optimization Evaluation Metrics

Total Runtime: 4h 37min 54s (Intel i7 13th gen, 16 cores)

With each column:

- **n_gen**: Number of generations.
- **n_eval**: Number of cumulative function evaluations.
- **n_nds**: Number of non-dominated solutions (Number of solutions on the Pareto front)
- **cv_min**: Minimum constraint violation among all the solutions in the current population.
- **cv_avg**: Average constraint violation of the solutions in the current population.
- **eps**: Epsilon indicator. This is a measure of the convergence of the optimization process. A lower value indicates that the solutions are closer to the objective space.
- **indicator**: General indicator representing the type of solution. [12]

Objective Functions

As the optimization progresses, the value of objective functions is minimized (1 - $\overline{\eta_{tt}}$, 1 - $\overline{\text{OR}}$). This results in the maximization of the total to total efficiency and operating range, shown below. Each dot represents a function evaluation (pump design point).

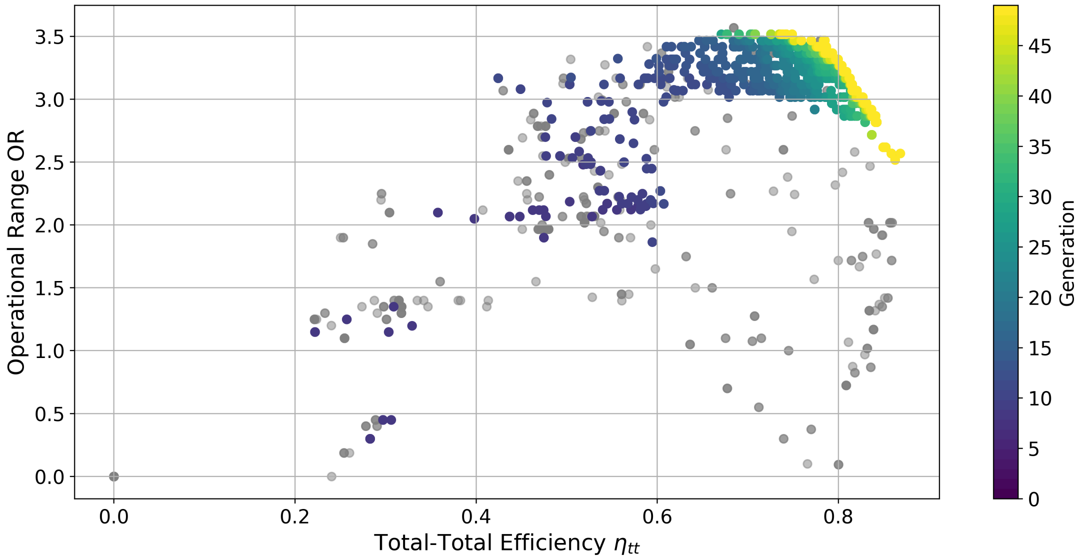

Figure 5.2: Optimization objective space. Grey dots represent designs that did not satisfy the constraints.

As the optimization algorithm generation increases, the design points trend towards the upper right of the objective space plot, indicating that the optimizer is successfully maximizing the objective variables. Zooming in to the top right of Figure 5.2, the Pareto front is clearer:

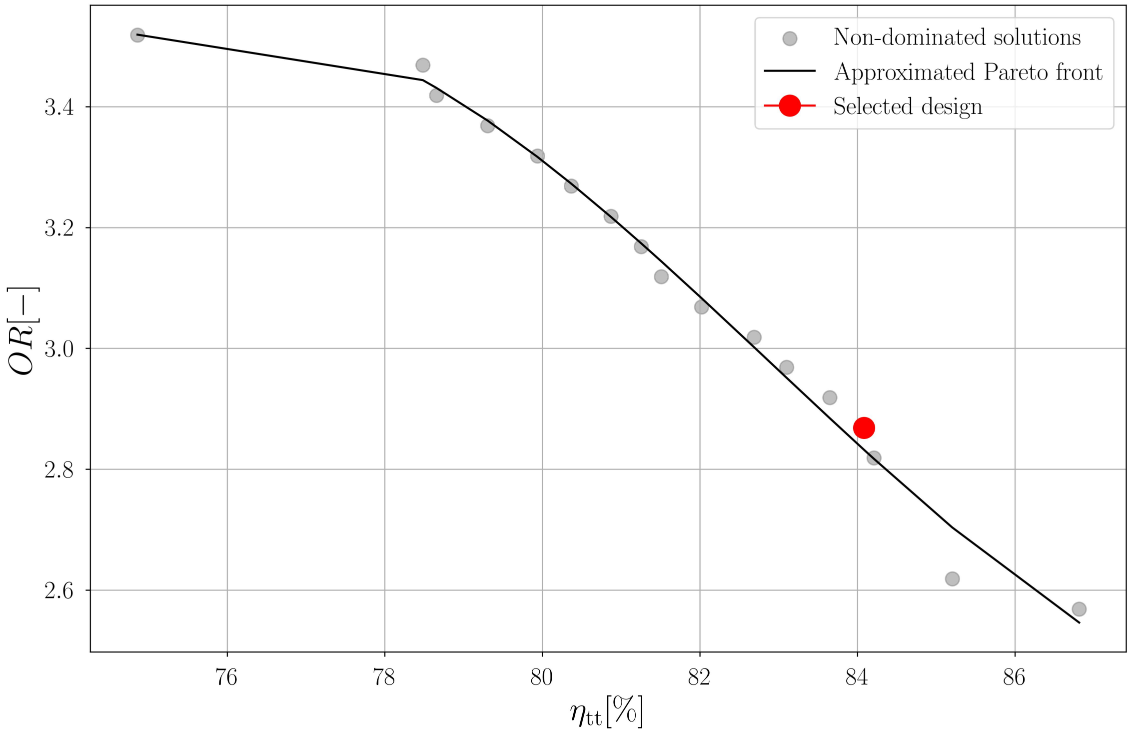

Figure 5.3: Pareto front on the objective space.

The non-determinate solutions reported by the optimizer are on the Pareto front. Depending on the application, choosing a design with a lower total to total average efficiency but a larger operating range may be more interesting. The user can select a point of interest and run the ROM in `analysis` mode to obtain detailed design parameters. Here, a design prioritizing a larger operational range over total efficiency was prioritized since ORCHID experiments may require a wide array of working conditions.

Furthermore, the objective values can be visualized over time, showing that the genetic algorithm learns to control the design variables as each generation progresses to increase the mean objective variables.

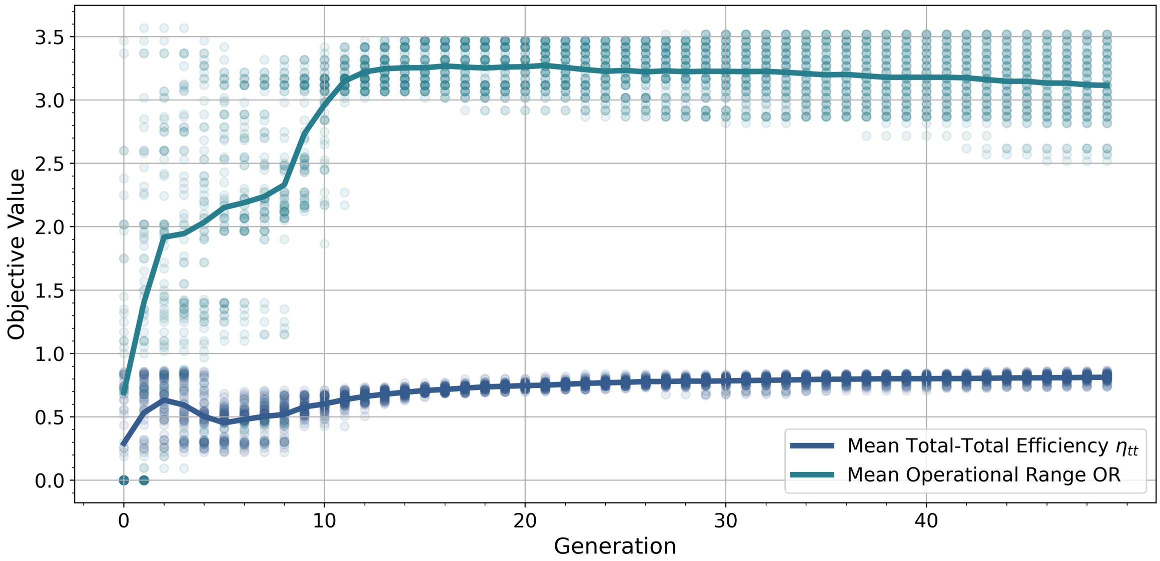

Figure 5.4: Evolution of objective function values

It is clear that both objective variable mean lines trend upward across generations, with the total-to-total efficiency approaching a value of 80% and the operational range exceeding a value of 3.

Design Variables

In Figure 5.5 below, the evolution of the design variables controlled by the optimization algorithm are shown across generations.

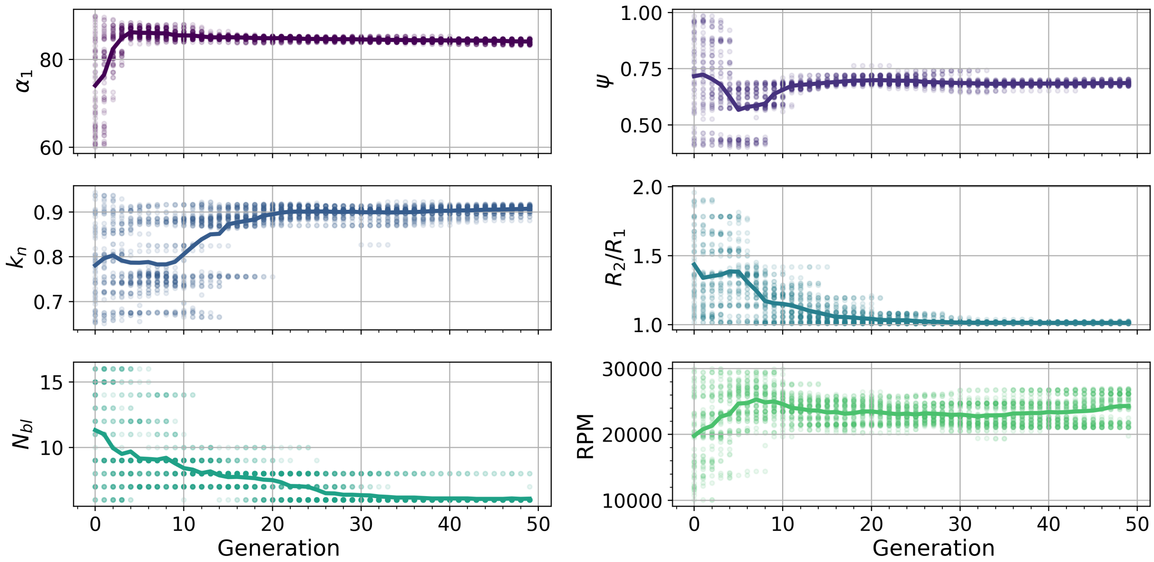

Figure 5.5: Evolution of design variables

Each variable departs from its initial value as the genetic algorithm explores the design space in search of the maximum objective values. In the very first generation, it begins to explore the limits of the design variables to understand their relationship and their influence on the objective functions and constraints. As the generations increase, the optimizer finds optimal values for each variable and slowly converges to them until the termination criteria are met.

Note that in this example, the number of blades has been set to 6, which is its minimum value. This probably does not affect the final head, as it can be compensated with a higher rpm, but it does decrease losses. Also, the diffuser length ratio converged to zero, which means the optimizer removed the diffuser. To simplify the following analysis, the diffuser is removed.

Constraints

A very important feature to observe from the optimization constraints is the constraint violation, represented as a value > 0. As the constraint value approaches zero, it becomes closer to its limiting value.

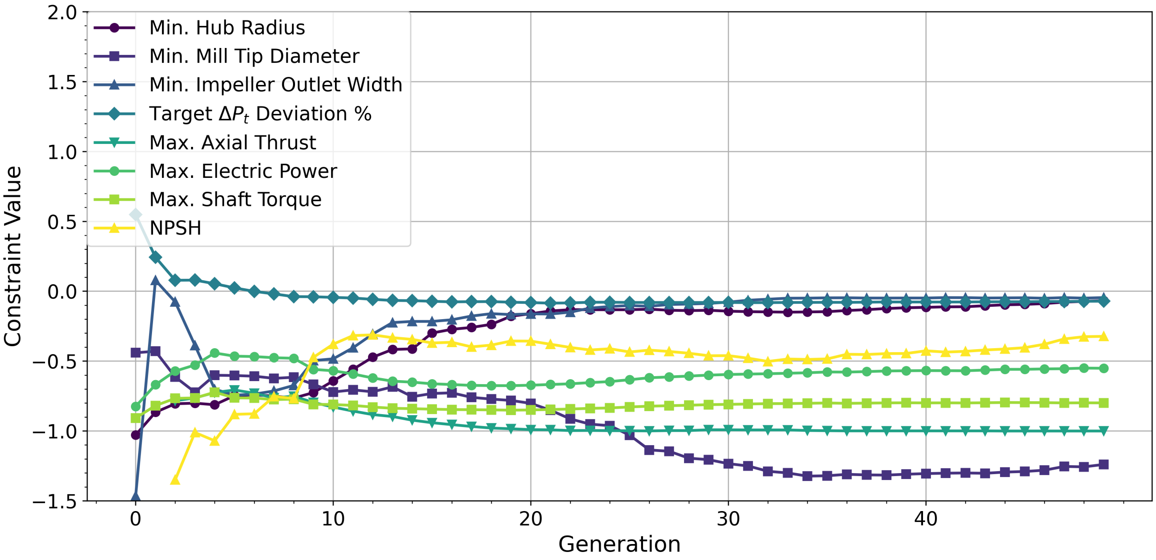

Figure 5.6: Optimization constraints over generations.

As seen above and in the metric evaluation table (Table 5.5), every constraint is satisfied. As the generations increase, the constraints change their value non-linearly. This results from the changes in design variables and their effects.

5.4 Final Design

The final design for the ORCHID main pump is presented in this section. After setting the requirements and running the optimization, the selected design parameters are input to the ROM in `analysis` mode to assess its performance. Furthermore, a CFD simulation is performed to compare and validate the results.

The design selected from the Pareto front has the following design variables:

Constraint	**Symbol**	**Unit**	**Value**
Outlet Absolute Flow Angle	α_1	[deg]	84.62
Work Coefficient	ψ	[-]	0.65
Impeller Shape Factor	k_n	[-]	0.92
Diffuser Radius Ratio	$\mathrm{DR}_{\mathrm{diff}}$	[-]	1.01
Main blade Number	N_{bl}	[-]	3
Splitter blade Number	N_{split}	[-]	3
Rotational Speed	RPM	[rev/min]	21752

Table 5.6: Optimized pump design variables

As the diffuser length is practically at its minimum value, it is omitted from the CFD simulations due to its added computational cost. This is because the objective function sought to obtain a target total pressure P_t. Since the diffuser does not add any work to the flow, it does not increase the total pressure (it actually decreases it due to friction losses). Another optimization with a *static* pressure target may have a different result.

5.4.1 Design Analysis

Using the CFD setup methodology from chapter 3, a mesh with 300k elements is used for a single passage. Below, the operational maps generated by TurboSim are superimposed onto the CFD results in Figure 5.7, and Figure 5.8. Only the relevant portion of the operating map (0.15-1.5 kg/s) was simulated.

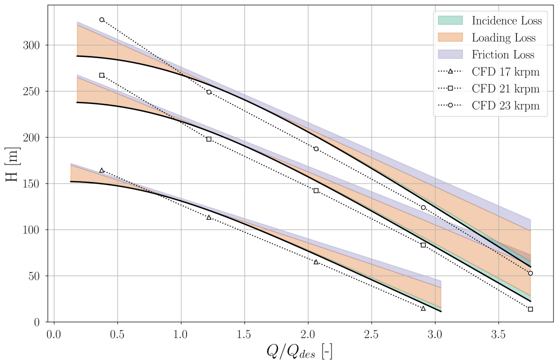

Figure 5.7: Head-Flow Curve for the ORCHID impeller.

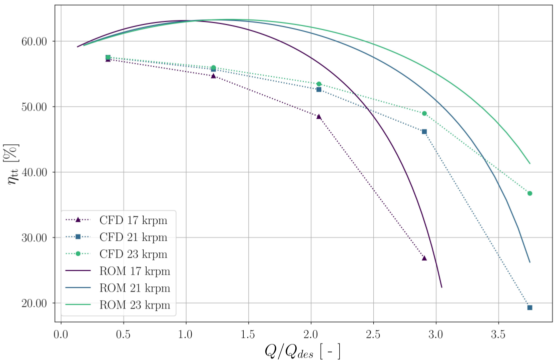

Figure 5.8: Total-Total efficiency for the ORCHID impeller.

The predicted head of Figure 5.7 agrees well with the CFD simulations, except at very low flow conditions, where the head is underestimated by the ROM. The predicted efficiency of Figure 5.8 shows a good agreement in the trends but overestimates the actual total-total internal efficiency. The cause for these discrepancies is not clear, as the source could stem from the loss modeling or the CFD setup.

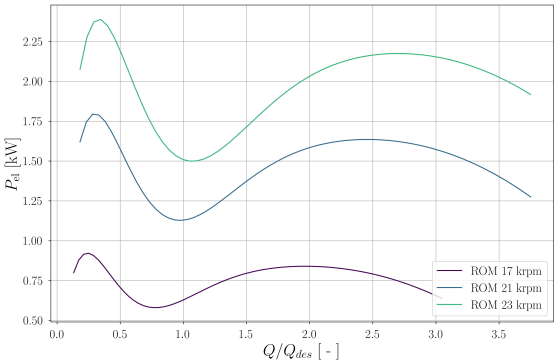

Figure 5.9: Power map for the ORCHID impeller.

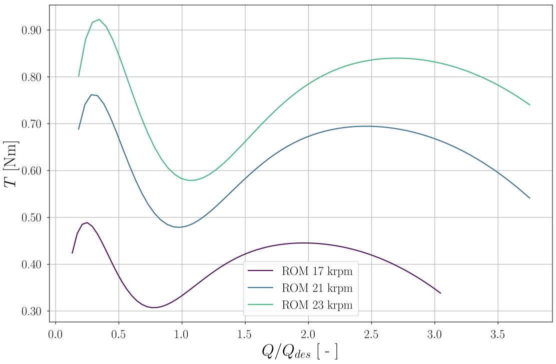

Figure 5.10: Shaft Torque map for the ORCHID impeller.

Both the power and torque curves seem to have a peculiar shape. However, they are a result of both the non-linear internal and external losses included in the model. As the flow rate deviates from the design condition, losses increase, and thus, the required power and torque increase.

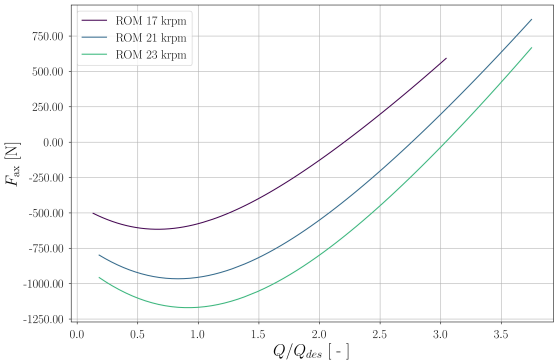

Figure 5.11: Axial force map for the ORCHID impeller.

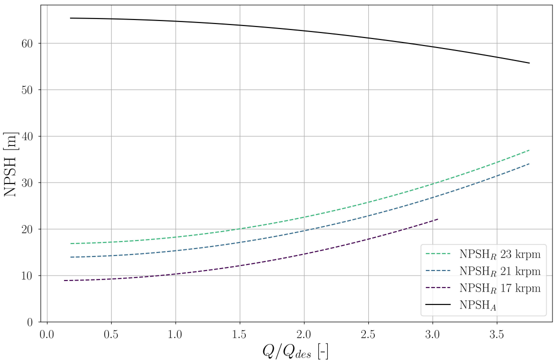

Figure 5.12: NPSH margin of the ORCHID impeller.

Finally, looking at the axial force plot, as the flow rate increases the axial force shifts from negative to positive (shaft in compression to tension, respectively). The axial force results from the pressure difference across the impeller face through clearance gaps, see Figure 3.12. At low flow rates, the head is high, and not much fluid leaks to the impeller's back face, leading to high compressive forces on the shaft. As the flow rate increases, the head drops, and more fluid leaks through the clearance gap, leading to tension in the shaft assembly. Looking at Figure 5.12, the pump has been designed to avoid cavitation throughout the whole operating range as seen from the NPSH_a and NPSH_r curves not crossing each other.

Power Consumption Comparison

A power consumption comparison between the currently installed reciprocating pump and the designed centrifugal pump is shown. According to the manufacturer, the Wanner Hydra-Cell G35 pump power curve is given by the following formula [37]:

$$P_{\mathrm{el}} = \frac{100 \cdot \mathrm{rpm}}{84428} + \frac{\mathrm{l/min} \cdot \mathrm{bar}}{511} [\mathrm{kW}] \tag{5.1}$$

Where the rpm is a function of the flow rate l/min (provided in the datasheet). In Figure 5.13 below, the power curves of both pumps can be compared.

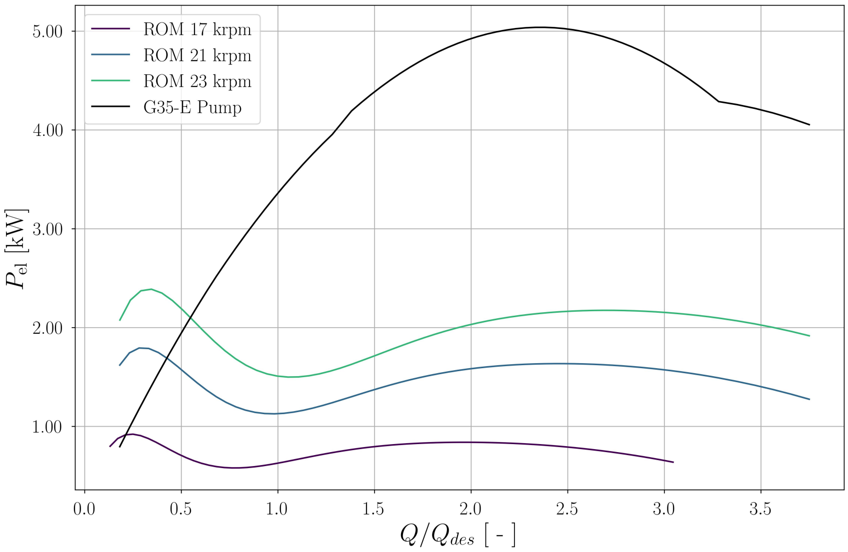

Figure 5.13: Expected power curves of the current G35-E pump and the proposed impeller.

The centrifugal pump decreases power consumption by 2kW (from 3.5kW to 1.5kW) at the design flow rate and maximum head compared to the G35 pump currently installed—a 60% reduction in power. Even with some uncertainty in the total efficiency provided by the ROM, it seems like adopting a centrifugal pump as a replacement for the reciprocating diaphragm pump would improve the power consumption of the ORCHID facility.

5.4.2 Summary

This section has defined an optimization problem using the ROM from this work to design an efficient and robust centrifugal pump impeller capable of replacing the current reciprocating diaphragm pump of the ORCHID facility.

The results show that it is possible to design an impeller with the operational requirements and constraints of the ORCHID, and doing so could result in a power reduction of around 60% at the best efficiency point.

Below is a CAD view of the final generated geometry (Generated with BladeGen from the ROM outputs).

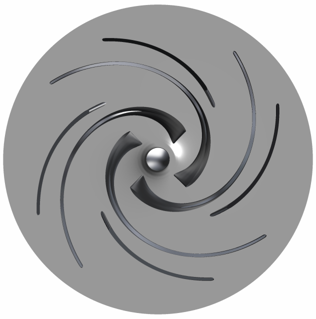

Figure 5.14: Top view of the ORCHID pump impeller (shroud removed).

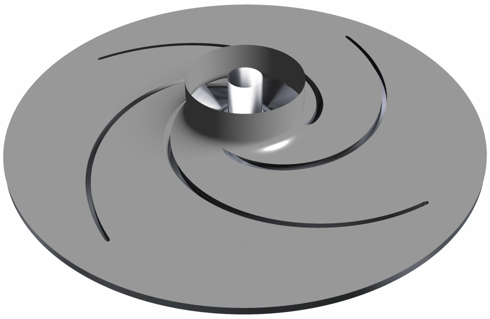

Figure 5.15: Isometric view of the ORCHID pump impeller.

Regarding the computational expense: This ORCHID impeller took less than 2 minutes to generate results for five speedlines. The batch of 15 CFD simulations to validate these results took about 2.5 hours of computation on a node from the `DelftBlue` HPC plus at least 30 minutes of set-up and meshing.

Finally, Appendix B contains the complete performance report generated by Turbosim Appendix B.

6

Conclusion

This work has reported the development and verification via CFD of a reduced-order model framework capable of designing and optimizing non-cavitating centrifugal pumps. This framework is highly valuable during component and system-wide preliminary design efforts. The user controls the design parameters and is also given automatic variable calculations. The design variables can be optimized for specific operating constraints through a genetic algorithm.

It is also found through a case study for the replacement of the current reciprocating diaphragm pump of the TU Delft ORCHID research facility with a centrifugal turbopump, the power consumption can be decreased by around 60%.

The developed program includes the following features:

- Pump modeling: Operational performance maps of various noncavitating pump components can be quickly analyzed: Impeller, Vaneless Diffuser, Volute, and Exit cone.
- Fluid Independence: Any fluid available through CoolProp or REFPROP is valid, allowing for the study of unconventional working fluids.
- Design Optimization: The analysis module is integrated into a genetic algorithm capable of generating efficient and robust pump designs for a given set of constraints.
- Verification: This work builds on the work of Giuffre' [29], which has been verified for centrifugal compressors. Furthermore, the implemented slip and loss models are validated in the literature. Finally, the complete implementation of this work has been verified with reasonable results (slightly underestimating head and efficiency) through a CFD study of two impellers.

6.1 Research Conclusion

The two main research objectives have been fulfilled:

Research objectives

- **To develop a preliminary design and optimization framework for non-cavitating turbopumps.**
- **To develop a centrifugal pump design to replace the TU Delft ORCHID main pump.**

Furthermore, the proposed research questions have been answered:

Research questions

- **To what degree can a reduced-order turbopump design model assess performance compared to CFD?**
  - This study has shown that reduced-order models can very much accelerate the design cycle of centrifugal pumps in the preliminary design phase by achieving high levels of fidelity (difference of less than 10% from RANS CFD) at a fraction of the computational cost (3h vs. 2 min).
- **What is the size and the efficiency of the ORCHID centrifugal pump?**
  - A proof of concept pump impeller was designed using a genetic algorithm to replace the current reciprocating feed pump at the ORCHID facility. Multiple suitable designs emerged from a Pareto front in the efficiency–operating range design space. One of such designs with an 84% total-to-total efficiency and an operating range of 2.9 was analyzed and showed satisfactory performance while reducing power consumption by 60% at the BEP compared to the current pump.

6.2 Limitations

- The assumption of no inlet prerotation may be misleading. As the flow entering the impeller eye is subsonic, the whirl imparted onto the flow due to the blade leading edge advects upstream. This has two effects:
  - Decreased efficiency: work is being done to the flow upstream.
  - Reduced flow incidence: As the incoming flow has a non-zero tangential velocity, the effective incidence on the blades is limited. Incidence losses are slightly decreased.
- The Effect of blade wrap angle is not captured, which has been seen to heavily influence the stability of the impeller and change the degree of blade loading, influencing losses.
- The CFD simulations use no-slip wall boundary conditions, meaning that the flow velocity is zero at the wall. While this is generally accurate, surface roughness has a strong effect on the development of boundary layers and could alter the loss mechanisms.
- This work has only verified the impeller model due to time and resource constraints. The other component models have been verified for centrifugal compressors, and it is expected that they do not need further changes. However, this should be verified.

6.3 Recommendations

- Further Verification: While the verification efforts of this work are reasonable, more can be done.
  - Internal Losses: More insight into the various loss mechanisms is required, as various validated loss models yield slightly different results. Loss model sets could be built for different centrifugal classes.
  - Clearance Losses: The clearance loss model was not verified, given the expensive simulations required. This should be done as unshrouded impellers are very common in small-scale applications.
  - External Losses: These have not been verified, as expensive simulations, including secondary flow paths and mechanical friction losses, are required.
- Cavitating regimes: This work has focused on non-cavitating regimes of pump operation. In practice, some cavitation may be allowable, but the modeling is computationally expensive. Research into how to model this efficiently and assess the impact on performance could be very valuable.
- Multistage Pumps: Multistage pumps are widely used in many industrial and aerospace applications. Axial inducers are also frequently used to raise the pressure ahead of a centrifugal pump. These would be very valuable additions to the ROM.
- Additional design variables: It was apparent that the impeller blade wrap angle played a big role in the convergence behavior of the CFD simulations. It is hypothesized that this also has a large impact on various loss mechanisms. The effect of other parameters such as the impeller height, meridional contour, surface roughness (perhaps as a function of material and manufacturing process), edge rounding, and splitter blade location could be very interesting.
- Data-Driven Models: if large datasets of high-fidelity data are generated, data-driven models could be trained on them to quickly produce novel designs or predict the performance of existing configurations.

References

[1] AC-9 Aircraft Environmental Systems Committee. *Thermodynamics of Incompressible and Compressible Fluid Flow*. Apr. 2019. DOI: `10.4271/AIR1168/1A`.

[2] Kara Omar Abdellah, Abdelkrim Khaldi, and Abdelkrim Ladouani. "Prediction of centrifugal pump performance using energy loss analysis". In: *Australian Journal of Mechanical Engineering* 15 (Nov. 2017), pp. 210–221. DOI: `10.1080/14484846.2016.1252567`.

[3] Alireza Ameli et al. "Centrifugal Compressor Design for Near-Critical Point Applications". en. In: *Journal of Engineering for Gas Turbines and Power* 141.3 (Mar. 2019), p. 031016. ISSN: 0742-4795, 1528-8919. DOI: `10.1115/1.4040691`. URL: `https://asmedigitalcollection.asme.org/gasturbinespower/article/doi/10.1115/1.4040691/366443/Centrifugal-Compressor-Design-for-NearCritical` (visited on 06/10/2024).

[4] *Ansys | Engineering Simulation Software*. en-US. URL: `https://www.ansys.com/` (visited on 05/12/2024).

[5] F. Ascione, P. Colonna, and C.M. De Servi. "Integrated design optimization method for novel vapour-compression-cycle-based environmental control systems". en. In: *Applied Thermal Engineering* 236 (Jan. 2024), p. 121261. ISSN: 13594311. DOI: `10.1016/j.applthermaleng.2023.121261`. URL: `https://linkinghub.elsevier.com/retrieve/pii/S1359431123012905` (visited on 11/17/2023).

[6] R. H. Aungier. "Mean Streamline Aerodynamic Performance Analysis of Centrifugal Compressors". In: *Journal of Turbomachinery* 117.3 (July 1995), pp. 360–366. ISSN: 0889-504X. DOI: `10.1115/1.2835669`.

[7] Ronald H Aungier. *Centrifugal compressors*. 2000.

[8] Theodor W. von Backström. "A Unified Correlation for Slip Factor in Centrifugal Impellers". In: *Journal of Turbomachinery* 128.1 (Aug. 2005), pp. 1–10. ISSN: 0889-504X. DOI: `10.1115/1.2101853`.

[9] S. Bahamonde et al. "Method for the Preliminary Fluid Dynamic Design of High-Temperature Mini-Organic Rankine Cycle Turbines". English. In: *Journal of Engineering for Gas Turbines and Power* 139.8 (2017). ISSN: 0742-4795. DOI: `10.1115/1.4035841`.

[10] Ian H. Bell et al. "Pure and Pseudo-pure Fluid Thermophysical Property Evaluation and the Open-Source Thermophysical Property Library CoolProp". In: *Industrial & Engineering Chemistry Research* 53.6 (2014), pp. 2498–2508. DOI: `10.1021/ie4033999`.

[11] Hao Bing et al. "Prediction method of impeller performance and analysis of loss mechanism for mixed-flow pump". en. In: *Science China Technological Sciences* 55.7 (July 2012), pp. 1988–1998. ISSN: 1674-7321, 1869-1900. DOI: `10.1007/s11431-012-4867-9`. URL: `http://link.springer.com/10.1007/s11431-012-4867-9` (visited on 02/14/2024).

[12] Julian Blank and Kalyanmoy Deb. "Pymoo: Multi-Objective Optimization in Python". In: *IEEE Access* 8 (2020), pp. 89497–89509. DOI: `10.1109/ACCESS.2020.2990567`.

[13] Christopher E. Brennen. *Hydrodynamics of Pumps*. en. 1st ed. Cambridge University Press, Mar. 2011. ISBN: 978-1-107-40149-5 978-1-107-00237-1 978-0-511-97672-8. DOI: `10.1017/CBO9780511976728`. URL: `https://www.cambridge.org/core/product/identifier/9780511976728/type/book` (visited on 12/15/2023).

[14] Weidong Cao et al. "Validation and simulation of cavitation flow in a centrifugal pump by filter-based turbulence model". en. In: *Engineering Applications of Computational Fluid Mechanics* 16.1 (Dec. 2022), pp. 1724–1738. ISSN: 1994-2060, 1997-003X. DOI: `10.1080/19942060.2022.2111363`. URL: `https://www.tandfonline.com/doi/full/10.1080/19942060.2022.2111363` (visited on 05/09/2024).

[15] *CFTURBO*. en. URL: `https://cfturbo.com/` (visited on 05/25/2024).

[16] Piero Colonna et al. "Organic Rankine Cycle Power Systems: From the Concept to Current Technology, Applications, and an Outlook to the Future". en. In: *Journal of Engineering for Gas Turbines and Power* 137.10 (Oct. 2015), p. 100801. ISSN: 0742-4795, 1528-8919. DOI: `10.1115/1.4029884`. URL: `https://asmedigitalcollection.asme.org/gasturbinespower/article/doi/10.1115/1.4029884/373802/Organic-Rankine-Cycle-Power-Systems-From-the` (visited on 09/09/2023).

[17] O Conrad, K Raif, and M Wessels. "The calculation of performance maps for centrifugal compressors with vane-island diffusers". In: *Performance prediction of centrifugal pumps and compressors* (1979), pp. 135–147.

[18] JE Coppage et al. *Study of supersonic radial compressors for refrigeration and pressurization systems*. Wright Air Development Center, 1956.

[19] Luca d'Agostino and Maria Vittoria Salvetti, eds. *Cavitation Instabilities and Rotordynamic Effects in Turbopumps and Hydroturbines: Turbopump and Inducer Cavitation, Experiments and Design*. en. Vol. 575. CISM International Centre for Mechanical Sciences. Cham: Springer International Publishing, 2017. ISBN: 978-3-319-49717-4 978-3-319-49719-8. DOI: `10.1007/978-3-319-49719-8`. URL: `http://link.springer.com/10.1007/978-3-319-49719-8` (visited on 10/18/2023).

[20] Luca d'Agostino et al., eds. *Fluid Dynamics of Cavitation and Cavitating Turbopumps*. Vol. 496. CISM International Centre for Mechanical Sciences. Vienna: Springer, 2007. ISBN: 978-3-211-76668-2 978-3-211-76669-9. DOI: `10.1007/978-3-211-76669-9`. URL: `http://link.springer.com/10.1007/978-3-211-76669-9` (visited on 10/11/2023).

[21] J. W. Daily and R. E. Nece. "Chamber Dimension Effects on Induced Flow and Frictional Resistance of Enclosed Rotating Disks". In: *Journal of Basic Engineering* 82.1 (Mar. 1960), pp. 217–230. ISSN: 0021-9223. DOI: `10.1115/1.3662532`. eprint: `https://asmedigitalcollection.asme.org/fluidsengineering/article-pdf/82/1/217/5519240/217\_1.pdf`.

[22] Amre Dardor. "Modelling the Slip Effect in High-Speed Centrifugal Compressors: A Comparison Between Reduced-Order Models and CFD". en. In: (2023). URL: `https://repository.tudelft.nl/islandora/object/uuid%3A926dddd3-6e1b-43d9-8f87-995132abd95f` (visited on 06/22/2024).

[23] K. Deb et al. "A fast and elitist multiobjective genetic algorithm: NSGA-II". In: *IEEE Transactions on Evolutionary Computation* 6.2 (2002), pp. 182–197. DOI: `10.1109/4235.996017`.

[24] *Die Kreiselpumpen*. en. URL: `https://link.springer.com/book/10.1007/978-3-662-43146-7` (visited on 05/10/2024).

[25] Sydney L. Dixon. *Fluid mechanics and thermodynamics of turbomachinery*. en. 4th ed., in SI/metric units. Boston, Mass. Oxford: Butterworth-Heinemann, 1998. ISBN: 978-0-7506-7059-3.

[26] Oleg Dubitsky and David Japikse. "Vaneless Diffuser Advanced Model". en. In: *Journal of Turbomachinery* 130.1 (Jan. 2008), p. 011020. ISSN: 0889-504X, 1528-8900. DOI: `10.1115/1.2372781`. URL: `https://asmedigitalcollection.asme.org/turbomachinery/article/doi/10.1115/1.2372781/462440/Vaneless-Diffuser-Advanced-Model` (visited on 06/10/2024).

[27] Michael R Galvas. *Fortran program for predicting off-design performance of centrifugal compressors*. Tech. rep. 1973.

[28] Andrea Giuffre, Piero Colonna, and Matteo Pini. "The Effect of Size and Working Fluid on the Multi-Objective Design of High-Speed Centrifugal Compressors". en. In: *International Journal of Refrigeration* 143 (Nov. 2022), pp. 43–56. ISSN: 01407007. DOI: `10.1016/j.ijrefrig.2022.06.023`. URL: `https://linkinghub.elsevier.com/retrieve/pii/S0140700722002092` (visited on 09/10/2023).

[29] A. Giuffré. "Integrated Design Optimization of Electrically-Driven Vapor Compression Cycle Systems for Aircraft". en. PhD thesis. [object Object], 2023. DOI: `10.4233/UUID:B4F6A4A4-2E48-4BBE-9093-3F1368282F63`. URL: `http://resolver.tudelft.nl/uuid:b4f6a4a4-2e48-4bbe-9093-3f1368282f63` (visited on 05/08/2024).

[30] Andrea Giuffre' et al. "Data-driven modeling of high-speed centrifugal compressors for aircraft Environmental Control Systems". In: *International Journal of Refrigeration* 151 (July 2023), pp. 354–369. ISSN: 0140-7007. DOI: `10.1016/j.ijrefrig.2023.03.019`. URL: `https://www.sciencedirect.com/science/article/pii/S0140700723000865` (visited on 05/09/2024).

[31] Jonathan Gloger. "Modeling Leakage Losses and Axial Thrust in Rocket Engine Turbopumps: Development of a numerical model". en. In: (2018). URL: `https://repository.tudelft.nl/islandora/object/uuid%3A5c56ae9c-96c5-4854-a16e-c13ffe749e02` (visited on 09/15/2023).

[32] Dimitri Goutaudier, Jüurg Schiffmann, and Fabio Nobile. "Parametric Reduced Order Model of a Gas Bearings Supported Rotor". In: *Journal of Engineering for Gas Turbines and Power* 146.1 (Oct. 2023), p. 011002. ISSN: 0742-4795. DOI: `10.1115/1.4063424`. eprint: `https://asmedigitalcollection.asme.org/gasturbinespower/article-pdf/146/1/011002/7055501/gtp\_146\_01\_011002.pdf`.

[33] Johann Friedrich Gülich. *Centrifugal Pumps*. en. URL: `https://link.springer.com/book/10.1007/978-3-030-14788-4` (visited on 05/09/2024).

[34] A.J. Head. "Novel Experiments for the Investigation of Non-Ideal Compressible Fluid Dynamics: The ORCHID and First Results of Optical Measurements". en. PhD thesis. Delft University of Technology, 2021. DOI: `10.4233/UUID:A3B03976-2DF6-435C-B7DF-1505718FCD3A`. URL: `http://resolver.tudelft.nl/uuid:a3b03976-2df6-435c-b7df-1505718fcd3a` (visited on 05/30/2024).

[35] Y G Heng et al. "Experimental Study and Theoretical Analysis of the Rotating Stall in a Vaneless Diffuser of Radial Flow Pump". en. In: *IOP Conference Series: Earth and Environmental Science* 49 (Nov. 2016), p. 032006. ISSN: 1755-1307, 1755-1315. DOI: `10.1088/1755-1315/49/3/032006`. URL: `https://iopscience.iop.org/article/10.1088/1755-1315/49/3/032006` (visited on 05/22/2024).

[36] Hooshang Heshmat et al. “Oil-Free Turbocharger Demonstration Paves Way to Gas Turbine Engine Applications”. en. In: American Society of Mechanical Engineers Digital Collection, Aug. 2014. DOI: `10.1115/2000-GT-0620`. URL: `https://dx.doi.org/10.1115/2000-GT-0620` (visited on 06/24/2024).

[37] Hydra-Cell. *Hydra-Cell G35 Datasheet*. 2023. URL: `https://www.hydra-cell.co.uk/docs//Sales-Lit-Extranet-Datasheets/G35-Datasheet-11-01-23.pdf`.

[38] Christian Brix Jacobsen. *The Centrifugal Pump*. Provided as a Public Resource by Langley Well Pump Resource Library. URL: `www.grundfos.com`.

[39] W Jansen. “A Method for Calculating the Flow in a Centrifugal Compressor When Entropy Gradient Are Present”. In: *Royal society conference on internal aerodynamics*. 1967.

[40] W. JANSEN. “A method for calculating the flow in a centrifugal impeller when entropy gradient are present”. In: *Inst. Mech. Eng. Internal Aerodynamics* (1970). URL: `https://cir.nii.ac.jp/crid/1571135650145571968`.

[41] David Japikse. “Advanced diffusion levels in turbocharger compressors and component matching”. In: (1982).

[42] A. Javed, R. Pecnik, and J. P. Van Buijtenen. “Optimization of a Centrifugal Compressor Impeller for Robustness to Manufacturing Uncertainties”. en. In: *Journal of Engineering for Gas Turbines and Power* 138.11 (Nov. 2016), p. 112101. ISSN: 0742-4795, 1528-8919. DOI: `10.1115/1.4033185`. URL: `https://asmedigitalcollection.asme.org/gasturbinespower/article/doi/10.1115/1.4033185/372158/Optimization-of-a-Centrifugal-Compressor-Impeller` (visited on 10/18/2023).

[43] J. P. Johnston and Jr. Dean R. C. “Losses in Vaneless Diffusers of Centrifugal Compressors and Pumps: Analysis, Experiment, and Design”. In: *Journal of Engineering for Power* 88.1 (Jan. 1966), pp. 49–60. ISSN: 0022-0825. DOI: `10.1115/1.3678477`. eprint: `https://asmedigitalcollection.asme.org/gasturbinespower/article-pdf/88/1/49/5667438/49\_1.pdf`.

[44] Patrik Kovář et al. “Searching for the Most Suitable Loss Model Set for Subsonic Centrifugal Compressors Using an Improved Method for Off-Design Performance Prediction”. en. In: *Energies* 14.24 (Jan. 2021), p. 8545. ISSN: 1996-1073. DOI: `10.3390/en14248545`. URL: `https://www.mdpi.com/1996-1073/14/24/8545` (visited on 10/12/2023).

[45] Dabo Krempus, Fabio Beltrame, and Matteo Majer. “ORC Waste Heat Recovery System for the Turboshaft Engines of Turboelectric Aircraft”. en. In: ().

[46] E. W. Lemmon et al. *NIST Standard Reference Database 23: Reference Fluid Thermodynamic and Transport Properties-REFPROP, Version 10.0, National Institute of Standards and Technology*. 2018. DOI: `https://doi.org/10.18434/T4/1502528`. URL: `https://www.nist.gov/srd/refprop`.

[47] Eric W. Lemmon and Reiner Tillner-Roth. “A Helmholtz energy equation of state for calculating the thermodynamic properties of fluid mixtures”. In: *Fluid Phase Equilibria* 165.1 (Nov. 1999), pp. 1–21. ISSN: 0378-3812. DOI: `10.1016/S0378-3812(99)00262-9`. URL: `https://www.sciencedirect.com/science/article/pii/S0378381299002629` (visited on 06/04/2024).

[48] C. Lettieri et al. “Characterization of Cavitation Instabilities in a Four-Bladed Turbopump Inducer”. en. In: *Journal of Propulsion and Power* 34.2 (Mar. 2018), pp. 510–520. ISSN: 0748-4658, 1533-3876. DOI: `10.2514/1.B36317`. URL: `https://arc.aiaa.org/doi/10.2514/1.B36317` (visited on 09/15/2023).

[49] Hao Li, Yaping Ju, and Chuhua Zhang. “Optimization of supercritical carbon dioxide recompression Brayton cycle considering anti-condensation design of centrifugal compressor”. en. In: *Energy Conversion and Management* 254 (Feb. 2022), p. 115207. ISSN: 01968904. DOI: `10.1016/j.enconman.2022.115207`. URL: `https://linkinghub.elsevier.com/retrieve/pii/S0196890422000036` (visited on 02/11/2024).

[50] Ming Liu, Lei Tan, and Shuliang Cao. “Theoretical model of energy performance prediction and BEP determination for centrifugal pump as turbine”. en. In: *Energy* 172 (Apr. 2019), pp. 712–732. ISSN: 03605442. DOI: `10.1016/j.energy.2019.01.162`. URL: `https://linkinghub.elsevier.com/retrieve/pii/S0360544219301781` (visited on 02/11/2024).

[51] Soheyl Massoudi, Cyril Picard, and Jürg Schiffmann. “Robust design using multiobjective optimisation and artificial neural networks with application to a heat pump radial compressor”. en. In: *Design Science* 8 (2022), e1. ISSN: 2053-4701. DOI: `10.1017/dsj.2021.25`. URL: `https://www.cambridge.org/core/product/identifier/S2053470121000251/type/journal_article` (visited on 10/09/2023).

[52] J. Matley. *Progress in Pumps*. McGraw-Hill Information Services Company, 1989. ISBN: 978-0-07-040933-0. URL: `https://books.google.nl/books?id=wO9SAAAAMAAJ`.

[53] M. Mohr. *A Design Procedure for Low and High Head Inducers*. Technische Universität Kaiserslautern, 2020. URL: `https://books.google.nl/books?id=wTF0OAEACAAJ`.

[54] “Data-Driven Pre-Design Tool for Small Scale Centrifugal Compressors in Refrigeration”. In: *Proceedings of ASME Turbo Expo 2018* (2018). Ed. by Violette Mounier, Cyril Picard, and Jurg Schiffmann. Meeting Name: ASME Turbo Expo 2018: Turbomachinery Technical Conference and Exposition Num Pages: 10. DOI: `10.1115/GT2018-76349`.

[55] Mohammed Ahmed El-Naggar. “A One-Dimensional Flow Analysis for the Prediction of Centrifugal Pump Performance Characteristics”. en. In: *International Journal of Rotating Machinery* 2013 (2013), pp. 1–19. ISSN: 1023-621X, 1542-3034. DOI: `10.1155/2013/473512`. URL: `http://www.hindawi.com/journals/ijrm/2013/473512/` (visited on 02/11/2024).

[56] H W Oh, E S Yoon, and M K Chung. “An optimum set of loss models for performance prediction of centrifugal compressors”. In: *Proceedings of the Institution of Mechanical Engineers, Part A: Journal of Power and Energy* 211.4 (June 1997). Publisher: IMECHE, pp. 331–338. ISSN: 0957-6509. DOI: `10.1243/0957650971537231`. URL: `https://doi.org/10.1243/0957650971537231` (visited on 02/21/2024).

[57] L. E. Olmedo and J. Schiffmann. “Towards a real-time capable hybrid-twin for gas-bearing supported high-speed turbocompressors”. In: *Energy* 275 (2023), p. 127385. ISSN: 0360-5442. DOI: `https://doi.org/10.1016/j.energy.2023.127385`. URL: `https://www.sciencedirect.com/science/article/pii/S036054422300779X`.

[58] I.S. Pearsall. In: *Cavitation* (1972). URL: `https://www.scopus.com/inward/record.uri?eid=2-s2.0-0003723712&partnerID=40&md5=67c4953684d521a7453e3a77239e3906`.

[59] W.W. Peng. *Fundamentals of Turbomachinery*. Wiley, 2007. ISBN: 978-0-470-12422-2. URL: `https://books.google.nl/books?id=PEV357OXWR0C`.

[60] Carl Pfleiderer. *Strömungsmaschinen*. Springer-Verlag, 2013.

[61] European Association for Pump Manufacturers. *Net Positive Suction Head for Rotodynamic Pumps: A Reference Guide*. The Europump Guides to Advanced Pumping Technology. Elsevier Science, 1999. ISBN: 9781856173575. URL: `https://books.google.es/books?id=7zEh1bs_Mm4C`.

[62] Xuwen Qiu et al. “Analysis and Validation of a Unified Slip Factor Model for Impellers at Design and Off-Design Conditions”. In: *Journal of Turbomachinery* 133.041018 (Apr. 2011). ISSN: 0889-504X. DOI: `10.1115/1.4003022`. URL: `https://doi.org/10.1115/1.4003022` (visited on 06/09/2024).

[63] Hayder Kareem Sakran et al. “Effects of Blade Number on the Centrifugal Pump Performance: A Review”. en. In: *Arabian Journal for Science and Engineering* 47.7 (July 2022), pp. 7945–7961. ISSN: 2193-567X, 2191-4281. DOI: `10.1007/s13369-021-06545-z`. URL: `https://link.springer.com/10.1007/s13369-021-06545-z` (visited on 05/10/2024).

[64] J. Schiffmann and D. Favrat. “Experimental investigation of a direct driven radial compressor for domestic heat pumps”. en. In: *International Journal of Refrigeration* 32.8 (Dec. 2009), pp. 1918–1928. ISSN: 01407007. DOI: `10.1016/j.ijrefrig.2009.07.006`. URL: `https://linkinghub.elsevier.com/retrieve/pii/S0140700709001686` (visited on 10/11/2023).

[65] Hermann Schlichting and Klaus Gersten. *Boundary-layer theory*. springer, 2016.

[66] D Serrano et al. “Improving train energy efficiency by Organic Rankine Cycle (ORC) for recovering waste heat from exhaust gas”. In: *Proceedings of the 3rd International Seminar on ORC Power Systems, Brussels, Belgium*. 2015, pp. 12–14.

[67] Gino Sovran. “Experimentally determined optimum geometries for rectilinear diffusers with rectangular, conical or annular cross section”. In: *Fluid mechanics of internal flow* (1967), pp. 270–319.

[68] John D Stanitz. *One-dimensional compressible flow in vaneless diffusers of radial-and mixed-flow centrifugal compressors, including effects of friction, heat transfer and area change*. Tech. rep. 1952.

[69] A.J. Stepanoff. *Centrifugal and Axial Flow Pumps: Theory, Design, and Application*. Wiley, 1957. ISBN: 9780471821373. URL: `https://books.google.es/books?id=VPlSAAAAMAAJ`.

[70] Ulrik Ullum et al. “Prediction of rotating stall within an impeller of a centrifugal pump based on spectral analysis of pressure and velocity data”. en. In: *Journal of Physics: Conference Series* 52 (Nov. 2006), pp. 36–45. ISSN: 1742-6588, 1742-6596. DOI: `10.1088/1742-6596/52/1/004`. URL: `https://iopscience.iop.org/article/10.1088/1742-6596/52/1/004` (visited on 05/22/2024).

[71] Rene Van den Braembussche. *Design and Analysis of Centrifugal Compressors*. ASME Press, Jan. 2020. ISBN: 9781119424093. DOI: `10.1115/1.861VAN`.

[72] Adam Vermes and Claudio Lettieri. “Source Term Based Modeling of Rotating Cavitation in Turbopumps”. In: *Journal of Engineering for Gas Turbines and Power-transactions of The Asme* 141.6 (Aug. 2018). MAG ID: 2889013681, p. 061002. DOI: `10.1115/1.4042302`.

[73] -G. Li W. “Validating full cavitation model with an experimental centrifugal pump”. en. In: *TASK Quarterly. Scientific Bulletin of Academic Computer Centre in Gdansk* 18.1 (2014), pp. 81–100. ISSN: 1428-6394. URL: `https://bibliotekanauki.pl/articles/1954444` (visited on 05/09/2024).

[74] F. J. Wiesner. “A Review of Slip Factors for Centrifugal Impellers”. In: *Journal of Engineering for Power* 89.4 (Oct. 1967), pp. 558–566. ISSN: 0022-0825. DOI: `10.1115/1.3616734`. eprint: `https://asmedigitalcollection.asme.org/gasturbinespower/article-pdf/89/4/558/5718043/558\_1.pdf`.

[75] F.J. Wiesner. “A review of slip factors for centrifugal impellers”. In: *Journal of Engineering for Gas Turbines and Power* 89.4 (1967), pp. 558–566. DOI: `10.1115/1.3616734`.

[76] “The influence of splitter blades and meridional profiles on the performance of small-scale turbopumps for ORC applications; analysis, neural network modeling and optimization”. In: *Thermal Science and Engineering Progress* (2023). Ed. by Sajjad Zakeralhoseini and Jürg Schiffmann. DOI: `10.1016/j.tsep.2023.101734`.

[77] “Analysis and modeling of the tip leakage flow on the performance of small-scale turbopumps for ORC applications”. In: *Applied Thermal Engineering* (2022). Ed. by Sajjad Zakeralhoseini and Jürg Alexander Schiffmann. DOI: `10.1016/j.applthermaleng.2022.119160`.

[78] “Design, computational and experimental investigation of a small-scale turbopump for organic Rankine cycle systems”. In: *Energy Conversion and Management* (2023). Ed. by Sajjad Zakeralhoseini and Jürg Alexander Schiffmann. DOI: `10.1016/j.enconman.2023.117073`.

[79] Chaowei Zhang et al. “A method to select loss correlations for centrifugal compressor performance prediction”. en. In: *Aerospace Science and Technology* 93 (Oct. 2019), p. 105335. ISSN: 12709638. DOI: `10.1016/j.ast.2019.105335`. URL: `https://linkinghub.elsevier.com/retrieve/pii/S1270963819313616` (visited on 06/06/2024).

[80] Chaowei Zhang et al. “Improved slip factor model for centrifugal compressor”. In: *Hangkong Dongli Xuebao/Journal of Aerospace Power* 33.9 (2018), pp. 2178–2187. DOI: `10.13224/j.cnki.jasp.2018.09.015`.

[81] Christof Zwyssig, Johann W. Kolar, and Simon D. Round. “Megaspeed Drive Systems: Pushing Beyond 1 Million r/min”. In: *IEEE/ASME Transactions on Mechatronics* 14.5 (2009), pp. 564–574. DOI: `10.1109/TMECH.2008.2009310`.

A

Friction Factor Estimation

Skin friction losses comprise a large share of the total losses in centrifugal pumps. This kind of loss is very sensitive to the friction factor C_f. Finding a good estimate during pre-design is non-trivial, especially for low-specific-speed impellers with large blade curvatures or for unconventional working fluids, which might exhibit changes in viscosity and density.

In a study by Ameli et al. [3], various friction factor correlations were compared against a URANS CFD study for a centrifugal compressor working near the fluid's critical point. It concluded that the weighted average model by Aungier was most accurate in estimating the friction factor C_f [7], [40].

Beginning with a simple pipe flow model developed by Jansen [40], the friction factor can be very simply expressed as:

$$C_f = 0.0412 \cdot Re^{-0.1925} \tag{A.1}$$

$$Re = \frac{\bar{\rho} \cdot \bar{W} \cdot d_1}{\bar{\mu}} \tag{A.2}$$

However, it has been shown that this simple model may not apply well to impellers, as the flow path–and thus the development of the boundary layer–is very different from that of a pipe. Another approach for flows of $Re > 2000$ was proposed by Schlichting [65], based on the Colebrook-White correlation [1]:

$$\frac{1}{\sqrt{4 \cdot C_{f_r}}} = -2 \log \left[\frac{e}{3.71 \cdot D_{\text{hyd}}} \right] \tag{A.3}$$

$$\frac{1}{\sqrt{4 \cdot C_{f_s}}} = -2 \log \left[\frac{2.51}{\text{Re}\sqrt{4 \cdot C_{f_s}}} \right] \tag{A.4}$$

Where e is the peak-to-valley surface roughness ratio based on the material and surface finish. Skin friction factors for fully smooth C_{f_s} and fully rough C_{f_r} surfaces are shown by Equation A.4 and Equation A.3 respectively. Note that Equation A.4 must be solved iteratively. An initial guess value of $C_{f_s} = 0.006$ is used, as proposed by Jansen [40].

Since the operating conditions of centrifugal pumps can be very broad, the friction factor should account for both laminar and turbulent flows within the impeller. The weighted-average model proposed by Aungier [7] accounts for this:

$$C_f = C_{f_s} + (C_{f_r} - C_{f_s}) \cdot \left(1 - \frac{60}{(\mathrm{Re} - 2000)} \cdot \frac{e}{D_{hyd}}\right) \tag{A.5}$$

The hydraulic diameter D_{hyd} can be assumed as the passage width for a simple annular passage. However, to provide a more accurate representation (and the Reynolds number with Equation A.2), the equation proposed by Jansen [40] is used in this work:

$$D_{\mathrm{hyd}} = d_1 \cdot \left[\frac{\cos\beta_1}{\left(\frac{N_{bl}}{\pi} + \frac{d_1 \cdot \cos\beta_1}{H_1}\right)} + \frac{0.5 \cdot \left(\frac{d_{0,s}+d_{0,h}}{d_1}\right) \cdot \left(\frac{\cos\beta_{0,s}+\cos\beta_{0,h}}{2}\right)}{\frac{N_{bl}}{\pi} + \left(\frac{d_{0,s}+d_{0,h}}{d_{0,s}-d_{0,h}}\right) \cdot \left(\frac{\cos\beta_{0,s}+\cos\beta_{0,h}}{2}\right)} \right] \tag{A.6}$$

Lastly, a different friction factor is used for the vaneless diffuser. From the model developed by Stanitz [68], a two-dimensional system of equations (Equation 3.116) is solved to model the flow within the vaneless diffuser. The average value of the friction factor is estimated using the empirical correlation for diffusers by Japikse [26]:

$$C_f = k \cdot \left(\frac{1.8 \times 10^5}{\mathrm{Re}}\right)^{0.2} \tag{A.7}$$

With $k = 0.010$ as the value best matching with experimental data.

B

ORCHID Impeller Design Report

```
********************************************************************************************
******************** TurboSim - Integrated Turbomachinery Design Suite ********************
********************************************************************************************

************************************ GENERAL INFORMATION ***********************************
Turbomachinery Type: Centrifugal Pump
Fluid                 : MM
gas constant  [J/kg.K]:      51.20    molecular complexity  :      78.35
omega            [rpm]:      21752
mass flow rate  [kg/s]:     0.4000    upper point     [kg/s]:     1.5000
V flow rate 0   [m3/s]:      0.001    V flow rate 1   [m3/s]:      0.001
Tt                    :    350.000    Pt                    : 500000.000
flow coefficient      :      0.001    work coefficient      :      0.782
reaction degree       :      0.609
Ns                    :      0.229    Ds                    :      7.850
Beta ts               :      2.988    Beta tt               :      4.000
Eta ts          [pct.]:      52.20    Eta tt          [pct.]:      78.72
Eta tt average  [pct.]:      55.92    Eta tt internal [pct.]:      97.31
Specific work  [kJ/kg]:      2.185

****************************** LOSS BREAKDOWN AT DESIGN POINT *****************************
Delta eta incidence      [pct.]:       0.53
Delta eta loading        [pct.]:       0.92
Delta eta friction       [pct.]:       1.77
Delta eta separation     [pct.]:       0.01
Delta eta clearance      [pct.]:       0.23
Delta eta mixing         [pct.]:       1.22
Delta eta disk friction  [pct.]:       9.51
Delta eta recirculation  [pct.]:       7.47
Delta eta leakage        [pct.]:       4.78

************************************** STAGE GEOMETRY **************************************
N blades                     :          3
N splitter blades            :          3
```

```
impeller shape factor        :      0.913
diffuser radius ratio        :      1.010
R0                       [mm]:       4.75
R1                       [mm]:      25.45
R2                       [mm]:      25.71
H0                       [mm]:       5.18
H1                       [mm]:       1.00
R0 hub                   [mm]:       2.16
R0 shroud                [mm]:       7.34
R shaft                  [mm]:       1.95
R0 shroud / R1               :      0.288
H1 / R1                      :     0.0393
Lax / R1                     :       0.22
tip gap / H1                 :      0.010
peak-to-valley roughness [mm]:       0.14
LE thickness hub         [mm]:       1.00
LE thickness shroud      [mm]:       1.00
TE thickness hub         [mm]:       0.50
TE thickness shroud      [mm]:       0.50
blade angle 0 hub       [deg]:     -43.07
blade angle 0 mid       [deg]:     -65.77
blade angle 0 shroud    [deg]:     -73.95
blade angle 1           [deg]:     -67.91

******************************** FLOW PROPERTIES AT MIDSPAN ********************************
Thermodynamic properties
P0     [kPa]:    495.242    P1     [kPa]:   1493.891
Pt0    [kPa]:    500.000    Pt1    [kPa]:   2000.000
h0   [kJ/kg]:    -48.953    h1   [kJ/kg]:    -47.477
ht0  [kJ/kg]:    -48.946    ht1  [kJ/kg]:    -46.761
s0  [J/kg.K]:    -136.89    s1  [J/kg.K]:    -136.73
T0       [K]:     350.00    T1       [K]:     350.42
Tt0      [K]:     350.00    Tt1      [K]:     350.61
D0   [kg/m3]:     703.84    D1   [kg/m3]:     705.81
Cp0 [J/kg.K]:    2041.89    Cp1 [J/kg.K]:    2038.92
gamma0      :      1.221    gamma1      :      1.219
gamma Pv0   :    700.544    gamma Pv1   :    240.257
Z0          :      0.039    Z1          :      0.118
Gamma0      :      6.594    Gamma1      :      6.513

Velocity triangles
V0     [m/s]:       3.68    V1     [m/s]:      37.86
W0     [m/s]:      11.43    W1     [m/s]:      20.60
U0     [m/s]:      10.82    U1     [m/s]:      57.98
alpha0 [deg]:       0.00    alpha1 [deg]:      84.63
beta0  [deg]:     -71.23    beta1  [deg]:     -80.09

********************************* FLOW PROPERTIES AT INLET *********************************
U0 hub    [m/s]:       4.93    U0 mid    [m/s]:      10.82    U0 tip    [m/s]:      16.72
```

```
beta0 hub [deg]:     -53.26    beta0 mid [deg]:     -71.23    beta0 tip [deg]:     -77.60
inc hub   [deg]:      10.19    inc mid   [deg]:       5.46    inc tip   [deg]:       3.64

*********************************** ANCILLARY QUANTITIES ***********************************
slip angle        [deg]:      11.68
Cp diffuser            :      0.050
Hydraulic diameter [mm]:       2.76
Hydraulic length   [mm]:      45.78
Reynolds impeller      :     498898

************************************* OPERATING RANGE **************************************
OR:      3.700   at       17402 rpm
OR:      3.569   at       21752 rpm
OR:      3.281   at       23927 rpm

*********************************** MECHANICAL ANALYSIS ************************************
max(Power) [W]:      881.9    max(Torque) [Nm]:      0.489    max(Axial thrust) [N]:      615.2
max(Centrifugal stress) [MPa]:        0.3   at       17402 rpm

max(Power) [W]:     1718.0    max(Torque) [Nm]:      0.762    max(Axial thrust) [N]:      965.3
max(Centrifugal stress) [MPa]:        0.4   at       21752 rpm

max(Power) [W]:     2288.5    max(Torque) [Nm]:      0.923    max(Axial thrust) [N]:     1169.3
max(Centrifugal stress) [MPa]:        0.5   at       23927 rpm

Weight compressor assembly [kg]:     0.0037
Weight electric motor      [kg]:     0.6588
```